



UNIVERSITY  
OF SUSSEX

---

DOCTORAL THESIS

---

**Optimisation studies and data-driven  
background estimation for searches for  
the supersymmetric partner of the top  
quark with the ATLAS Detector at the  
LHC**

*A thesis submitted in fulfilment of the requirements  
for the degree of Doctor of Philosophy*

*in the*

Experimental Particle Physics Research Group  
School of Mathematical and Physical Sciences

*Author:*

Fabrizio MIANO

*Supervisor:*

Dr. Fabrizio SALVATORE

12th March 2018

*To Mum, Dad, and Eleonora*

# ACKNOWLEDGEMENTS

---

The writing of this section has been a rather emotional time as it's made me retrace my entire PhD journey.

Since I've started the programme, my supervisor, Fabrizio Salvatore, has constantly been an outstanding support across the whole spectrum of my needs, as a PhD student. Not only has he been able to spot in advance when I needed support, no matter whether work-related or simply the right joke at the right time that would cheer me up, but he's also been to me a warm human being equipped with a distinguished dose of both empathy and motivation capability. My second supervisor and head of the ATLAS-Sussex group, Antonella De Santo, has also been a constant presence to whom I feel grateful for the support provided and with whom I shared all my PhD-related moans. I feel grateful also to Iacopo Vivarelli and Alex Cerri whose doors have always been open, whenever I had questions or doubts. Thanks Alex for all the delicious dinners at yours, which you've sweetened my LTA at CERN with. Thanks also to you, Lily, for the great *#ScienceOnBuses* project you've organised and for the amazing times, even if just few, we've spent at the pub. In other words, my experience at Sussex has been just wonderful. The perfect chance for a professional and personal growth.

A few people properly mentored me throughout the whole programme. Kerim Suruliz, Mark Sutton, and Zara Grout, who's since moved on from the group, are unquestionably the people who've shared their knowledge with me the most (besides the outrageous number of lines of code). Without you guys, it would've been a nightmare. Nicky, Carlos, and Umberto, who've also since moved on from the group, and Benedict, have always been a friendly presence, at both Sussex and CERN, and also outside the work environment.

Yusufu Shehu, a.k.a. *Suf*, has played a major role across my whole PhD. He's taken me by the hand through the difficulties that one has to go through when approaching the ATLAS world, but he's especially been the one who's helped me the most with the traumatising transition that a Sicilian guy has to face when moving to a country like the UK (language, culture, etc.). Thanks Suf. Not only have you been a great colleague, but you've also become a great friend who I've shared sad times, emotional outbursts, and nights out in Brighton with, along the line of *Tales of ordinary madness*.

A big *Thank you!* goes also to Giuseppe Lerner who, with his remarkable generosity and physics knowledge, has helped me go through the sourness of the last 4 years, and who I've shared pints, laughter, and interesting discussions with. To people like Mark Stringer, James Waterfield, and Ed Leming, I would like to say: "*Thanks lads. My time here wouldn't have been the same without you*".

I'd also like to thank Nicola, Sam, Emma, Tom, electroweak Fab, Giovannis and the Marios, who've been a good company to share the office with, and Jack, Rob and Helena for having shared the pain of living in a crappy house. Special thanks to Fabione and Vangelis, who've not only been good physicists to share thoughts with, but trips and drinks, too.

When it comes to my LTA period at CERN, Benjamin Sowden and Callum Kilby are the ones who I'd like to mention. They've been great officemates who've provided me with a lot of incredibly useful insights about the life at CERN (and lines of code), and who I've shared my times in R1 with. Thanks also to STFC for the funding provided. And how could I not mention Massimo, Mario, and Daniele?! You've all been social-life saviours with joyful dinners at mine and nights out in Geneva. Thank you!

Among the ATLAS  $\tilde{\tau}0\ell$  group members I would like to thank Andrea Rodriguez and Walter Hopkins who've been a pleasure to work with. Your friendly attitude has helped me get the work done and ease the stress of endless boring *cutflow challenges*.

*Two (three) in distress make sorrow less.*

An expression of sincere gratitude goes to my MSc supervisor, Giuseppe Verde, who's made me want to go for a PhD, who's given me the boost of confidence I needed, and whose help has also been decisive to get where I am now.

To all of you my Sicilian mates, particularly to you Lucigno, inspiring, reliable, eternally funny friend, ready to listen and solve my problems, and to all those spread across the globe, to you Massimo and Renatano, always there no matter what, to you Scifo, Enza, Emilianotidie, Sebi, to you Gesu, Michi, Stefano, Curenti, Barbone, Amenta, to you Pietro and Pistocchi, friends of a lifetime, to all of you lovely pack of kooks, I save a special place in my heart. You've been managing to make up for the distance that separates us with either fantastic reunions, or long Play Station sessions during those stay-at-home weekends. You've always been a constant and pleasant presence even if thousands of miles away from me.

To my family, a continuous warmth dispenser, a safety net that has been giving me the strength not to give up even during the toughest times, a huge *thank you* for having been a financial support throughout my education and the backbone of my entire upbringing. The credits of what I've become go to you Dad, to you Mum, and to you Sister. This work's also for you, it's for us.

Finally, my last thought is for you Martina. Your patience, support, and affection, helped me deal with the last tough years more than anything else. I hope the best has yet to come.

# **STATEMENT**

I, Fabrizio MIANO, hereby declare that this thesis has not been and will not be, submitted in whole or in part to another university for the award of any other degree.

*Brighton,  
12th March 2018*

---

Fabrizio MIANO

University of Sussex  
School of Mathematical and Physical Sciences  
Experimental Particle Physics Research Group

DOCTORAL THESIS

---

Optimisation studies and data-driven background estimation for  
searches for the supersymmetric partner of the top quark with the  
ATLAS Detector at the LHC

---

by Fabrizio MIANO

## ABSTRACT

This thesis presents the search for the supersymmetric partner of the top quark in  $\sqrt{s} = 13$  TeV proton-proton collisions at the LHC using data collected by the ATLAS detector in 2015 and 2016. Results were interpreted considering natural supersymmetric extensions of the Standard Model in  $R$ -parity conserving decays. Events characterised by four or more jets and missing transverse momentum in the final states were selected. The performances of the tracking algorithms used by the ATLAS online trigger were studied. Optimisation studies of the search regions to increase the sensitivity to supersymmetric signals were performed and data-driven techniques to estimate Standard Model backgrounds were employed. The agreement between data and background predictions was extensively checked and the extrapolations from background-enriched regions to signal-enriched regions were validated. The analysis yielded no significant excess therefore exclusion limits on various models were set.

# CONTENTS

<b>Introduction</b>	<b>1</b>
<b>1 The Standard Model and Supersymmetry</b>	<b>2</b>
1.1 The Standard Model . . . . .	2
1.1.1 Electroweak Symmetry Breaking and the Higgs mechanism . . . . .	5
1.1.2 Limitations of the Standard Model . . . . .	8
1.2 Supersymmetry and the MSSM . . . . .	10
1.2.1 Minimal Supersymmetric Standard Model . . . . .	12
1.2.2 Phenomenology of Supersymmetry . . . . .	14
<b>2 The ATLAS Experiment at the LHC</b>	<b>19</b>
2.1 The LHC . . . . .	19
2.2 The ATLAS Detector . . . . .	21
2.2.1 The Magnet System . . . . .	23
2.2.2 The Inner Detector . . . . .	24
2.2.3 The Calorimeters . . . . .	27
2.2.4 The Muon Spectrometer . . . . .	28
2.3 The ATLAS Trigger System . . . . .	30
<b>3 The ATLAS Trigger System</b>	<b>31</b>
3.1 Overview . . . . .	31
3.2 Level-1 Trigger . . . . .	33
3.3 High-Level Trigger . . . . .	35
3.3.1 Inner detector tracking . . . . .	35
3.3.2 Performance of HLT . . . . .	36
<b>4 Event Simulation and Object Reconstruction</b>	<b>42</b>
4.1 Generation of an MC-simulated event . . . . .	43
4.2 Object Reconstruction . . . . .	46
<b>5 Search for top squarks in all-hadronic final states</b>	<b>56</b>

5.1	SUSY Signals . . . . .	57
5.1.1	Benchmark processes . . . . .	57
5.1.2	MC samples . . . . .	58
5.2	Objects definition . . . . .	58
5.3	Event Selection . . . . .	60
5.3.1	Triggers used . . . . .	60
5.3.2	Event cleaning . . . . .	61
5.4	Standard Model Backgrounds . . . . .	61
5.5	Signal Region optimisation . . . . .	63
5.5.1	Preliminary selection and discriminating key variables . . . . .	63
5.5.2	Optimisation strategy . . . . .	65
5.6	Nominal Background Estimation . . . . .	65
5.6.1	Control Regions . . . . .	65
5.6.2	Validation Regions . . . . .	65
5.7	Data-Driven Background Estimation . . . . .	65
5.8	Results and Interpretation . . . . .	65
<b>Conclusion</b>		<b>66</b>
<b>A <math>t\bar{t}+Z</math> estimation in DM plus heavy flavour</b>		<b>67</b>
<b>List of Acronyms</b>		<b>68</b>
<b>Bibliography</b>		<b>72</b>

# INTRODUCTION

*The journey, not the destination  
matters.*

---

Thomas S. Eliot

Last thing to write

# THE STANDARD MODEL AND SUPERSYMMETRY

1

*A theory is something nobody believes, except the person who made it. An experiment is something everybody believes, except the person who made it.*

Albert Einstein

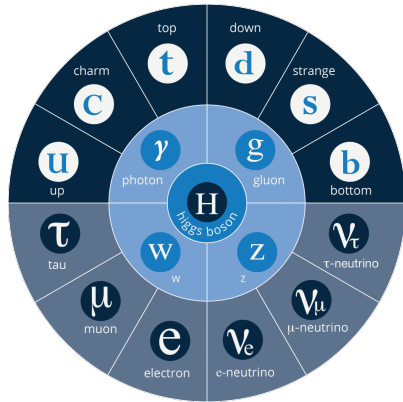


Figure 1.1: The elementary particles of the [SM](#). From the outermost to the innermost; fermions (quarks, top-half wheel, leptons, bottom-half wheel), vector bosons, and the Higgs boson.

Section 1.1 presents an overview of the [SM](#) of particle physics, together with its limitations (Section 1.1.2) and the need of an extension. One of the most popular of these extensions, Supersymmetry ([SUSY](#)), will be discussed in Section 1.2 where an overview of the theory and the motivations behind its success will be presented. The description of the Minimal Supersymmetric Standard Model ([MSSM](#)) in Section 1.2.1, and finally the phenomenology of supersymmetry, with particular attention to third-generation supersymmetry - as the most relevant theoretical support to this work - will be discussed in Section 1.2.2.

## 1.1 The Standard Model

The [SM](#) is an effective theory that aims to provide a general description of fundamental particles and their interactions.

The 20<sup>th</sup> century can be considered a quantum revolution. Several experiments led to discoveries which were found to be, together with the formalised theory, a solid base of the [SM](#) of

particle physics and our description of nature. Several particles were first predicted and then experimentally observed e.g. the  $W$  and the  $Z$  bosons, the  $\tau$  lepton, [1], and more recently the Higgs boson at the Large Hadron Collider (LHC) discovered by the ATLAS [2] and CMS [3] collaborations.

The SM is a Quantum Field Theory (QFT) where particles are treated like excitations of quantum fields in a four-dimensional Minkowski space-time [4]. It can describe three of the four fundamental forces; weak, electromagnetic, and strong, but not gravity.

The most general classification of the elementary particles within the SM can be made by means of spin and their behaviour under Poincaré transformations [5]: *fermions* (leptons and quarks), usually referred to as matter particles, which have half-integer spin values, in unit of  $\hbar$ , and *bosons*, usually referred to as information carriers, which have integer-spin values. A noteworthy subset of bosons is formed by the Spin-1 bosons, also known as gauge bosons. These can be considered mediators of the forces. Figure 1.1 displays the elementary particles of the Standard Model known as of today.

## Symmetries and Gauge Groups

In 1915, the German mathematician and theoretical physicist Emmy Noether (23 March 1882 – 14 April 1935) proved that every differentiable symmetry of the action - defined as the integral over space of a Lagrangian density function  $S = \int \mathcal{L} dt$  - of a physical system has a corresponding conservation law [6]. More generally, a symmetry is a property of a physical system and under certain transformations this property is preserved.

A gauge theory in QFT, is a theory in which the Lagrangian is invariant under a continuous group of local transformations. Group theory was adopted to describe the symmetries conserved in the SM. The gauge group of the SM is the *Lie Group* which contains all the transformations between possible gauges [5]. The Lie algebra of group generators is associated to any Lie group and for each group generator there emerges a corresponding field, called the gauge field, and the quanta of such fields are called *gauge bosons*.

The three SM interactions can therefore be mathematically described by the following:

$$U(1)_Y \otimes SU(2)_L \otimes SU(3)_C \quad (1.1)$$

Here,  $Y$  is the weak hypercharge, used to estimate the correlation between the electric charge ( $Q$ ) and the third component of the weak isospin ( $I_3$ ) via the relation  $Q = I_3 + Y/2$ , where  $I_3$  can either be  $\pm 1/2$  or 0 for left-handed and right-handed particles, respectively;  $L$  the left-handedness; and  $C$  the colour charge.

Quantum Electrodynamics (QED) is an Abelian gauge theory described by the symmetry group  $U(1)$ . The electromagnetic four-potential is its gauge field and the photon its gauge boson [7]. The interactions between charged fermions occurs by the exchange of a massless photon.

The weak interaction is described by the non-Abelian gauge group  $SU(2)$ . The  $SU(2)$  generators are the massless gauge bosons  $W_\mu^{\alpha=1,\dots,3}$  and they violate parity by acting only on left-handed particles. As a consequence of non-Abelianity,  $SU(2)$  gauge bosons can self-interact as the generator commutators are non-vanishing. Additionally, quarks can also interact through weak interaction as mixtures of [SM](#) eigenstates as described by the CKM matrix [8].

Finally, the strong interaction, described by the symmetry group  $SU(3)$ , has eight massless gauge bosons, the gluons,  $G_\mu^{\alpha=1,\dots,8}$  which can be exchanged between quarks and can also self-interact.

## Fermions

There are twelve fermions in the [SM](#): six quarks and six leptons. In particular, fermions can be grouped into three generations. Each generation contains four particles; one up- and one down-type quark, one charged lepton and one neutral lepton. The masses of the charged leptons and quarks increase with the generation. The six quarks of the [SM](#) can be grouped into three  $SU(2)$  doublets;

$$\begin{pmatrix} u \\ d \end{pmatrix}, \quad \begin{pmatrix} c \\ s \end{pmatrix}, \quad \begin{pmatrix} t \\ b \end{pmatrix}$$

The up-type quarks (*up, charm, top*) have charge  $+\frac{2}{3}e$  and the down-type quarks (*down, strange, beauty/bottom*) have charge  $-\frac{1}{3}e$ , where  $e$  is the electron charge. Quarks also have another quantum number that can be seen as the analogue of the electric charge; the colour charge. This can exist in three different states; *red, green* and *blue*, but they cannot exist as free particles. They rather group to form hadronic matter, also known as *hadrons*. There are two kinds of hadrons; mesons and baryons. Mesons are quark-antiquark systems, e. g. the pion, and baryons are three-quark system, e. g. protons and neutrons. Quarks and anti-quarks have a baryon number of  $\frac{1}{3}$  and  $-\frac{1}{3}$ , respectively.

There are six leptons and they can be classified in charged leptons (electron  $e$ , muon  $\mu$ , tau  $\tau$ ) and neutral leptons (electron neutrino  $\nu_e$ , muon neutrino  $\nu_\mu$ , tau neutrino  $\nu_\tau$ ):

$$\begin{pmatrix} \nu_e \\ e^- \end{pmatrix}, \quad \begin{pmatrix} \nu_\mu \\ \mu^- \end{pmatrix}, \quad \begin{pmatrix} \nu_\tau \\ \tau^- \end{pmatrix}$$

Each lepton has a characteristic quantum number, called lepton number ( $L$ ). Negatively (positively) charged leptons have  $L = -1$  ( $L = 1$ ) and neutral leptons have  $L = 1$ . The lepton number is conserved in all the interactions.

## Forces of Nature

Forces in the [SM](#) are described by gauge theories, where the interactions are mediated by a vector gauge boson.

[QED](#) describes the electromagnetic force, which only affects charged leptons (neutrinos are instead affected by the weak force, mediated by the  $W^\pm$  and  $Z^0$  bosons) and quarks and it is mediated by the photon ( $\gamma$ ).

The weak interaction is associated with *handedness* i. e., the projection of a particle spin onto its direction of motion. Both leptons and quarks have left- and right-handed components. However, only the left-handed (right-handed) component for neutrinos (anti-neutrinos) has been observed. This means that nature prefers to produce left-handed neutrinos and right-handed anti-neutrinos, which is the so-called *parity violation* [9].

The strong interaction, mediated by the gluon, electrically neutral and massless, is described by Quantum Chromodynamics ([QCD](#)). Its coupling ( $\alpha_s$ ) increases with increasing distance and is smaller at short range. In particular,  $\alpha_s$  evolves as a function of the transferred four-momentum squared,  $Q^2$ , as follows:

$$\alpha_s(Q^2) \propto \frac{1}{n_f \log\left(\frac{Q^2}{\Lambda_{\text{QCD}}^2}\right)} \quad (1.2)$$

where  $n_f$  is the number of quarks with mass below  $Q^2$  and  $\Lambda_{\text{QCD}}$  is the [QCD](#) characteristic scale. Eq. 1.2 shows that  $\alpha_s$  decreases as a function of  $\Lambda_{\text{QCD}}$ , but at the same time it quickly diverges when  $Q^2$  gets closer to  $\Lambda$ . In other words, as the condition  $\alpha_s \ll 1$  only holds for  $Q^2 \gg \Lambda_{\text{QCD}}$ , [QCD](#) can be treated perturbatively<sup>1</sup> only at high energy scales<sup>2</sup>. Furthermore, [QCD](#) has three important features:

- *confinement*: quarks or gluons cannot be observed as free particles, but only colourless “singlet” states can be observed as “jets”, namely collimated cone-shaped sprays of hadrons;
- *asymptotic freedom*: interactions between quarks and gluons become weaker as the energy scale increases and the corresponding length scale decreases, as  $\alpha_s \rightarrow 0$  for  $Q^2 \rightarrow \infty$
- *hadronisation*: when quarks or gluons are pulled apart, the production of pairs of hadrons, produced from the vacuum, is energetically preferred to an increase in distance.

Table 1.1 summarises the forces described in the [SM](#) and the main characteristics of the mediators. The gravitational force is believed to be mediated by the graviton, but as already mentioned, since it is not included in the [SM](#), it will not be further discussed.

### 1.1.1 Electroweak Symmetry Breaking and the Higgs mechanism

In 1979 Sheldon Glashow, Abdus Salam, and Steven Weinberg were awarded the Nobel Prize in Physics for their contributions to the so-called electroweak unification [10, 11, 12]. In the

<sup>1</sup> Perturbation theory (quantum mechanics) is an approximation to describe a complicated quantum system in terms of a simpler one.

<sup>2</sup> Perturbation theory can only be used when the coupling constant (expansion parameter) is small.

Table 1.1: Forces and mediators described by the SM

Force	Name	Symbol	Mass [GeV]	Charge
Electromagnetic	Photon	$\gamma$	0	0
Weak	W	$W^\pm$	80.398	$\pm e$
	Z	$Z^0$	91.188	0
Strong	Gluon	$g$	0	0

mathematical description of the SM in 1.1, the electroweak interaction is described by  $U(1)_Y \otimes SU(2)_L$ .

The four electroweak physical bosons  $W^\pm$ ,  $Z$  and  $\gamma$  are related to the four unphysical gauge bosons  $W_\mu^{\alpha=1,\dots,3}$  and  $B_\mu$ . In particular, to obtain the physical bosons the gauge bosons have to mix as follows;

$$A_\mu = W_\mu^3 \sin \theta_W + B_\mu \cos \theta_W \quad (1.3)$$

$$Z_\mu = W_\mu^3 \cos \theta_W - B_\mu \sin \theta_W \quad (1.4)$$

$$W_\mu^\pm = \frac{1}{\sqrt{2}} \left( W_\mu^1 \mp i W_\mu^2 \right) \quad (1.5)$$

Here,  $\theta_W$  is the so-called *Weinberg angle* which is the angle by which spontaneous symmetry breaking rotates the original gauge bosons  $W_\mu^3$  and  $B_\mu$  into the physical  $Z$  and  $\gamma$ .  $A_\mu$  and  $Z_\mu$  are the photon and the  $Z$  boson fields, respectively. The  $\theta_W$  angle can be experimentally determined in terms of the coupling strengths, of the  $B_\mu(g_1)$  and the  $W_\mu^\alpha(g_2)$  to the fermions, using the relation  $\tan \theta_W = g_1/g_2$ .

The mass terms for both gauge bosons and fermionic fields are forbidden by the electroweak gauge as they are not invariant under gauge transformations. Nonetheless, it was experimentally proven that  $W$  and  $Z$  bosons are massive [7], therefore in order for the SM assumption to hold, the electroweak symmetry must be broken.

The SM Lagrangian can be written as the sum of the various Lagrangians describing the three interactions and the masses of the elementary particles as follows:

$$\mathcal{L}_{\text{SM}} = \mathcal{L}_{\text{EWK}} + \mathcal{L}_{\text{QCD}} + \mathcal{L}_{\text{Mass}} \quad (1.6)$$

In order for the SM Lagrangian to remain a re-normalisable theory, the mass terms ( $\mathcal{L}_{\text{Mass}}$ ) cannot be inserted by hand. A mechanism, that can preserve the gauge symmetry in the SM and can solve the inconsistency arisen from the mass difference between the gauge bosons and the physical ones is needed. A British theoretical physicist, Peter Higgs (29 May 1929, Newcastle upon Tyne, UK), came up with a brilliant solution for which he was awarded the Nobel Prize in Physics in 2013. Higgs proposed [13] that broken symmetry in the electroweak theory could

explain the origin of masses of elementary particles, and in particular of  $W$  and  $Z$  bosons. The mechanism introduces a scalar field, known as the Higgs field, thought to couple to both massive fermions and bosons. The  $SU(2)$  doublet is then introduced in the [SM](#):

$$\phi = \begin{pmatrix} \phi^+ \\ \phi^0 \end{pmatrix} \quad (1.7)$$

with  $\phi^+$  and  $\phi^0$  generic complex fields:

$$\phi^+ = \frac{\phi_1 + i\phi_2}{\sqrt{2}}, \quad \phi^0 = \frac{\phi_3 + i\phi_4}{\sqrt{2}} \quad (1.8)$$

Consider a Lagrangian of the form:

$$\mathcal{L}_{\text{Higgs}} = (\partial_\mu \phi)^* (\partial^\mu \phi) - V(\phi) \quad (1.9)$$

where  $V(\phi)$  is now the Higgs potential. Re-normalisability and  $SU(2)_L \otimes U(1)_Y$  invariance require the Higgs potential to be of the following form:

$$V(\phi) = \mu^2 \phi^\dagger \phi + \lambda (\phi^\dagger \phi)^2 \quad (1.10)$$

The Lagrangian in Eq. 1.9 is the Higgs Lagrangian if  $\phi$  is chosen to be the following:

$$\phi = \begin{pmatrix} \phi^+ \\ \phi^0 \end{pmatrix} = \begin{pmatrix} G^+ \\ \frac{1}{\sqrt{2}} (v + H + iG^0) \end{pmatrix}$$

Here, the complex scalar field  $G^\pm$  and the real scalar field  $G^0$  correspond to Goldstone bosons, and the real scalar field  $H$  is the [SM](#) Higgs boson field [14]. These massless scalars are absorbed due to the gauge transformations by the electroweak gauge bosons of the [SM](#):

$$\phi = \begin{pmatrix} \phi^+ \\ \phi^0 \end{pmatrix} = \begin{pmatrix} 0 \\ \frac{1}{\sqrt{2}} (v + H) \end{pmatrix} \quad (1.11)$$

The Higgs potential in Eq. 1.10 is displayed in Figure 1.2 if  $\lambda$  and  $\mu$  are chosen to be real. Such potential has a non-zero ground state,  $v$ , also known as Vacuum Expectation Value ([VEV](#)):

$$\phi_0 = \begin{pmatrix} 0 \\ \frac{1}{\sqrt{2}} v \end{pmatrix} \quad (1.12)$$

Such representation remains invariant under  $U(1)$  allowing electric charge conservation. However, the [SM](#) gauge symmetry 1.1 is broken into  $SU(2)_L \otimes U(1)_Y$ .

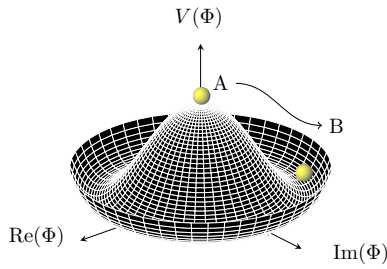


Figure 1.2: The Higgs potential in the complex plane.

In summary, to generate particle masses gauge symmetry must be broken. However, in order for the theory to remain renormalisable, the global Lagrangian symmetry must be preserved. This can be solved introducing the concept of *spontaneous symmetry breaking* (SSB): a mechanism that allows a symmetric Lagrangian, but not a symmetric vacuum. In particular, given a Lagrangian invariant under a certain transformation,  $T_X$ , and a generic set of states, that transform under  $T_X$  as the elements of a multiplet, the symmetry is spontaneously broken if one of those states is arbitrarily chosen as the ground state of the system. The interaction of the Higgs field with the  $SU(2) \otimes U(1)$  gauge fields,  $W_\mu^{\alpha=1,2,3}$ , result in the three gauge bosons fields acquiring mass whilst the  $A_\mu$  field remains massless.

### 1.1.2 Limitations of the Standard Model

The SM has been extensively validated at the Large Electron-Positron Collider (LEP) (European Organization for Nuclear Research (CERN)), Tevatron at Fermilab, and SLAC. Run 1 of the LHC extended the validation beyond the energy limits of previous colliders as shown in Figure 1.3: the agreement, between the measured production cross-section of various SM processes and the SM predictions, looks very good. However, there are some fundamental questions that still have no answer.

#### Hierarchy Problem

Due to the coupling of the Higgs field to the fermionic fields, the one-loop corrections to the Higgs mass receive several contributions [16]. In particular, looking at Figure 1.4:

$$\Delta m_H^2 = -\frac{|\lambda_f|^2}{8\pi^2} \Lambda_{\text{UV}}^2 + \dots \quad (1.13)$$

where,  $\lambda_f$  is the coupling constant to the fermionic field;  $\Delta m_H^2$  is the difference between the observed Higgs mass  $m_H^2$  and the bare mass,  $m_H^0$  (Lagrangian parameter);  $\Lambda_{\text{UV}}$  is the ultraviolet momentum cut-off, selected to be at the Planck scale ( $\sim 2 \cdot 10^{18}$  GeV), at which a QFT description of gravity is believed to become possible. The correction to the Higgs mass will be around 30 orders of magnitude larger than Higgs mass itself, in opposition to what has been measured. This difference just mentioned, between the electroweak scale and the Planck scale arisen from the quantum corrections to the Higgs mass, is the so-called Hierarchy Problem [16].

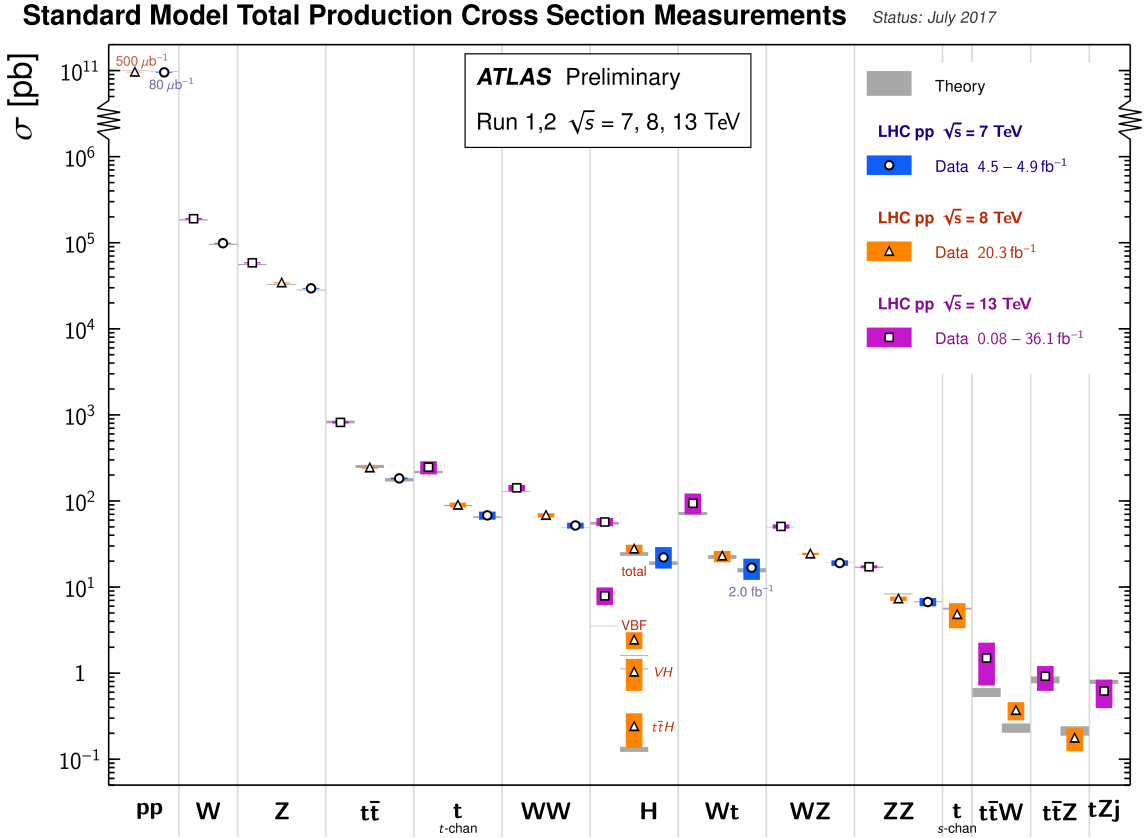


Figure 1.3: Summary of several SM total production cross-section measurements, corrected for leptonic branching fractions, compared to the corresponding theoretical expectations. All theoretical expectations were calculated at NLO or higher. The luminosity used for each measurement is indicated close to the data point. Uncertainties for the theoretical predictions are quoted from the original ATLAS papers. They were not always evaluated using the same prescriptions for PDFs and scales. Not all measurements are statistically significant yet [15].

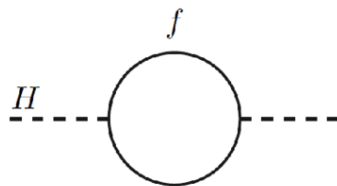


Figure 1.4: One-loop quantum corrections to the Higgs mass. A fermion correction with coupling  $\lambda_f$ .

## Neutrino Masses

The Super-Kamiokande Collaboration in 1998 [17], and SNO Collaboration in 2001 [18], have provided measurements of the neutrino flux from solar and atmospheric sources. The Nobel Prize in Physics 2015 was awarded jointly to Takaaki Kajita and Arthur B. McDonald “for the discovery of neutrino oscillations, which shows that neutrinos have mass” [19]. Such feature contradicts the description of the neutrinos in the SM, which are assumed to be massless, therefore there needs to be a mechanism that generates neutrino masses. One possibility would be to add Majorana mass terms or adding additional right-handed neutrinos with a very heavy mass, known as the see-saw mechanism [20].

## Dark Matter

Although Dark Matter (DM) has never been directly observed, its existence is inferred from its gravitational effects. For example, looking at galaxies rotation, it was observed that the rotation speed was higher than expected, given the amount of visible matter [21]. Two different reasoning arose during the last century to justify such effect: there is either matter that cannot be seen by us (in terms of visible light), which contributes to the galactic mass, or the general relativity works differently at galactic distances. The former is believed to be the most likely and it implies the existence of new particles which do not interact via electromagnetic interaction, the so-called Weakly Interacting Massive Particle (WIMP) [22].

## 1.2 Supersymmetry and the MSSM

One of the main motivations for SUSY is the cancellation of quadratic divergences to  $\Delta m_H^2$  via the introduction of the so-called SUSY particles with a half-integer spin difference with respect to their SM partners. This provides a solution to the hierarchy problem as the Higgs mass squared potential receives corrections from a new scalar of mass of the form:

$$\Delta m_H^2 = -\frac{|\lambda_S|^2}{16\pi^2} \left[ \Lambda_{UV}^2 - 2m_S^2 \ln(\Lambda_{UV}/m_S) + \dots \right] \quad (1.14)$$

where,  $\lambda_S$  is the coupling of SUSY particles to the Higgs field. This term cancels the fermionic contributions in Eq. 1.13 since the couplings are the same, which means that the experimentally measured mass of the Higgs boson can be obtained without performing any unnatural *tuning* of the parameters [23, 24]. This is what makes SUSY a *natural* theory<sup>3</sup>.

The running of gauge coupling constants<sup>4</sup> is predicted by the SM, but, as previously mentioned, although the electroweak unification occurs at  $\sim 100$  GeV, it is not the case for the strong force. In the MSSM, a supersymmetric extension of the SM, due to addition of *new* particles involved in the gauge interactions, a new set of coefficients arise. As shown in Figure 1.5 the three lines, representing electromagnetic (dashed blue), weak (dashed red) and strong (solid green) interactions respectively, do not meet at one point, but they do with the introduction of supersymmetry. This can therefore be considered an approximate unification, of all three gauge couplings, at the Planck scale, which is an indication for a potential Grand Unification Theory (GUT) that could be obtained within a supersymmetric model. In addition, together with the unification at the GUT scale, another good motivation for SUSY searches is that, if SUSY is MSSM-like ( $m_{SUSY}$  not heavier than  $\sim 1$  TeV), it can be discovered at the LHC.

SUSY introduces a space-time symmetry that relates bosons to fermions and vice-versa, via

---

<sup>3</sup> The Naturalness of a theory is a property for which dimensionless ratios between free parameters should assume sensible values and that free parameters are not fine-tuned.

<sup>4</sup> The coupling strength, as a function of energy, is calculable given a value at a fixed scale.

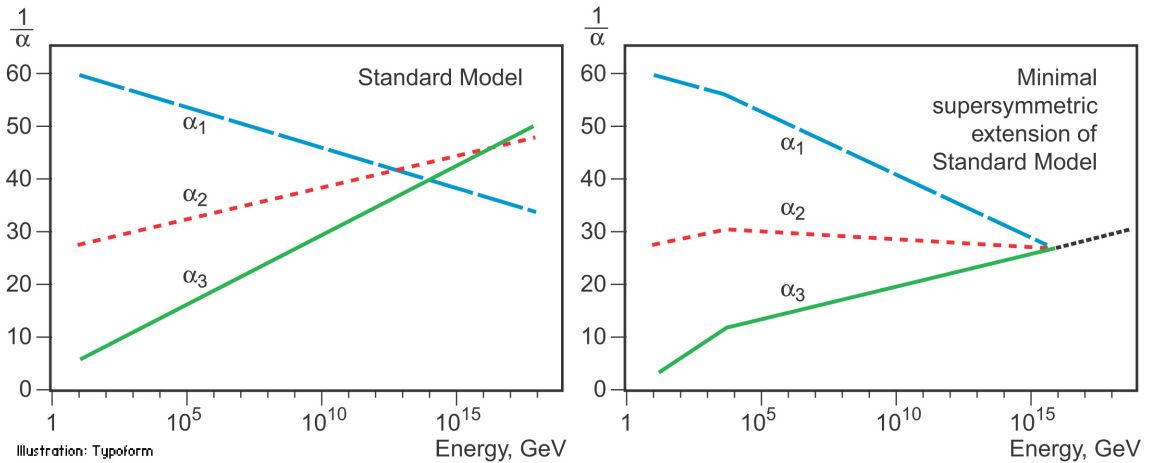


Figure 1.5: The inverse couplings of electromagnetic (dashed blue), weak (dashed red) and strong (solid green) interactions with the SM (left) and a supersymmetric model (right). In the SM the three lines do not meet at one point, but with the introduction of supersymmetry, and assuming that the supersymmetric particles are not heavier than about 1 TeV, they do meet.

a transformation of the form of:

$$Q |\text{fermion}\rangle = |\text{boson}\rangle, \quad Q |\text{boson}\rangle = |\text{fermion}\rangle \quad (1.15)$$

For each SM particle there exists a supersymmetric partner, generally called *sparticle* (where the s stands for “scalar”), with a spin difference of  $\Delta s = 1/2$ . Each pair of partners is arranged in a so-called *supermultiplet*. The two components have same masses and quantum numbers, but different spin, due to their relation to the Q operator (and its properties).

*Sleptons* and *squarks* interact as their SM equivalent. The superpartners of the left-handed fermion components couple weakly, while the superpartners of the right-handed SM fermion components do not. Gauge supermultiplets contain a vector boson and two spin- $\frac{1}{2}$  fermions. Spin-1 bosons are arranged in gauge multiplets, and their superpartners, referred to as *gauginos*, are spin- $\frac{1}{2}$  fermions. Unlike the SM, the Spin-0 Higgs boson has two supermultiplets containing sparticles with different weak isospin values, referred to as  $H_u$  and  $H_d$ , which are required to give mass to both the up- and down-type sparticles. Higgs SUSY partners are called the *Higgsinos*.

As of today, SUSY particles have not been observed, resulting in the assumption that SUSY must be a broken symmetry, otherwise superpartners would have the same masses as their SM equivalent. However, if sparticles were to be too heavy (close to the Planck scale), the hierarchy problem would be re-introduced and therefore would still remain unsolved. The *soft SUSY* breaking mechanism, described in Section 1.2.1, overcomes this problem by imposing constraints on the masses of sparticles to a range that can be experimentally explored.

### 1.2.1 Minimal Supersymmetric Standard Model

There does not exist a unique extension of a supersymmetric **SM**, i. e. **SUSY** is not a well-defined model but it is more a framework within which various **SM** extensions can be derived. The **MSSM**, a minimal supersymmetric extension of the **SM** [25], is defined by essentially doubling up the number of particles in the **SM** theory in order to include all the **SM** particles as well as their corresponding superpartners.

#### Soft SUSY breaking

The mass spectrum of the **SUSY** particles must sit somewhere at a larger scale than the **SM** one, as supersymmetric particles have not been discovered at the mass scale of their **SM** partners. This gives us a hint that supersymmetry cannot be an exact symmetry and therefore it is broken. There has to be an analogy with the electroweak symmetry breaking discussed in 1.1.1, where the symmetry is broken by a non-zero **VEV**. The mechanism must be spontaneous in order for the broken supersymmetry to still provide a solution to the hierarchy problem: a big alteration of the relationship between the fermionic and scalar couplings will result in a non-cancellation of the corrections to the Higgs mass squared parameter. This equates to adding terms to the **SUSY** Lagrangian which are gauge invariant and violate **SUSY**, but contain only masses and couplings with positive mass dimension. The total Lagrangian is defined as;

$$\mathcal{L}_{\text{MSSM}} = \mathcal{L}_{\text{SUSY}} + \mathcal{L}_{\text{soft}} \quad (1.16)$$

where all the additional terms are contained within  $\mathcal{L}_{\text{soft}}$  and the original **SUSY** invariant interaction terms are contained within  $\mathcal{L}_{\text{SUSY}}$ . A new set of parameters is then introduced into this **SM** extension. These parameters determine the mixing between the flavour eigenstates and the **SUSY** phenomenology, which will be discussed in Section 1.2.2.

#### MSSM mass spectrum

As per the **SM** gauge bosons, the gaugino masses are affected by electroweak symmetry breaking. The new states, introduced in the  $\mathcal{L}_{\text{soft}}$ , mix to form the mass eigenstates of the sparticles. The neutral Winos ( $\tilde{W}^0$ ), Binos ( $\tilde{B}^0$ ), and Higgsinos ( $\tilde{H}^0$ ) mix to form the four *neutralinos*  $\tilde{\chi}_i^0$  ( $i = 1, 2, 3, 4$ ) as it follows;

$$\begin{pmatrix} \tilde{\chi}_1^0 \\ \tilde{\chi}_2^0 \\ \tilde{\chi}_3^0 \\ \tilde{\chi}_4^0 \end{pmatrix} = \begin{pmatrix} M_1 & 0 & -c_\beta s_W m_Z & c_W s_\beta m_Z \\ 0 & M_2 & c_\beta c_W m_Z & -c_W s_\beta m_Z \\ -c_\beta s_W m_Z & c_\beta s_W m_Z & 0 & -\mu \\ s_\beta c_W m_Z & -s_\beta c_W m_Z & -\mu & 0 \end{pmatrix} \begin{pmatrix} \tilde{B}^0 \\ \tilde{W}^0 \\ \tilde{H}_u^0 \\ \tilde{H}_d^0 \end{pmatrix} \quad (1.17)$$

Here,  $c_\beta = \cos \beta$ ,  $(s_\beta) = \sin \beta$ ,  $c_W = \cos \theta_W$  and  $(s_W) = \sin \theta_W$ .  $M_1$ ,  $M_2$  are related to gaugino masses and  $\mu$  to Higgsinos mass,  $\tan \beta$  is the ratio of the **VEVs** of the two Higgs doublet fields,

$\theta_W$  is the ratio of the electroweak coupling constants and,  $m_Z$  ( $m_W$ ) is the mass of the  $Z$  ( $W$ ) boson. The neutralino indices are conventionally assumed to increase with their masses. The charged winos ( $\tilde{W}^\pm$ ) and Higgsinos ( $\tilde{H}^\pm$ ) mix to form four *charginos*,  $\tilde{\chi}_i^\pm$  ( $i = 1, 2$ ) as it follows;

$$\begin{pmatrix} \tilde{\chi}_1^\pm \\ \tilde{\chi}_2^\pm \end{pmatrix} = \begin{pmatrix} M_2 & \sqrt{2}m_W s_\beta \\ \sqrt{2}m_W c_\beta & \mu \end{pmatrix} \begin{pmatrix} \tilde{W}^\pm \\ \tilde{H}^\pm \end{pmatrix} \quad (1.18)$$

Charginos and neutralinos mix as described in Eq. 1.18 and 1.17 and will be referred to as bino-like, wino-like or higgsino-like depending on their phenomenology. Gluinos do not mix as they carry colour charge.

The Higgs sector is also affected. There are five mass eigenstates,  $h^0$ ,  $H^0$ ,  $A^0$ , and  $H^\pm$ . These, together with the other MSSM particles are listed in Table 1.2.

Table 1.2: SUSY particles in the MSSM

Name	Spin	Gauge Eigenstates	Mass Eigenstates
Squarks ( $\tilde{q}$ )	0	$\tilde{u}_L \tilde{u}_R \tilde{d}_L \tilde{d}_R$	(same)
		$\tilde{c}_L \tilde{c}_R \tilde{s}_L \tilde{s}_R$	(same)
		$\tilde{t}_L \tilde{t}_R \tilde{b}_L \tilde{b}_R$	$\tilde{t}_1 \tilde{t}_2 \tilde{b}_1 \tilde{b}_2$
Sleptons ( $\tilde{l}$ )	0	$\tilde{e}_L \tilde{e}_R \tilde{\nu}_L$	(same)
		$\tilde{\mu}_L \tilde{\mu}_R \tilde{\nu}_L$	(same)
		$\tilde{\tau}_L \tilde{\tau}_R \tilde{\nu}_\tau$	$\tilde{\tau}_1 \tilde{\tau}_2 \tilde{\nu}_\tau$
Higgs bosons	0	$H_u^0 H_d^0 H_u^+ H_d^-$	$h^0 H^0 A^0 H^\pm$
Neutralinos ( $\tilde{\chi}_j^0$ )	1/2	$\tilde{B}^0 \tilde{W}^0 \tilde{H}_u^0 \tilde{H}_d^0$	$\tilde{\chi}_1^0 \tilde{\chi}_2^0 \tilde{\chi}_3^0 \tilde{\chi}_4^0$
Charginos ( $\tilde{\chi}_i^\pm$ )	1/2	$\tilde{W}^\pm \tilde{H}_u^\pm \tilde{H}_d^\pm$	$\tilde{\chi}_1^\pm \tilde{\chi}_2^\pm$
Gluino	1/2	$\tilde{g}$	(same)
Gravitino	3/2	$\tilde{G}$	(same)

In the MSSM the squark sector is specified by the mass matrix in the basis  $(\tilde{q}_L, \tilde{q}_R)$  with  $\tilde{q} = \tilde{t}$  or  $\tilde{b}$  [26]. A rotation matrix can be defined also for left- and right-handed squarks and sleptons, although in the MSSM the mixing is assumed to be non-zero only for the third-generation scalar partners. Stop ( $\tilde{t}_L, \tilde{t}_R$ ), sbottom ( $\tilde{b}_L, \tilde{b}_R$ ), and stau ( $\tilde{\tau}_L, \tilde{\tau}_R$ ) rotate into mass eigenstates,  $\tilde{t}_1, \tilde{t}_2, \tilde{b}_1, \tilde{b}_2, \tilde{\tau}_1, \tilde{\tau}_2$ , respectively, as described in Eq. 1.19 [27].

$$\mathcal{M}_{\tilde{q}}^2 = \begin{pmatrix} m_{\tilde{q}_L}^2 & a_q m_q \\ a_q m_q & m_{\tilde{q}_R}^2 \end{pmatrix} \quad (1.19)$$

with

$$\begin{aligned}
m_{\tilde{q}_L}^2 &= M_{\tilde{Q}}^2 + m_Z^2 \cos 2\beta \left( I_3^{q_L} - e_q \sin^2 \theta_W \right) + m_q^2, \\
m_{\tilde{q}_R}^2 &= M_{\{\tilde{U}, \tilde{D}\}}^2 + m_Z^2 \cos 2\beta e_q \sin^2 \theta_W + m_q^2, \\
a_q m_q &= \begin{cases} (A_t - \mu \cot \beta) m_t, & (\tilde{q} = \tilde{t}) \\ (A_b - \mu \tan \beta) m_t, & (\tilde{q} = \tilde{b}) \end{cases}
\end{aligned} \tag{1.20}$$

Here,  $I_3^{q_L}$  is the third component of the weak isospin and  $e_q$  the electric charge of the quark  $q$ .  $M_{\{\tilde{Q}, \tilde{U}, \tilde{D}\}}$  and  $A_{t,b}$  are soft SUSY-breaking parameters,  $\mu$  is the higgsino mass parameter, and  $\tan \beta$ , as previously mentioned, is the ratio of Higgs field VEVs. By diagonalising the matrix in Eq. 1.19 one gets the mass eigenstates

$$\tilde{q}_1 = \tilde{q}_L \cos \theta_{\tilde{q}} + \tilde{q}_R \sin \theta_{\tilde{q}} \tag{1.21}$$

$$\tilde{q}_2 = -\tilde{q}_L \sin \theta_{\tilde{q}} + \tilde{q}_R \cos \theta_{\tilde{q}} \tag{1.22}$$

with the mass eigenvalues  $m_{\tilde{q}_1}$ ,  $m_{\tilde{q}_2}$  ( $m_{\tilde{q}_1} < m_{\tilde{q}_2}$ ) and the mixing angle  $\theta_{\tilde{q}}$  ( $-\pi/2 < \theta_{\tilde{q}} \leq \pi/2$ ).

## 1.2.2 Phenomenology of Supersymmetry

As previously mentioned, the introduction of SUSY particles overcomes the problem of an unnatural fine-tuning to the Higgs mass due to its quadratic corrections.

### R-parity

The most general MSSM can contain operators that violate baryon and/or lepton number, thus allowing proton decays. The non-observation of proton decays forbids the existence of such terms. A possibility to avoid these operators is to introduce a new discrete symmetry named *R*-parity. The conserved quantum number is defined as;

$$P_R = (-1)^{3(B-L)+2s} \tag{1.23}$$

where  $B$ ,  $L$ , and  $s$  are the baryon, lepton, and spin number, respectively.

The SM particles have  $R = 1$  and SUSY partners have  $R = -1$ . When *R*-parity conservation is imposed on MSSM models, the mixing between particles and sparticles cannot occur, resulting in the number of SUSY particles to be even at every interaction vertex. Furthermore, all sparticles must be pair-produced and the Lightest Supersymmetric Particle (LSP) has to be stable and can be a good Dark Matter candidate.

Although SUSY searches in an *R*-parity violating (RPV) scenario have been extensively investigated by the particle-physics community, in this work only *R*-parity conserving (RPC) models, where the  $\tilde{\chi}_1^0$  is assumed to be the LSP, were considered.

### Phenomenological MSSM (pMSSM)

As mentioned in 1.2.1, once the SUSY soft breaking occurred, the unconstrained MSSM has more than 100 parameters in addition to the SM ones. This makes the SUSY searches, e. g. finding regions, in parameter space, that are consistent with the data, rather impractical. However, the number of free parameters can be reduced down to 19 if the following assumptions are made;

- no new source of CP-violation (CKM matrix is the only source)
- no Flavour Changing Neutral Currents (FCNC)
- masses of the first- and second-generation sfermions are identical (first- and second-generation universality)

The introduction of such parameters, summarised in Table 1.3, defines the so-called Phenomenological MSSM (pMSSM).

Table 1.3: Parameters in the pMSSM.

Parameter	Description	N. of parameters
$M_1, M_2, M_3$	Bino, Wino and gluino masses	3
$M_A$	pseudo-scalar Higgs boson mass	1
$\mu$	higgsino mass	1
$m_{\tilde{q}}, m_{\tilde{u}_R}, m_{\tilde{d}_R}$ , $m_{\tilde{Q}_L}, m_{\tilde{t}}, m_{\tilde{b}}$	first- and second-generation squark masses third generation squark masses	3 3
$m_{\tilde{l}}, m_{\tilde{e}_R}$ , $m_{\tilde{L}}, m_{\tilde{\tau}_R}$	first- and second-generation slepton masses third-generation slepton masses	2 2
$A_t, A_b, A_\tau$	third-generation trilinear couplings	3
$\tan \beta$	two-higgs-doublet fields VEVs ratio	1

Such parameter space is still rather large and it makes pMSSM searches extremely challenging and difficult to exclude. To overcome this problem *simplified models* are introduced. In other words, a certain signal process is extracted from the model and only particles contributing to a certain decay mode will be considered, e. g.  $\tilde{t}_1 \rightarrow t + \tilde{\chi}_1^0$  only targets the 2-body decay ignoring the remaining SUSY mass spectrum. The number of parameters will then boil down to 2;  $m_{\tilde{t}}$  and  $m_{\tilde{\chi}^0}$ , allowing the reinterpretation of the results and providing a powerful tool to constrain various models.

In this work only analyses based on such simplified models will be presented.

### Phenomenology of the top squark

Figure 1.6 shows SUSY particles production cross-sections in  $pp$  collisions at  $\sqrt{s} = 13$  TeV for squarks that do not contribute to gluino production diagrams and vice versa, i. e. treating squarks

and gluinos as *decoupled* making the cross-section of squark pair-production be the same for all families. While gluino pair-production cross-sections are fairly large, SUSY electroweak production cross-sections of neutralinos and charginos are considerably lower. Slepton production cross-section, which is not displayed, would sit just below higgsino-like chargino/neutralino production cross-section.

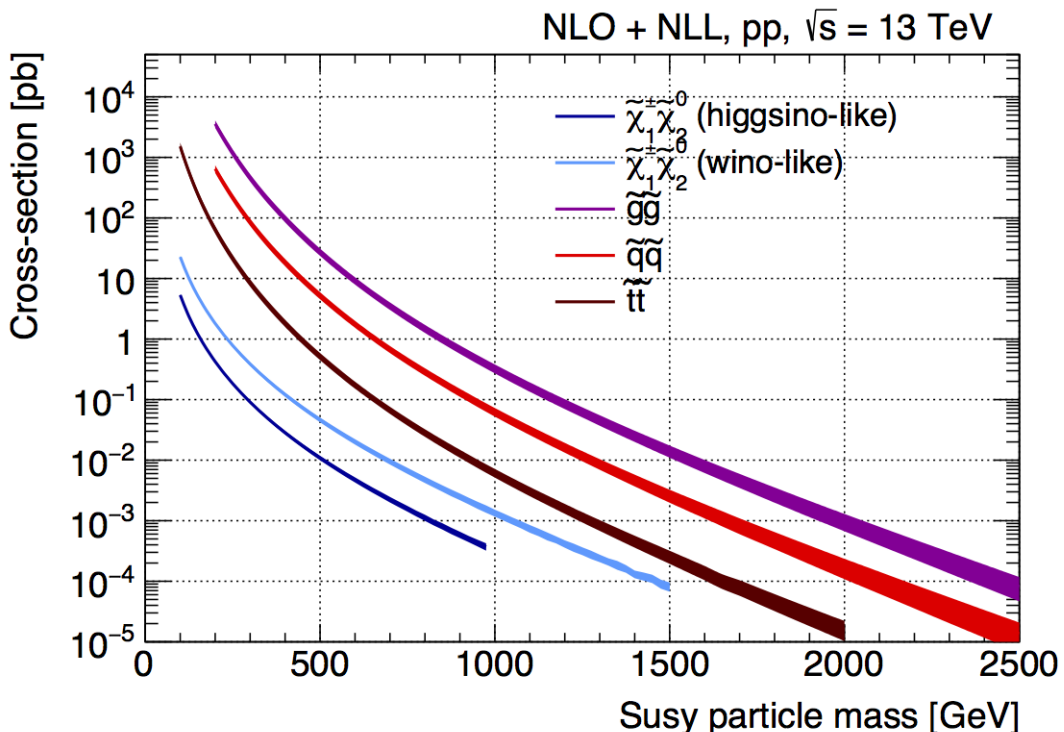


Figure 1.6: NLO+NLL production cross-sections as a function of mass at  $\sqrt{s} = 13$  TeV [28]

There exists various decay modes of pair-produced stops, depending on the masses of the decay products;

- $\tilde{t} \rightarrow t \tilde{\chi}_1^0$
- $\tilde{t} \rightarrow b \tilde{\chi}_1^\pm \rightarrow b W \tilde{\chi}_1^0$  (on/off-shell  $W$ ) or  $\tilde{t} \rightarrow b W \tilde{\chi}_1^0$  (off-shell top)
- $\tilde{t} \rightarrow c \tilde{\chi}_1^0$
- $\tilde{t} \rightarrow b f f' \tilde{\chi}_1^0$

Figure 1.7 shows a schematic representation of the parameter space  $(m_{\tilde{t}_1}, m_{\tilde{\chi}_1^0})$  and the different region where each of the above-mentioned process dominates.

In the models considered in this work, either  $\tilde{\chi}_2^0$  or  $\tilde{\chi}_1^\pm$  is assumed to be the so-called Next Lightest Supersymmetric Particle (NLSP). Three different decay scenarios were considered in this work; (a) where both top squarks decay via  $\tilde{t} \rightarrow t^{(*)} \tilde{\chi}_1^0$ <sup>5</sup>; (b) at least one of the stops decays

<sup>5</sup> The symbol (\*) indicates the off-shell production

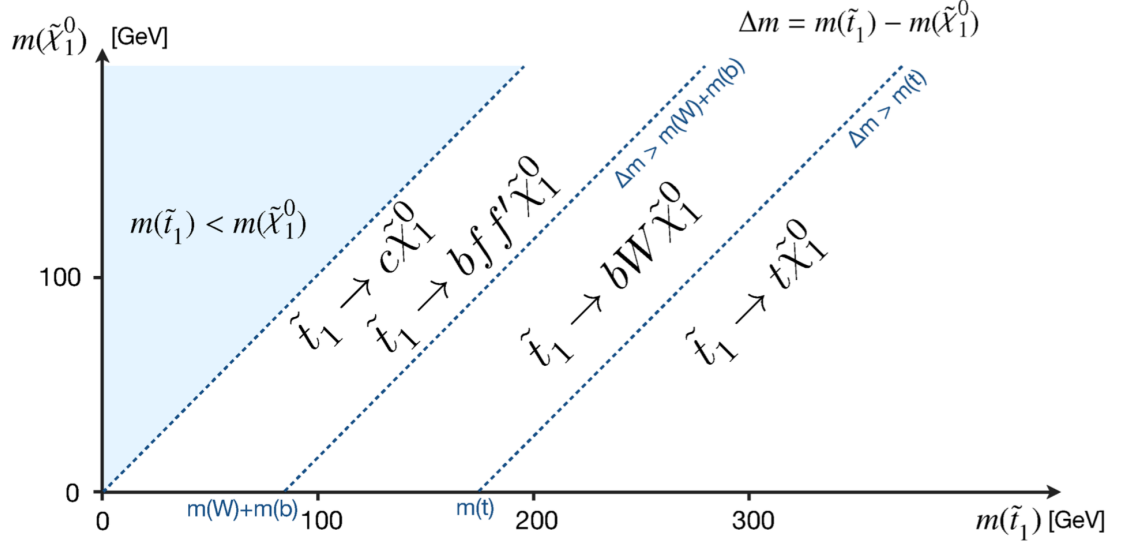


Figure 1.7: Illustration of stop decay modes in the  $(m_{\tilde{t}_1}, m_{\tilde{\chi}_1^0})$  mass place where the  $\tilde{\chi}_1^0$  is assumed to be the lightest supersymmetric particle. The dashed blue lines indicate thresholds separating regions where different processes dominate.

via  $\tilde{t} \rightarrow b \tilde{\chi}_1^\pm \rightarrow b W^{(*)} \tilde{\chi}_1^0$ ; (c) where  $m_{\tilde{\chi}_2^0}$  is small enough to allow one stop to decay via  $\tilde{t} \rightarrow t \tilde{\chi}_2^0 \rightarrow h/Z \tilde{\chi}_1^0$ . Here,  $h$  is the SM Higgs boson (125 GeV), as illustrated in Figure 1.8(a)–(c), respectively. Furthermore, top squarks can also be indirectly produced through the so-called gluino-mediated stop production, as shown in Figure 1.8(d).

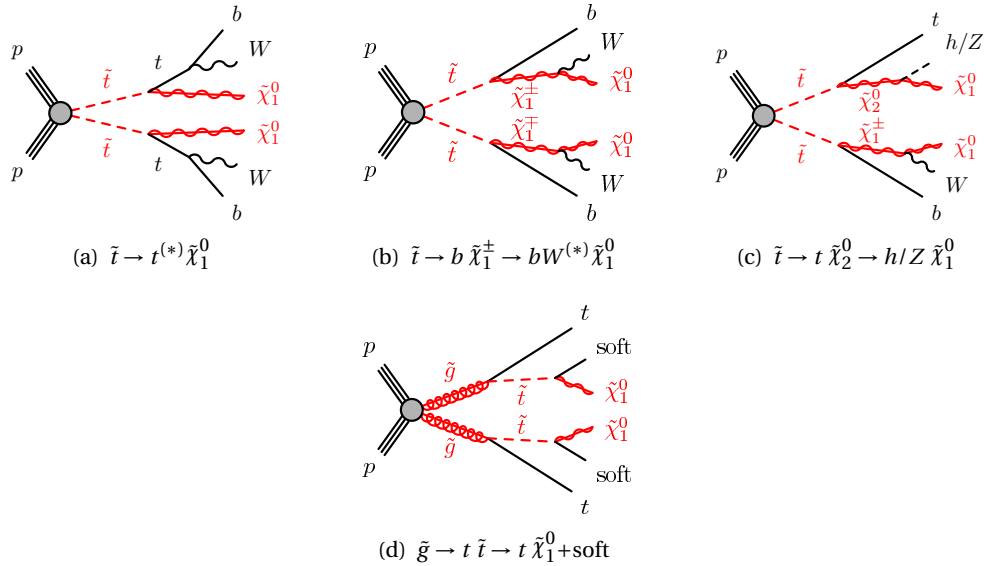


Figure 1.8: Diagrams of the decay topologies of the signal models considered in this work. The term “soft” refers to decay products that have transverse momenta below the detector thresholds.

Third-generation SUSY analyses, e. g. stop pair-production ( $\tilde{t}\tilde{t}$ ) or sbottom pair-production ( $\tilde{b}\tilde{b}$ ) are very challenging, due to the cross-section being around a factor of six smaller than  $t\bar{t}$  production (when  $m_{\tilde{t}_1} \sim m_t$ ), which usually is one of the main backgrounds. Furthermore, the cross-section of such processes dramatically decreases with increasing  $m_{\tilde{q}}$ . Nonetheless, for

example, searches for direct  $\tilde{t}_1$  production with  $\tilde{t}_1 \rightarrow t + \tilde{\chi}_1^0$  are sensitive in a scenario where  $m_{\tilde{t}_1} \gg m_t + m_{\tilde{\chi}_1^0}$  as the large  $E_T^{\text{miss}}$ , from the neutralinos, provides discriminating power for  $t\bar{t}$  rejection. Further details will be discussed in Chapter 5.

# THE ATLAS EXPERIMENT AT THE LHC

2

*We are rather like children, who  
must take a watch to pieces to see  
how it works.*

---

Sir Ernest Rutherford

A Toroidal LHC ApparatuS ([ATLAS](#)) (A Toroidal LHC ApparatuS) is one of the four main experiments<sup>1</sup> taking data at a centre-of-mass energy of 13 TeV using beams delivered by the [LHC](#). In this chapter an overview of the [LHC](#) will be given in Section 2.1, then the [ATLAS](#) detector will be described in Section 2.2, and finally the Trigger system, used to cleverly select the data, will be described in Section 2.3. A more in-depth description of the Trigger algorithms the author has been involved in will be given in Chapter 3.

## 2.1 The LHC

As of today, the [LHC](#) [29] is the world's largest and most powerful particle accelerator. It was designed to help answer some of the fundamental open questions in particle physics by colliding protons at an unprecedented energy and luminosity. It is located at [CERN](#), in the Geneva area, at a depth ranging from 50 to 175 metres underground. It consists of a 27-kilometre ring made of superconducting magnets, and inside it two high-energy particle beams travel in opposite directions and in separate beam pipes.

The beams are guided around the ring by a strong magnetic field generated by coils - made of special electric cables - that can operate in a superconducting regime. A total of 1232 superconducting dipole and 392 quadrupole magnets, with an average magnetic field of 8.3 T, are employed and kept at a temperature below 1.7 K, in order to preserve their superconducting properties. The former are used to bend the beams and the latter to keep them focused while they get accelerated.

---

<sup>1</sup> [ATLAS](#), Compact Muon Solenoid ([CMS](#)), A Large Ion Collider Experiment ([ALICE](#)), Large Hadron Collider beauty ([LHCb](#))

The collider first went live on September 2008 even though, due to a magnet quench incident that damaged over 50 superconducting magnets, it has been fully operational since November 2009 when low-energy beams circulated in the tunnel for the first time since the incident. This also marked the start of the main research programme and the beginning of the so-called Run 1: first operational run (2009 - 2013).

## Performance of the LHC

In June 2015 the [LHC](#) restarted delivering physics data, after a two-year upgrade programme, the so-called Long Shut down 1 ([LS1](#)), during which the magnets were upgraded to handle the current required to circulate 7-TeV beams. It was the beginning of the so-called Run 2 - second operational run (2015-2018) - during which the [LHC](#) has collided up to  $10^{11}$  bunches of protons every 25 ns at the design luminosity<sup>2</sup> of  $2 \cdot 10^{34} \text{ cm}^{-2} \text{ s}^{-1}$ . The definition of the luminosity is:

$$\mathcal{L} = f \frac{n_b N_1 N_2}{4\pi \sigma_x \sigma_y} \quad (2.1)$$

where  $N_1$  and  $N_2$  are the number of protons per bunch in each of the colliding beams,  $f$  is the revolution frequency of the bunch collisions,  $n_b$  the number of proton per bunch, and  $\sigma_x$  and  $\sigma_y$  are the horizontal and vertical dimensions of the beam. The luminosity is strictly related to the number of collisions occurring during a certain experiment via the following:

$$\mathcal{N}_{\text{event}} = \mathcal{L} \sigma_{\text{event}} \quad (2.2)$$

where  $\sigma_{\text{event}}$  is the cross section of the process under investigation. It has not only collided protons but also heavy ions, in particular lead nuclei at  $\sqrt{s_{NN}} = 5.02 \text{ TeV}$ , at a luminosity of  $10^{27} \text{ cm}^{-2} \text{ s}^{-1}$  [30].

## Acceleration stages

Before reaching the maximum energy, the proton beams are accelerated by smaller accelerators through various stages. Figure 2.1 shows a sketch of the [CERN](#)'s accelerator complex. It all begins with the Linear Accelerator 2 ([LINAC2](#)). Here protons are accelerated up to 50 MeV, and then injected in the Proton Synchrotron Booster ([PSB](#)) where they reach 1.4 GeV. The next stage is the Proton Synchrotron, which boosts the beams up to 25 GeV and then Super Proton Synchrotron ([SPS](#)) makes them reach energies up to 450 GeV. Eventually, the beams are injected in bunches with a 25 ns spacing into the [LHC](#), where they travel in opposite directions, while they are accelerated to up to a centre-of-mass energy of 13 TeV. Once the bunches reach the maximum energy, they are made collide at four different points, inside four experiments around the ring [29].

---

<sup>2</sup> the highest luminosity the detector was designed to cope with

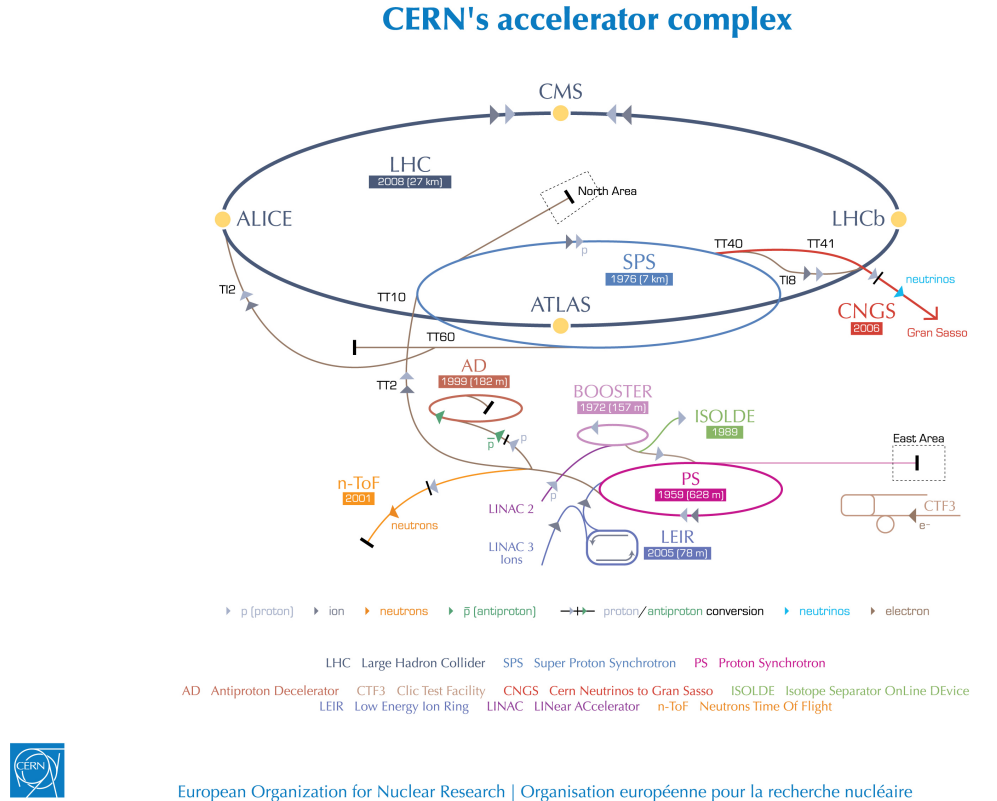


Figure 2.1: **CERN** Accelerator complex. The **LHC** is the last ring (dark grey line). Smaller machines are used for early-stage acceleration and also to provide beams for other experiments [31].

The heavy ion beams acceleration procedure is slightly different. Their journey starts at Linear Accelerator 3 (LINAC3), and the Low Energy Ion Ring (LEIR) then, before they make their way into the Proton Synchrotron where they follow the same path as the protons.

The four large detectors on the collision points are; the multi-purpose detectors **ATLAS** [32], and **CMS** [33], **LHCb** [34], which focuses on flavour physics, and **ALICE** [35] which specialises in heavy ion physics. The *big four* are not the only experiments at the **CERN**'s accelerator complex. There also are smaller experiments based at the the four caverns about the collision points e.g. TOTal cross section, Elastic scattering and diffraction dissociation Measurement at the **LHC** (**TOTEM**) [36], Large Hadron Collider forward (**LHCf**) [37] and Monopole & Exotics Detector At the **LHC** (**MoEDAL**) [38], but these will not be discussed any further.

## 2.2 The ATLAS Detector

**ATLAS** is a general-purpose detector designed to collect data with the highest luminosity provided by the **LHC**. It is located at **CERN**'s Point 1 cavern and it measures about 45 m in length and 25 m in diameter. It has a forward-backward symmetric cylindrical geometry with respect to the interaction point and it is designed to reconstruct and measure physics objects such as electrons, muons, photons and hadronic jets. Its design was optimised to be as sensitive as possible to the discovery of the Higgs boson and Beyond Standard Model (**BSM**) physics. In fact, thanks

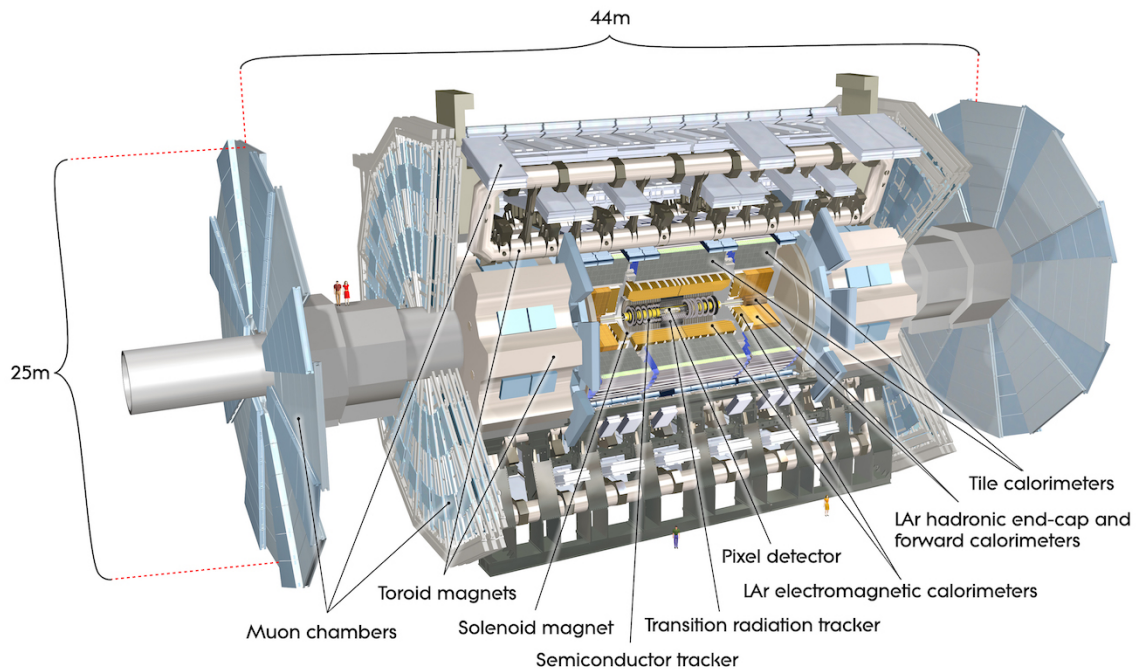


Figure 2.2: Cut-away view of the [ATLAS](#) detector. The dimensions of the detector are 25 m in height and 44 m in length. The overall weight of the detector is approximately 7000 tonnes [31].

to its various sub-systems, [ATLAS](#) is able to observe all possible decay products by covering nearly  $4\pi$  steradians of solid angle.

In Figure 2.2 a cut-away view of [ATLAS](#) with all its components is shown. The innermost layer is the Inner Detector ([ID](#)) which is the core of the tracking system and consists of a Pixel, a SemiConductor Tracker ([SCT](#)), and a Transition Radiation Tracker ([TRT](#)). It is submerged in a 2 T magnetic field, generated by a thin superconducting solenoid, which bends all the charged particles' trajectories allowing transverse momentum measurement. The electromagnetic and hadronic calorimeters form the next layer and they are both used to perform precise energy measurements of photons, electrons, and hadronic jets. Finally, the outermost layer corresponds to the Muon Spectrometer ([MS](#)), enclosed in a toroidal magnetic field, which, together with the [ID](#), allows precise measurement of momentum and position of muons. These sub-detectors will be discussed in more detail in the following sections.

### The ATLAS coordinate system

A coordinate system is taken on for the spatial definition of the sub-systems and kinematic measurement of physics processes. Such system is defined starting from the interaction point, defined as the origin. The  $z$ -axis is defined by the beam direction and the  $x - y$  plane, as transverse to the beam direction.

A quantity, known as pseudo-rapidity, ( $\eta$ ), is defined to describe the angle of a particle coming out of the collision, with respect to the beam axis:

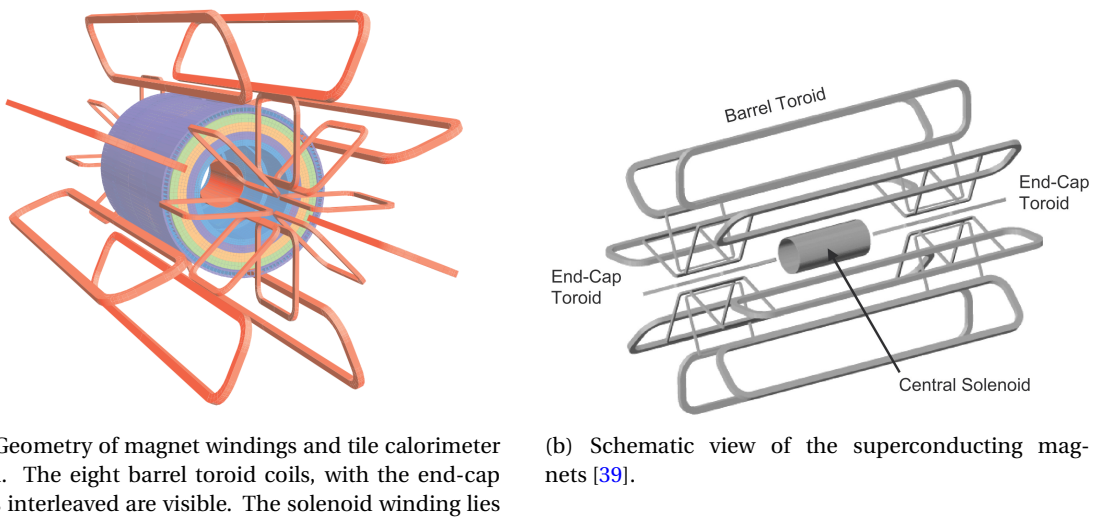
$$\eta \equiv -\ln(\tan(\theta/2))$$

Here  $\theta$  is the polar angle. The azimuthal angle,  $\phi$ , is defined around the beam axis and the polar angle. In the  $(\eta, \phi)$  space a distance  $\Delta R$  can be therefore defined as

$$\Delta R = \sqrt{\Delta\eta^2 + \Delta\phi^2}$$

where  $\Delta\eta$  and  $\Delta\phi$  are the differences in pseudo-rapidity and azimuthal angle between any two considered objects. A central and a forward region of pseudo-rapidity are also defined such that the detector components are described as part of the *barrel* if they belong to the former or as part of the *end-caps* if they belong to the latter.

### 2.2.1 The Magnet System



(a) Geometry of magnet windings and tile calorimeter steel. The eight barrel toroid coils, with the end-cap coils interleaved are visible. The solenoid winding lies inside the calorimeter volume [32].

(b) Schematic view of the superconducting magnets [39].

Figure 2.3: The ATLAS magnet system.

The ATLAS magnet system, 26 m long with a 22 m diameter, generates the magnetic field needed to bend the trajectories of charged particles in order to perform momentum measurement. Figure 2.3(a) and 2.3(b) show the geometry of the system and its components, which are made of NbTi - superconducting material - and will be described in the following paragraphs.

#### The Central Solenoid

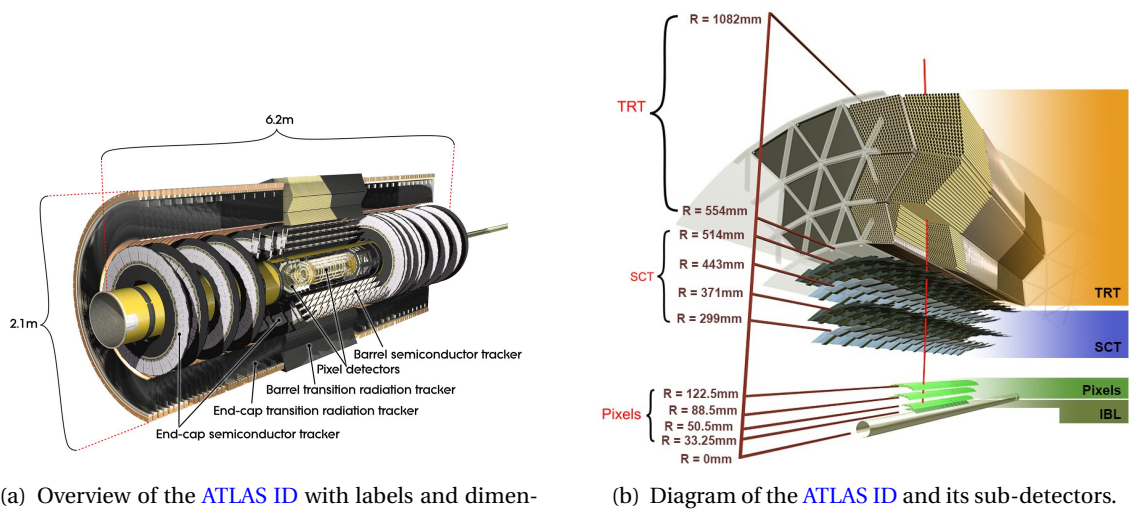
With an axial length of 5.8 m, an inner radius of 2.46 m, and an outer radius of 2.56 m, the central solenoid magnet is located between the ID and the Electromagnetic Calorimeter (ECAL). Its function is to bend the charged particles that go through the ID and it is aligned on the beam axis providing a 2 T axial magnetic field that allows accurate momentum measurement up to 100 GeV [39].

## The Barrel and the End-cap Toroids

Figure 2.3(b) displays the toroid magnetic system that surrounds the calorimeters. With its cylindrical shape this component consists of a barrel and two end-caps toroids. The barrel toroid is comprised of eight coils and produces an approximately 0.5 T toroidal magnetic field for the central muon detectors. The end-cap toroids, also comprised of eight coils each, produce an approximately 1 T toroidal magnetic field, which is required to provide bending power for the end-cap regions of the muon spectrometer.

### 2.2.2 The Inner Detector

The ID [40] is the innermost component of the ATLAS detector i. e. the nearest sub-detector to the interaction region and it is used to reconstruct charged particle tracks used in the selection of physics objects. In fact, it allows robust track reconstruction, with accurate impact parameter resolution ( $\sim 20\mu m$ ) and precise primary and Secondary Vertex (SV) reconstruction for charged particles (tracks) above 500 MeV and within  $|\eta| < 2.5$ .



(a) Overview of the ATLAS ID with labels and dimensions.

(b) Diagram of the ATLAS ID and its sub-detectors.

Figure 2.4: The ATLAS Inner Detector

The ID is comprised of independent and concentric sub-systems, which are all shown in Figure 2.4:

#### Insertable B-Layer (IBL):

innermost Pixel Detector layer added during ATLAS Run 2 upgrade (2013/2014) to improve vertexing, by a factor  $\sim 1.4$ , and impact parameter reconstruction, by a factor 2;

#### Silicon Pixel Tracker (Pixel):

made of silicon pixel layers and used mainly for reconstructing both the primary and secondary vertices in an event;

**SCT:**

comprised of silicon micro-strip layers; thanks to its resolution ( $17 \times 580 \mu\text{m}$ ) it can accurately measure particle momenta;

**TRT:**

final layer comprised of various layers of gaseous straw tube elements surrounded by transition radiation material.

These sub-detectors will be discussed in the following sections.

**IBL**

The **IBL** [41] is the innermost Pixel Detector layer as shown in Figure 2.4(b). It is comprised of 6M channels and each pixel measures  $50 \times 250 \mu\text{m}$ . Its resolution is  $8 \times 40 \mu\text{m}$ . The addition of this new layer produced an improvement on the quality of the impact parameter reconstruction of tracks almost by a factor 2, and almost by a factor 1.4 on the resolution of the reconstructed Primary Vertex (PV), highly important e.g. for the tagging of bottom-quark-initiated jets (*b*-jets).

**Pixel**

The Pixel detector is comprised of 1750 identical sensorchip-hybrid modules, each covering an active area of  $16.4 \times 60.8 \text{ mm}$ . The total number of modules correspond to roughly 80 million semiconductor silicon pixels. The nominal pixel size is  $50 \mu\text{m}$  in the  $\phi$  direction and  $400 \mu\text{m}$  in the barrel region, along the  $z$ -axis (beam axis) [42]. The reason why such a large amount of pixels is employed is justified by the need to cope with the high luminosity in **ATLAS**. The silicon pixel detector measures 48.4 cm in diameter and 6.2 m in length providing a pseudo-rapidity coverage of  $|\eta| < 2.5$ . Figure 2.4(b) shows the three concentric barrel layers placed at 50.5 mm, 88.5 mm and 122.5 mm respectively. Furthermore, the Pixel detector is made of six disk layers, three for each forward region, such that when a charged particle crosses the layers it will generate a signal at least in three space points. The fine granularity of such detector allows accurate measurement and precise vertex reconstruction, as it provides a more accurate position measurement as a large detection area is available. In particular, it has a resolution of  $10 \times 115 \mu\text{m}$ .

**SCT**

The **SCT** is made of 4088 modules of silicon micro-strip detectors arranged in four concentric barrel layers. It is mainly used for precise momentum reconstruction over a range  $|\eta| < 2.5$  and it was designed for precision measurement of the position using four points (corresponding to eight silicon layers), obtained as track hits when crossing the layers. Figure 2.4(b) shows the structure of the **SCT** with its four concentric barrel layers with radii ranging from 299 mm

to 514 mm and two end-cap layers. Each module has an intrinsic resolution of 17  $\mu\text{m}$  in the  $R - \phi$  direction and 580  $\mu\text{m}$  in the  $z$  direction. As the **SCT** is further away from the beam-pipe than the Pixel detector, it has to cope with reduced particle density. This allows for reduced granularity maintaining the same level of performance of the Pixel detector: **SCT** can use  $\sim 6.3$  million read-out channels.

## TRT

The last and outermost of the sub-systems in the **ID** is the **TRT**. It is a gaseous detector which consists of 4 mm diameter straw tubes wound from a multilayer film reinforced with carbon fibres and containing a 30  $\mu\text{m}$  gold plated tungsten wire in the centre. The straw is filled with a gas mixture of 70% Xe, 27% CO<sub>2</sub> and 3% O<sub>2</sub> [43]. As shown in Figure 2.4(b), its section consists of three concentric layers with radii ranging from 554 mm to 1082 mm, each of which has 32 modules containing approximately 50,000 straws, 1.44 m in length, aligned parallel to the beam direction with independent read-out at both ends. The gas is ionised when a charged particle passes through it and electrons (ions) are collected at the anode (cathode). A current in the wire will be created and as the electric field in the tube is known, the distance from the wire can be calculated using the time that electrons take to drift to the wire. Furthermore, the **TRT** is capable of performing particle identification on the particles that pass through it by utilising the detection of transition radiation photons that are emitted when a highly relativistic charged particle crosses a boundary between two media with different dielectric constants. The separation between, e. g. electrons and charged pions is achieved by observing the amount of transition radiation produced, since this is dependent on how relativistic the charged particle is.

The **TRT** has an intrinsic resolution of 130  $\mu\text{m}$  and, on average, 35 hits are observed within such sub-system when a charged particle passes through.

## Performance of the ID

As previously mentioned, the tracking performed by the **ID** is indispensable to measure the properties of objects such as leptons and jets, as well as interaction vertices in a certain event and secondary vertices, which are used e. g. to identify bottom-quark-initiated jets( $b$ -jets). Both jets and  $b$ -jets are expected in the final states that are being searched for in this thesis.

The overall performance of the **ID** depends on the three sub-systems and it can be shown in terms of momentum resolution:

$$\frac{\sigma_{p_T}}{p_T} = 1.6 \pm 0.1\% \oplus \frac{(53 \pm 2) \times 10^{-5}}{\text{GeV}} \times p_T \quad (2.3)$$

measured in [44] using cosmic muons before the addition of the **IBL**. Eq. 2.3 shows that the **ID** has a momentum resolution of  $\sim 1.6\%$  at low momenta ( $\sim 1$  GeV) and of  $\sim 50\%$  at 1 TeV.

### 2.2.3 The Calorimeters

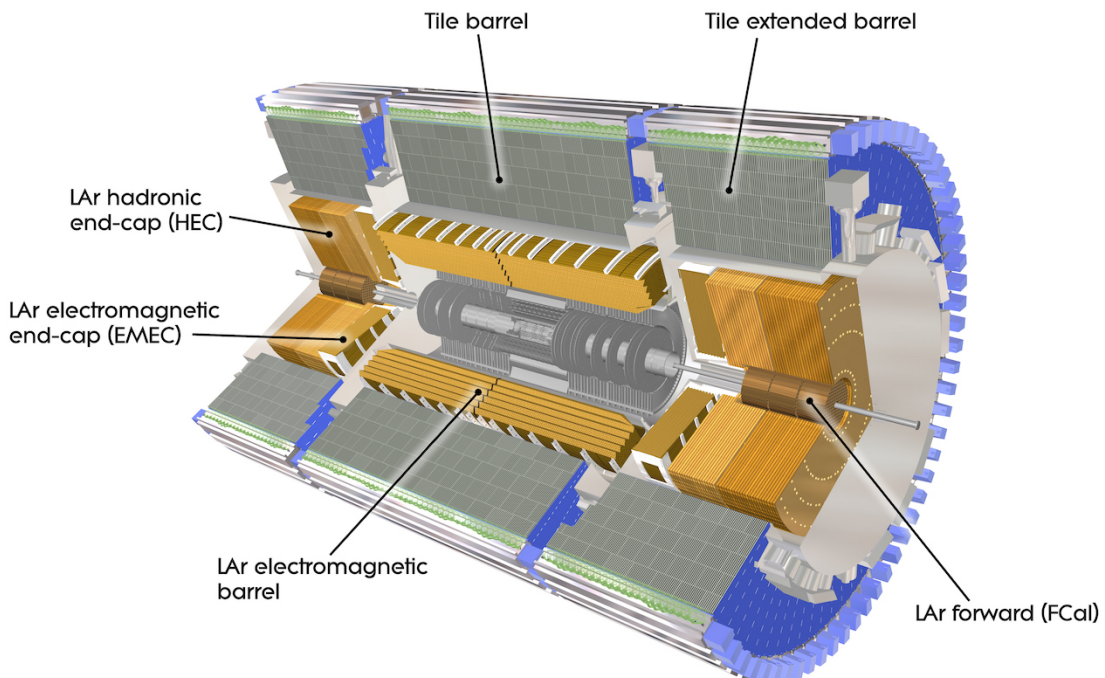


Figure 2.5: A computer generated image of the full calorimeter.

The [ATLAS](#) Calorimeter system, shown in Figure 2.5, is comprised of two main sub-systems; the [ECAL](#) and Hadronic Calorimeter ([HCAL](#)), which are designed to stop and measure the energy of electromagnetic-interacting and hadronic particles respectively. The combination of the two provides full coverage in  $\phi$  and  $|\eta| < 4.95$ . Particles slow down and lose energy generating showers when crossing different layers. The [ECAL](#) is comprised of one barrel and two end-cap sectors employing Liquid Argon ([LAr](#)). The showers hereby develop as electrons pairs which are then collected. The [HCAL](#) is also comprised of one barrel and two end-cap sectors. The sensors in the barrel of the [HCAL](#) are tiles of scintillating plastic whereas [LAr](#) is employed for the end-cap. A forward region, the closest possible to the beam, is covered by a [LAr](#) forward calorimeter ([FCal](#)). The [LAr](#) and Tile Calorimeter will be briefly discussed in the following paragraphs.

#### The Liquid Argon Calorimeter

The [ECAL](#) is comprised of multiple layers of [LAr](#) sampler and lead absorber. The choice of its accordion-geometry design brought two main advantages; full  $\phi$  coverage with no non-interactive regions (no cracks); fast extraction of signals coming from both front or rear end of the electrodes. It is made of two half-barrel wheels, both placed in the barrel cryostat, that provide a pseudo-rapidity coverage up to  $|\eta| < 1.475$  and two end-cap detectors providing  $1.375 \leq |\eta| \leq 3.20$  coverage in two end-cap cryostats. The junction between the barrel and

end cap components defines the crack region and any signal coming from the crack region is therefore discarded.

In the  $|\eta| < 1.8$  region there is an additional layer, placed at the front of the calorimeter, that is made of a thin (0.5 cm in the end-cap and 1.1 cm in the barrel) LAr layer with no absorber [45]. This additional layer was designed to correct for the energy lost, as particles enter the calorimeter, by taking a measurement just before the majority of the electromagnetic shower is developed.

### The Tile calorimeter

The main purpose of the hadronic calorimeter is to measure the energy of hadronic showers. It is built employing steel and scintillating tiles coupled to optical fibres which are read out by photo-multipliers. As shown in Figure 2.5, the HCAL is made up of three cylinders; a central barrel, 5.64 m long covering a region  $|\eta| < 1.0$ , and two extended barrel, 2.91 m long covering a region  $0.8 < |\eta| < 1.7$ . Each cylinder is made up of 64 modules and each module is in turn made up of three layers. Ultimately, the smallest section of the calorimeter module is a cell with a  $\Delta\phi \times \Delta\eta = 0.1 \times 0.1$  granularity for the two innermost layers and  $\Delta\phi \times \Delta\eta = 0.2 \times 0.1$  for the outermost one.

### Performance of the Calorimeter

The performance of the calorimeter is important to measure the properties of the jets used in the analyses presented in this thesis. This has been assessed using test beam data and, once the noise has been subtracted from the experimental measurements these are fit using Eq. 2.4

$$\frac{\sigma(E)}{E} = \frac{a}{\sqrt{E[\text{GeV}]}} \oplus b \quad (2.4)$$

Here,  $a$  is the stochastic term and  $b$  is a constant that includes local non-uniformities in the calorimeter response.

The ECAL performance in the barrel was assessed firing an electron beam at a module that is identical to those in ATLAS and the fitted energy resolution is  $\sigma(E)/E = (10 \pm 0.4)\%/\sqrt{E} \oplus (0.4 \pm 0.1)\%$  with a variation of no more than 0.7% for the entire coverage of the calorimeter.

The HCAL performance in the barrel was assessed firing a pion beam at a prototype detectors of the LAr electromagnetic and tile calorimeters. The fitted energy resolution (with an added term to account for electronic noise) is  $\sigma(E)/E = (52 \pm 1.0)\%/\sqrt{E} \oplus (3.0 \pm 0.1)\% \oplus (1.6 \pm 0.1)/E$ .

#### 2.2.4 The Muon Spectrometer

The MS [46], shown in Figure 2.6, is the outermost sub-system of the whole ATLAS detector. As such, it surrounds the calorimeters and its main function is to perform precision measurement of muons momenta. The deflection of muon tracks employing large superconducting air-core

toroid magnets and high-precision tracking chambers is at the heart of such high precision measurement.

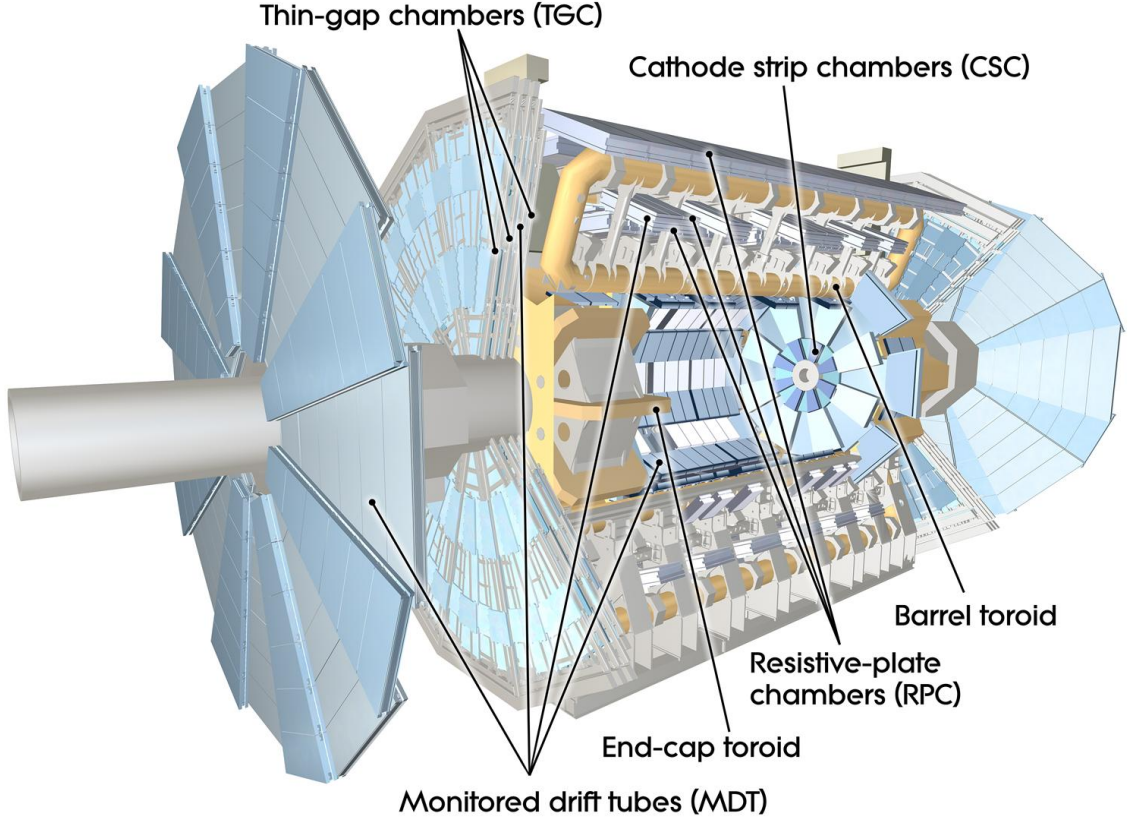


Figure 2.6: Cut-away view of the ATLAS muon system [32].

The **MS** is comprised of one large barrel toroid, covering the region  $|\eta| \leq 1.4$ , and two end-cap toroids, covering  $1.6 < |\eta| \leq 2.7$  which are employed together to achieve the track-bending effect wanted. The magnitude of the magnetic field in the barrel, generated by eight large superconducting coils, ranges from 0.5 to 2 T.

Around the beam axis, three cylindrical layers make way for the chambers, placed in planes perpendicular to the beam, used to measure tracks.

Monitored Drift Tubes (**MDTs**) are employed over most of the pseudo-rapidity range to provide precision measurement of track coordinates in the bending direction. An MDT is essentially a set of 30-mm-diameter Aluminium tubes containing a *W-Re* (Tungsten-Rhenium) wire, surrounded by a non-flammable Ar-CH<sub>4</sub>-N<sub>2</sub> mixture at a pressure of 3 bar. The resolution a single wire can give on the particle position is 80  $\mu\text{m}$  enhanced by having multiple layers of tubes for each module.

Cathode Strip Chambers (**CSCs**) are instead employed at large pseudo-rapidity ( $2 < |\eta| < 2.7$ ). They work similarly to the MDT but instead of tubes there are cathode strips above and below the anode wires. In particular, one set is orthogonal to the wires for precision measurement and the other one parallel to the wires providing a measurement of the transverse coordinate. The gas employed between the strips and wires is a non-flammable mixture of Ar-CO<sub>2</sub>-CF<sub>2</sub>.

Thin-Gap Chambers ([TGCs](#)) are employed in the end-cap region and Resistive-Plate Chambers ([RPCs](#)) in the barrel. The [TGCs](#) are very similar to the [CSCs](#). They provide large signals and in a very narrow time window making them ideal for triggering purposes.

The [RPCs](#) are also gas-based detectors. They are comprised of two parallel resistive plates held apart by insulating spacers, and a uniform electric field is employed to generate a limited avalanche multiplication centred around the primary ionisation electron. This will then be detected by *Al* strips separated from the plates by an insulating film.

## 2.3 The ATLAS Trigger System

The [ATLAS](#) Trigger System is at the heart of data taking. It is an essential component of any nuclear or particle physics experiment as it is responsible for deciding whether or not to store an event for later study. Its main function to reduce the event rate from  $\sim 40$  MHz bunch-crossing<sup>3</sup> to  $\sim 1$  kHz.

The Trigger system employs a two-level system: a first hardware-based trigger, Level-1 ([L1](#)) Trigger, and a software-based, High Level Trigger ([HLT](#)). [L1](#) processes low-granularity information from the calorimeter and the muon spectrometer and identifies the so-called Regions of Interest (RoIs)<sup>4</sup> before making a decision. Event data from other sub-system are temporarily stored in memories whilst [L1](#) decision is taken.

Further investigations are left to [HLT](#) which is made of software running on a cluster of computers ([HLT](#) farm). Additionally, a Fast TracKer ([FTK](#)) system [47] (to be installed before the end of Run 2) will process events that are accepted by [L1](#) trigger, and seed the [HLT](#) algorithms. It will provide global [ID](#) track reconstruction at the [L1](#) trigger rate using lookup tables stored in custom associative memory chips for the pattern recognition.

The [ATLAS](#) trigger system will be further discussed in Chapter 3, however the Run-1-to-Run-2 upgrade of the [ATLAS](#) trigger will not be discussed any further.

---

<sup>3</sup> The term bunch-crossing,  $\langle\mu\rangle$ , is hereby used when referring to a collision between two bunches of protons.

<sup>4</sup>  $\eta - \phi$  regions where event features have been found by the [L1](#) selection process.

# THE ATLAS TRIGGER SYSTEM

# 3

*Software is a great combination  
between artistry and engineering.*

---

Bill Gates

The [ATLAS](#) trigger system together with its performance will be presented in this chapter. A brief introduction of the reason behind the need of a trigger system, together with its implementation in [ATLAS](#), will be discussed in Section 3.1. The [L1](#) trigger and [HLT](#) will be discussed in Sections 3.2 and 3.3, respectively. Finally, Section 3.3.2 will be dedicated to the performance of [HLT](#) for low- $p_T$  single-lepton, missing transverse energy,  $E_T^{\text{miss}}$ - as the most relevant trigger for the analysis discussed in Chapter 5 -, and medium- and high- $p_T$   $b$ -jet triggers. This has been part of the *qualification task*<sup>1</sup> of the author and the results were published in a paper in the European Physics Journal [48].

## 3.1 Overview

More than  $80 \text{ fb}^{-1}$  of  $pp$  collisions were delivered in 2016 and 2017 by the [LHC](#) and, due to storage space limitations, it is not feasible to save all the information about the collision after every bunch crossing. The [ATLAS](#) Trigger System is indispensable to reduce the read-out rate to a sensible value without affecting the physics programme of [ATLAS](#), e.g. discarding potentially interesting events. A multiple-level architecture is employed to allow the trigger enough time to identify interesting events, using both software- and hardware-based real-time algorithms.

Figure 3.1 shows the Trigger and Data Acquisition ([TDAQ](#)) system. This is comprised of both a hardware-based first-level trigger ([L1](#)) and a software-based [HLT](#), as already mentioned in Section 2.3. The [L1](#) trigger decision is formed by the Central Trigger Processor ([CTP](#)), which receives inputs from the L1 Calorimeter ([L1Calo](#)) and L1 Muon ([L1Muon](#)) triggers. Once the events pass the [L1](#) selection, they are buffered in the Read-Out System ([ROS](#)) and processed by the [HLT](#), which receives information on the Region of Interest ([RoI](#)) from [L1](#) to be used for

---

<sup>1</sup> In order to become an [ATLAS](#) author every active [ATLAS](#) researcher should spend 50% of their time (in their first year), moving to 30% the year after.

track reconstruction in the trigger algorithms. An **RoI** is an extended wedge-shaped spatial region in the detector, consisting of a direction in  $\eta - \phi$  originating from a  $z$ -position along the beam-line, extended along the beam-line by independent directions with respect to this  $z$  position, and extended about the  $\phi$  direction with independent directions in pseudo-rapidity, at the maximum and minimum  $z$  positions along the beam-line.

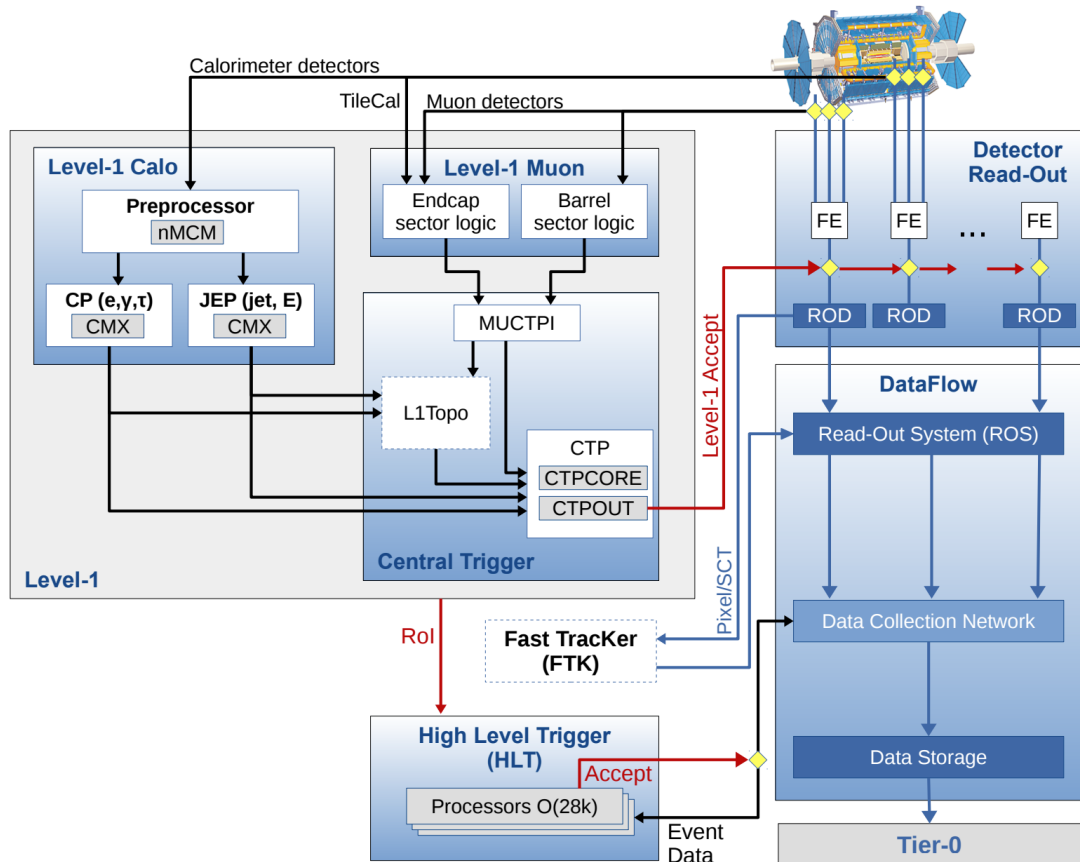


Figure 3.1: The ATLAS TDAQ system. L1Topo and FTK [48] have not been used for the results shown in this thesis.

The trigger system is configured via the so-called trigger *menu*, which contains the multiplicity requirement (number of tracks) and the pre-scale factors<sup>2</sup> for the selected events. Additionally, the menu is meant to define the trigger *chains* - usually referred to just as trigger - that start from a **L1** trigger and specify a sequence of reconstruction and selection steps for the specific trigger signatures required in the trigger chain. This is named after the following convention:

TriggerLevel\_TypeAndThreshold\_Identification\_Isolation

Here, “TriggerLevel” refers to either **L1** or **HLT**, “TypeAndThreshold” refers to the type of object to trigger on (electron, muon,  $E_T^{\text{miss}}$ , etc.) and its energy threshold. If any identification and/or isolation criteria are included, these are appended at the end of the name, e.g.:

<sup>2</sup> A factor associated with a trigger at each level that indicates what fraction of events, that could pass this trigger selection, is actually accepted.

HLT\_e24\_1hmedium is an electron trigger with a 24 GeV threshold, using “medium” identification criteria, which will be further discussed in Chapter 4.

## 3.2 Level-1 Trigger

The L1 trigger decision is essentially taken by the CTP, based on the information the L1 calorimeter and L1 muon trigger systems. Additionally, a Level-1 Topological (L1Topo) trigger<sup>3</sup>, fed with energy and direction information about the objects found by the L1Calo and L1Muon triggers, is employed [32, 48, 49].

The L1 trigger system is implemented in fast custom electronics to keep the decision time around  $2.5 \mu\text{s}$  and its decision is used as a *seed* for HLT.

### The L1 Calorimeter Trigger

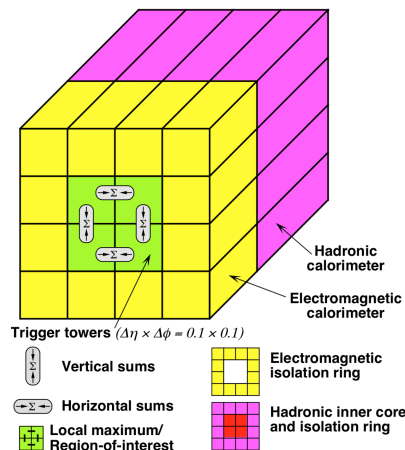


Figure 3.2: Illustration of the electron/photon and tau algorithms with the sums to be compared to programmable thresholds (from [50]).

The L1Calo trigger [32, 51] is based on inputs from the electromagnetic and hadronic calorimeters within the region  $|\eta| < 4.9$ . It provides triggers for objects such as electrons/photons, taus, jets, and global transverse energy. Dedicated analogue trigger signals, provided by the ATLAS calorimeters independently from the signals read out and used at the HLT and offline, make the L1Calo trigger decision, which is based on the information from analogue sums of calorimeter elements, called *trigger towers*, instead of using the full granularity of the calorimeter. The trigger towers have a size of approximately  $\Delta\eta \times \Delta\phi = 0.1$  in the central part of the calorimeter,  $|\eta| < 2.5$ , and they get larger and less regular in the forward region. Separate trigger towers are employed for electromagnetic and hadronic calorimeters. Furthermore, two processor systems run the trigger algorithms, once the signals have been digitised: the first, called *cluster processor*, uses the full L1 trigger granularity information in the central region to look for small and localised clusters, which are typical a energy deposit left by an electron, photon or tau; the second, the *jet and energy-sum processor*, uses  $2 \times 2$  sums of trigger towers (jet elements), to identify jet candidates and form missing transverse energy,  $E_{\text{T}}^{\text{miss}}$ , and total transverse energy,  $E_{\text{T}}$ . As an example, Figure 3.2 shows a sketch of the electron/photon and tau triggers. The trigger algorithm identifies a Region of Interest as a  $2 \times 2$  trigger tower cluster in the electromagnetic calorimeter for which

<sup>3</sup> Two FPGA-based (Field-Programmable Gate Arrays) processor modules

the transverse-energy sum, released in at least one of the four possible pairs of nearest neighbour towers ( $1 \times 2$  or  $2 \times 1$ ), exceeds a pre-defined threshold. Additionally, jets **RoI**s are defined as  $4 \times 4$ ,  $6 \times 6$  or  $8 \times 8$  trigger-tower windows for which the summed electromagnetic and hadronic transverse energy exceeds pre-defined thresholds and which surround a  $2 \times 2$  trigger tower core that is a local maximum that will be also used to define the coordinates of the jet **RoI**.

## The L1 Muon Trigger

The **L1Muon** trigger system [52] processes input data from fast muon trigger sub-detectors and its main task is to select muon candidates with a  $p_T$  threshold of 6 GeV and identify the bunch crossing in which they were produced.

Figure 3.3 shows how muons are triggered at **L1**. The **RPC** system in the barrel region ( $|\eta| < 1.05$ ) and the **TGC** system in the end-cap regions ( $1.05 < |\eta| < 2.4$ ) are employed. They provide a rough measurements of muon-candidate  $p_T$ ,  $\eta$ , and  $\phi$ . Three planes in the barrel and three in each endcap form the trigger chambers. Each plane is comprised of two to four layers and muon candidates are identified by forming coincidences between the muon planes. Coincidences are formed requiring hits that lie within parametrised geometrical muon *roads*. A road, as the example shown in Figure 3.3, essentially contains the trajectories, from the interaction point, of either positively or negatively charged muons with a  $p_T$  above a given threshold. In particular six programmable  $p_T$  thresholds are employed at **L1**, divided into two sets: three low- $p_T$  thresholds meant to cover values up to 10 GeV, and three high- $p_T$  thresholds meant to cover  $p_T > 10$  GeV.

## The CTP

The **CTP** [32] applies the multiplicity requirements and pre-scale factors specified in the trigger menu to the inputs from the **L1** trigger systems and forms the **L1** trigger decision. Timing and control signals<sup>4</sup> are employed to distribute the **L1** trigger decision to all **ATLAS** sub-detector readout systems. The **CTP** is responsible for applying the so-called *preventive dead-time*, meant to limit the minimum time between two consecutive **L1** accepts (*simple dead-time*),  $\mathcal{O}(100\text{ns})$ , in order to both avoid overlapping readout windows, and restrict the number of **L1** accepts allowed in a given number of bunch-crossings (*complex dead-time*) to avoid buffers from overflowing. In addition, a *busy dead-time*, can be introduced by **ATLAS** sub-detectors to temporarily throttle the trigger rate. These dead-times are used to monitor the total **L1** trigger rate, and individual trigger rates that need to be monitored before and after any pre-scales and/or any vetoes that have been applied. Furthermore, such information is also used to provide a measure of the **L1** dead-time, which has to be accounted for when determining the luminosity [50].

---

<sup>4</sup> The timing signals are defined with respect to the **LHC** bunch crossings: a 25 ns time window centred on the instant at which a proton bunch might cross the **ATLAS** interaction point.

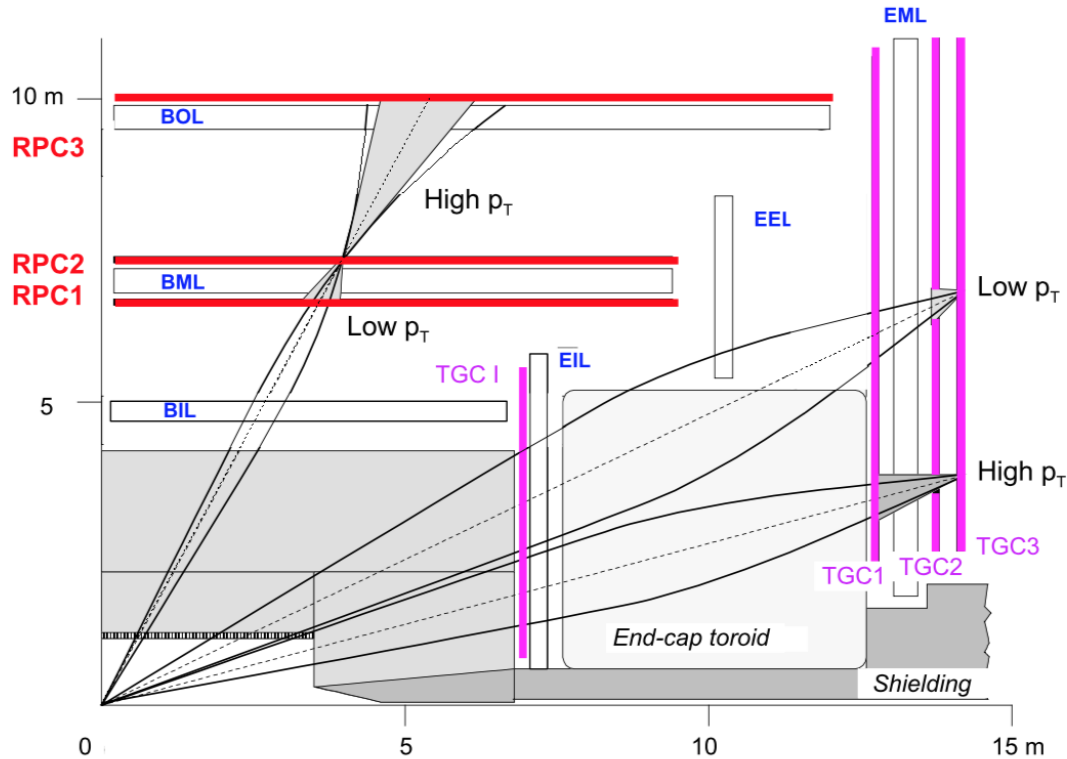


Figure 3.3: A schematic view of the [L1Muon](#) trigger chambers (from [50]).

### 3.3 High-Level Trigger

The events that are accepted by [L1](#) are then buffered in the [ROS](#) and processed by the *High-Level Trigger* using information that is not available at [L1](#), such as finer-granularity calorimeter inputs, precision measurements from the [MS](#) and tracking information from the [ID](#). [HLT](#) receives [RoI](#) from [L1](#) and performs the reconstruction within them. As needed, the reconstruction performed by the [HLT](#) software can either be run within [RoI](#)s or performing a so-called *full scan* of the detector. In order to reduce the processing time, a two-stage approach is employed for most [HLT](#) triggers: a first reconstruction (fast) to reject the majority of events; a second precision reconstruction for the remaining events (slower). Events that are accepted by the [HLT](#) get transferred to local storage at the experimental site and exported to the [CERN](#)'s computing centre for offline reconstruction [48].

#### 3.3.1 Inner detector tracking

The track reconstruction in the Inner Detector is a vital component of the trigger decision in the [HLT](#). A robust reconstruction of particle trajectories is an essential prerequisite for triggering on electrons, muons, taus, and  $b$ -jets. Furthermore, it is also used for triggering on inclusive  $pp$  interactions and for the on-line determination of the beam spot<sup>5</sup> where the reconstructed

<sup>5</sup> The luminous region produced by the collisions of proton beams.

tracks provide the input for vertex reconstruction.

The ID tracking in the trigger also includes information from the IBL, which significantly improves the tracking performance and in particular the impact parameter resolution [41]. The tracking algorithms are called *Fast Tracking* and *Precision Tracking*. The former is comprised of trigger-specific pattern recognition algorithms, unlike the latter which is heavily based on offline-tracking algorithms. As already mentioned, once an **RoI** has been identified by **L1**, the algorithms are typically configured to run within it. Furthermore, in order to reduce Central Processing Unit (**CPU**) usage, the offline track-finding is seeded with tracks and space-points identified by fast tracking stage seeds. The running of the full **HLT** reconstruction for each event on an individual node allows for the two stages of the trigger, e. g.  $b$ -jet triggers, which will be discussed in Section 3.3.2, to share the data preparation so detector information only needs to be read out once.

In order to reduce the detector volume of **RoI**, an advanced multi-stage approach, in particular for tau and  $b$ -jet tracking, is employed. The first stage is to identify leading tracks within an **RoI**, long in  $z$  but narrow in  $\eta$  and  $\phi$ , by running the Fast Track Finder (**FTF**) algorithm. The leading tracks are used to construct a second-stage **RoI**, constrained in both  $\eta$  and  $\phi$ , but very tightly constrained in polar angle and with a small  $z$  position width. The **FTF** is then run again within the wider second-stage **RoI**, followed by the Precision Tracking [48, 53]. The second stage, the Precision Tracking, is heavily based on an optimised subset of the tracking algorithms used off-line, which is slower than the first but, in return, it identifies objects constructed starting from the inner detector tracks.

### 3.3.2 Performance of HLT

The performance of the tracking was estimated using 13-TeV  $pp$  collision events collected in July 2015 by the **ATLAS** detector (unless otherwise stated). In order to be as unbiased as possible, specific monitoring triggers that do not require a track to be present for the event to be accepted are used to estimate the efficiency of the tracking algorithms. All the quantities used to estimate the performance of the tracking, i. e. efficiencies, residuals and resolutions, are calculated with respect to the tracks found by the offline reconstruction software. In particular, the efficiency is defined as the fraction of offline reference tracks that are matched to a trigger track

$$\mathcal{E} = \frac{N_{\text{trigger}}}{N_{\text{offline}}} \quad (3.1)$$

The tracking efficiency has been estimated for electrons and muons for the single-stage tracking, and for  $b$ -jets for the multi-stage approach, as part of the author's qualification task. The reconstructed tracks are required to have at least two (six) Pixel (**SCT**) clusters and lie within the region  $|\eta| < 2.5$ . The closest trigger track within a cone of size  $\Delta R = \Delta\eta^2 + \Delta\phi^2 = 0.05$  of the offline reconstructed track is selected as the matching trigger track.

## Electrons

Figure 3.4 shows the tracking efficiency for the 24 GeV electron trigger as a function of  $\eta$  and  $p_T$  of the offline track. The tracking efficiency is measured with respect to offline tracks with  $p_T > 20$  GeV for tight offline electron candidates from the 24 GeV electron support trigger, which does not use the trigger tracks in the selection, despite being identical to the physics trigger. The FTF and Precision Tracking efficiencies are all above 99% within the whole pseudo-rapidity range. The small efficiency drop at low  $p_T$  is due to bremsstrahlung energy loss by electrons [48].

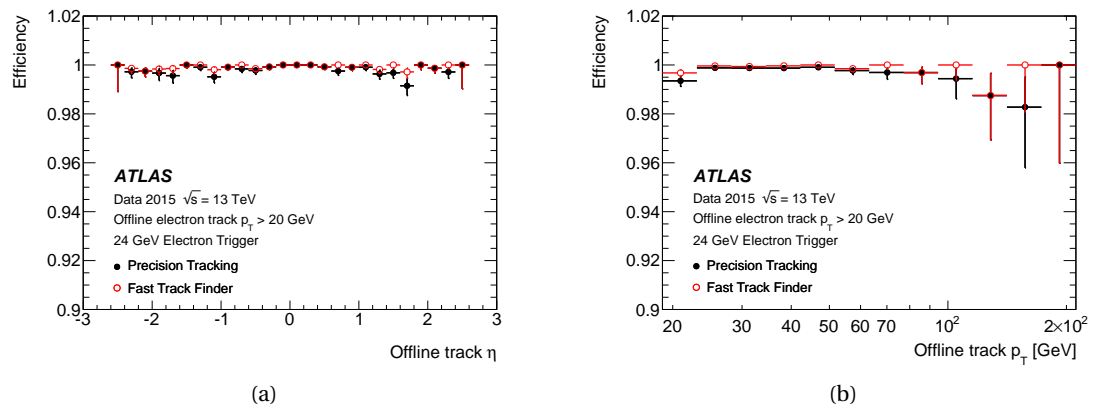


Figure 3.4: The ID tracking efficiency for the 24 GeV electron trigger is shown as a function of the (a)  $\eta$  and (b)  $p_T$  of the track of the offline electron candidate. Uncertainties based on Bayesian statistics are shown (from [48]).

## Muons

Figure 3.5(a) shows the muon tracking performance with respect to offline muon candidates with  $p_T > 6$  GeV selected by the 6 GeV muon support trigger as a function of the offline muon  $p_T$ . The efficiency is well above 99% in the entire  $p_T$  range for both FTF and Precision Tracking. Figure 3.5(b) shows the resolution of the transverse track impact parameter with respect to offline as a function of the offline muon  $p_T$ . FTF and Precision Tracking resolutions are better than 17 and 15  $\mu\text{m}$ , respectively, for muon candidates with offline  $p_T > 20$  GeV. The difference ( $\sim 10\%$ ) between the two algorithms is driven by the fact that Precision Tracking (black solid points) uses the space points found by the FTF (red open points), but refits them using the offline algorithm. In other words, Precision Tracking runs a faster version of the full offline track fit and it performs better.

## *b*-jets

As previously mentioned, the *b*-jet triggers tracking algorithms are run in a larger RoI than for electrons or muons and in order to limit CPU usage, multiple stage track reconstruction was implemented and deployed during Run-2.

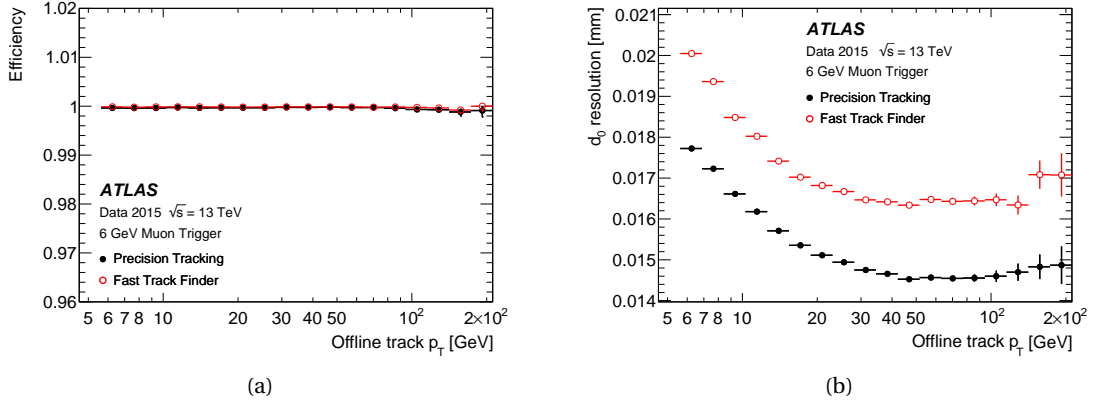


Figure 3.5: The ID tracking performance for the 6 GeV muon trigger; (a) efficiency as a function of the offline reconstructed muon  $p_T$ , (b) the resolution of the transverse impact parameter,  $d_0$  as a function of the offline reconstructed muon  $p_T$ . Uncertainties based on Bayesian statistics are shown (from [48]).

First, the leading track and its position along the beam-line are determined by executing fast tracking in an **RoI** that is fully extended along the beam-line, in the  $|z| < 225$  mm region, but narrow (0.1) in both  $\eta$  and  $\phi$ , as shown in the blue-shaded region in Figure 3.6. The second stage is then run, using this position along the beam-line, to reconstruct all tracks in an **RoI** that is larger (0.4) in both  $\eta$  and  $\phi$  but limited to  $|\Delta z| < 10$  mm with respect to the leading track, as shown by the green-shaded region in Figure 3.6.

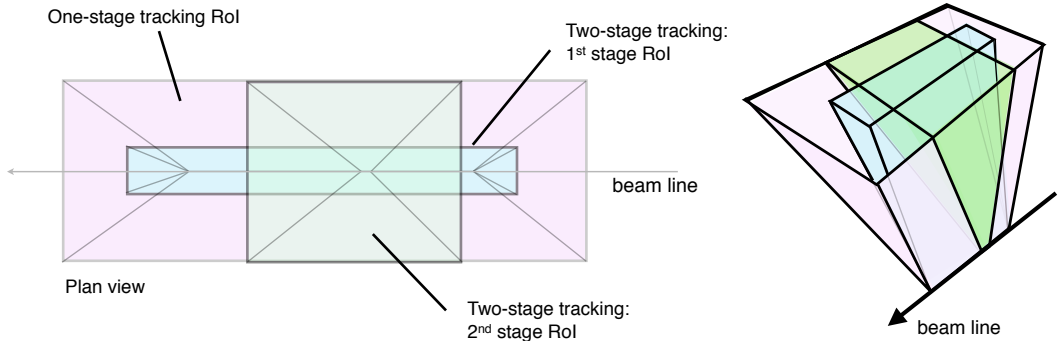


Figure 3.6: An illustration of the **RoIs** from the single-stage and two-stage tau lepton trigger tracking, shown in plan view (x-z plane) along the transverse direction and in perspective view. The z-axis is along the beam line. The combined tracking volume of the 1<sup>st</sup> and 2<sup>nd</sup> stage **RoI** in the two-stage tracking approach is significantly smaller than the **RoI** in the one-stage tracking scheme (from [48]).

The first-stage vertex tracking takes all jets identified by the jet trigger with  $\eta > 30$  GeV and reconstructs tracks with the **FTF** in a narrow region in  $\eta$  and  $\phi$  around the jet axis for each jet, but with  $|z| < 225$  mm along the beam line.

Following this step, the primary vertex reconstruction [54] is performed using the tracks from the fast tracking stage. This vertex is used to define wider **RoIs** around the jet axes, with  $|\Delta\eta| < 0.4$  and  $|\Delta\phi| < 0.4$  but with  $|\Delta z| < 20$  mm relative to the primary vertex  $z$  position. These **RoIs** are then used for the second-stage reconstruction that runs the fast track finder in the wider  $\eta$  and  $\phi$  regions followed by the Precision Tracking, secondary vertexing and  $b$ -tagging

algorithms, which will not be discussed in this work.

The performance of the primary vertexing in the  $b$ -jet vertex tracking can be seen in Figure 3.7(a), which shows the vertex finding efficiency with respect to offline vertices in jet events with at least one jet with transverse energy above 55, 110, or 260 GeV and with no additional  $b$ -tagging requirement. The efficiency is shown as a function of the number of offline tracks with  $p_T > 1$  GeV that lie within the boundary of the wider ROI (defined above) from the selected jets. The efficiency rises sharply and is above 90% for vertices with three or more tracks, and rises to more than 99.5% for vertices with five or more tracks. The resolution in  $z$  with respect to the offline  $z$  position as shown in Figure 3.7(b) is better than 100  $\mu\text{m}$  for vertices with two or more offline tracks and improves to 60  $\mu\text{m}$  for vertices with ten or more offline tracks.

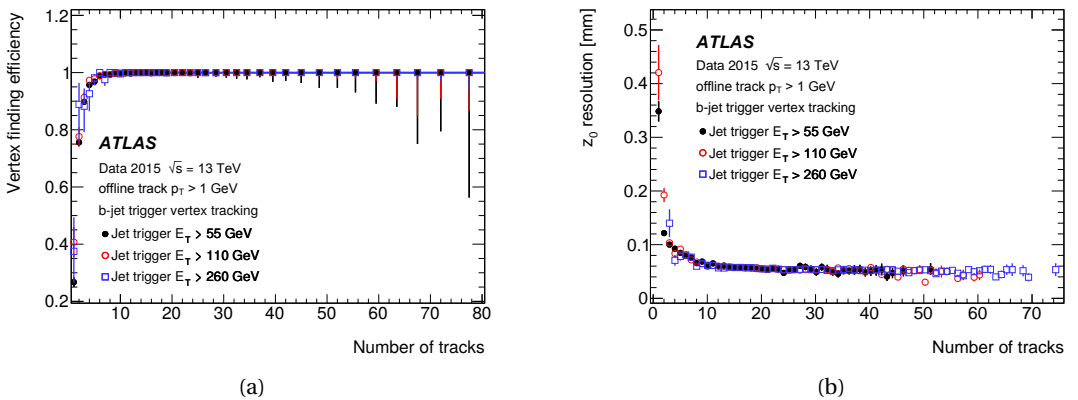


Figure 3.7: The trigger performance for primary vertices in the  $b$ -jet signatures for 55, 110 and 260 GeV jet triggers; (a) the vertexing efficiency as a function of the number of offline tracks within the jets used for the vertex tracking, (b) the resolution in  $z$  of the vertex with respect to the offline vertex position as a function of the number of offline tracks from the offline vertex (from [48]).

### Missing Transverse Energy, $E_T^{\text{miss}}$

There exists several algorithms to reconstruct the  $E_T^{\text{miss}}$  at the HLT. The *missing  $H_T$* <sup>6</sup> (MHT) algorithm calculates  $E_T^{\text{miss}}$  as the negative sum of transverse energy of calibrated jets, constructed from calibrated topological clusters of calorimeter cells. This algorithm is the most relevant to the analysis presented in Chapter 5. The *cell algorithm* is based on the negative sum of transverse energy deposited in calorimeter cells above a certain noise threshold. Unlike the cell algorithm, which calculates  $E_T^{\text{miss}}$  on the electromagnetic scale, the MHT algorithm looks at jets calibrated using jet energy scale, so that numerical threshold values for similar signal efficiencies differ. *Pufit*, a third algorithm, was employed to disentangle calorimeter deposits from the hard-scatter, from those originating from pile-up interactions by grouping towers made out of topological clusters into a pile-up and a hard-scatter category. This grouping is based on their energy, where the threshold itself is dependent on the overall event activity measured by the total energy deposited in the calorimeter. The assumption is that the contribution to  $E_T^{\text{miss}}$  due

<sup>6</sup>  $H_T$  is the scalar sum of the various  $p_{\text{T}}$ s in the event,  $H_T = \sum_i p_T^i$ .

to pile-up interactions is zero. Nevertheless a minimisation, which takes into account resolution terms, determines an effective energy density from pile-up interaction which allows a vanishing contribution to  $E_T^{\text{miss}}$  by the pile-up calorimeter towers. This correction is then subtracted from the hard-scatter towers. The negative sum of transverse energy of those pile-up corrected hard-scatter towers will provide the final  $E_T^{\text{miss}}$  value [55].

Figure 3.8 shows the turn-on curves for various  $E_T^{\text{miss}}$  triggers: Figure 3.8(a) shows the efficiency as a function of *modified*<sup>7</sup> offline  $E_T^{\text{miss}}$  for three different  $E_T^{\text{miss}}$  trigger algorithms, using early 2016  $pp$  collision data. The events have been selected using single lepton (electron or muon) triggers. The x-axis shows the offline  $E_T^{\text{miss}}$  calculated from the sum of electrons, photons and jets, without the contributions from the muons. Three different  $E_T^{\text{miss}}$  high-level trigger algorithms are shown: HLT\_xe80\_tc\_1cw\_L1XE50 calculates  $E_T^{\text{miss}}$  based on calibrated clusters of calorimeter cells, and has a threshold of 80 GeV. HLT\_xe90\_mht\_L1XE50 calculates  $E_T^{\text{miss}}$  based on reconstructed jets, and it has a threshold of 90 GeV. HLT\_xe100\_L1XE50 calculates  $E_T^{\text{miss}}$  based on calorimeter cells calibrated at the electromagnetic scale, and has a threshold of 100 GeV. All three algorithms are seeded by a Level-1 trigger with a threshold of 50 GeV which is also shown; Figure 3.8(b) shows the combined L1 and HLT efficiency of the missing transverse energy triggers HLT\_xe110\_pufit\_L1XE50 and HLT\_xe110\_mht\_L1XE50 as well as the efficiency of the corresponding L1 trigger (L1\_XE50) are shown as a function of the reconstructed  $E_T^{\text{miss}}$  (modified to count muons as invisible) using  $pp$  collision data collected in 2017. The events shown are taken from data with a  $W \rightarrow \ell\nu$  selection to provide a sample enriched in real  $E_T^{\text{miss}}$ . The HLT  $E_T^{\text{miss}}$  of the *pufit* algorithm is calculated as the negative of the transverse momentum vector sum of all calorimeter topological clusters corrected for pile-up. The pile-up correction is done by grouping the clusters into coarser “towers” which are then marked as pile-up if their  $E_T$  falls below a pile-up-dependent threshold.

---

<sup>7</sup> To calculate the  $E_T^{\text{miss}}$  efficiency, e.g. in events with muons, a muon trigger must be employed, therefore muon contributions are removed.

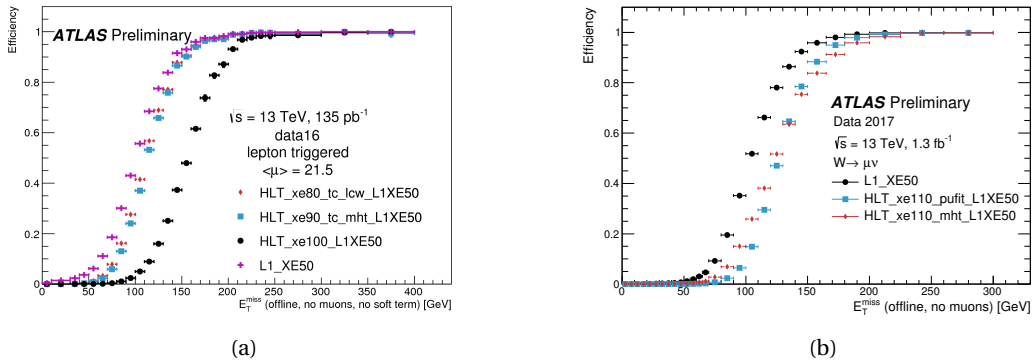


Figure 3.8: Turn-on curves of various  $E_T^{\text{miss}}$  triggers: Figure 3.8(a) shows the efficiency as a function of offline  $E_T^{\text{miss}}$  for three different  $E_T^{\text{miss}}$  trigger algorithms. Three different  $E_T^{\text{miss}}$  high-level trigger algorithms are shown: HLT\_xe80\_tc\_lcw\_L1XE50 calculates  $E_T^{\text{miss}}$  based on calibrated clusters of calorimeter cells, and has a nominal threshold of 80 GeV. HLT\_xe90\_mht\_L1XE50 calculates  $E_T^{\text{miss}}$  based on reconstructed jets, and has a nominal threshold of 90 GeV. HLT\_xe100\_L1XE50 calculates  $E_T^{\text{miss}}$  based on calorimeter cells calibrated at the electromagnetic scale, and has a nominal threshold (at the electromagnetic scale) of 100 GeV. All three algorithms are seeded by a Level-1 trigger algorithm with a nominal threshold of 50 GeV which is also shown; Figure 3.8(b) shows missing transverse energy trigger efficiencies for HLT\_xe110\_pufit\_L1XE50 and HLT\_xe110\_mht\_L1XE50 and for the corresponding L1 seed (L1\_XE50). (from [56]).

# EVENT SIMULATION AND OBJECT RECONSTRUCTION

# 4

*Nature isn't classical, dammit, and if you want to make a simulation of nature, you'd better make it quantum mechanical, and by golly it's a wonderful problem, because it doesn't look so easy.*

Richard P. Feynman

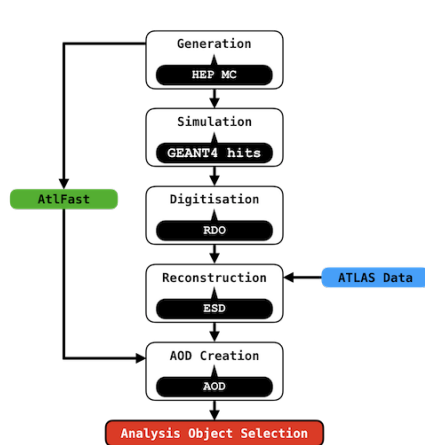


Figure 4.1: The different stages of the work flow needed to produce analysable simulated and collected data outputs. The white boxes represent the processes, and their outputs are shown in black balloons: **RDO**, **ESD**, and the final product, **AOD**. The green ‘AtFast’ box represents the alternative simulation method ATLFAST [57], discussed in Section 4.1. Finally, the blue box shows the stage at which the actual **ATLAS** data events begin processing.

generation (Section 4.1); reconstruction of physics objects<sup>1</sup> in both real data and simulated **MC**

<sup>1</sup> A set of criteria needs to be applied in order to reconstruct the detected object as an “electron”, “photon”, “muon”,

The **ATLAS** software framework Athena [58], which is based on the Gaudi [59] framework developed by the **LHCb** collaboration [34], is used to reconstruct physics objects to be used by analysers, as the data collected and recorded by the **ATLAS** detector requires processing. The Athena framework is capable of dealing with various aspects of the experiment software, e.g. triggering or the processing of simulated data. Custom software, in particular Monte Carlo (**MC**) simulations, is used to simulate physics events used to model background and signal processes. These are produced through different stages, as shown in Figure 4.1, the last of which produces an analyser-friendly output.

In this chapter the stages will be briefly explained as it follows: event gen-

events (Section 4.2).

## 4.1 Generation of an MC-simulated event

MC event generators [60] are extensively used in particle physics to simulate physics processes. A combination of perturbative and phenomenological calculations is employed, to produce randomly distributed physics events of a given type, with stable final state particles. As already mentioned in Chapter 2, the ATLAS detector collects  $pp$ - and heavy-ion-collision data. When two protons collide at such high energy in the centre of mass, the collision essentially occurs between the constituent partons<sup>2</sup>. Three valence quarks (uud), the gluons mediating the strong interactions between the valence quarks, and the sea quarks produced in virtual  $q\bar{q}$  pairs due to interacting gluons, are included as partons. Figure 4.2 shows one of these interactions which are known as Deep Inelastic Scattering (DIS) processes: the substructure of the proton is probed (therefore *deep*), by an incoming particle, in this case a proton, and the particles in the final states are in general different from the initial ones (therefore *inelastic*).

An important, yet simplifying, dimensionless physical quantity is the Bjorken scaling [63], which represents the fraction ( $x$ ) of the proton momentum carried by an interacting parton. The measure of momentum transfer  $Q^2$  in such events, is related to the momentum transferred by the exchanged boson  $q$  by  $Q^2 = -q^2$ . Parton Distribution Functions (PDFs) are used to describe mathematically the parton content of the colliding protons in order to model their interaction.

The  $pp$  scattering at the LHC can be categorised in processes such as *hard*, which can be described with perturbation theory, or *soft*, which involve non-perturbative QCD effects. Typically, a  $pp$  collision involves a hard scattering process between two partons, one for each proton, and a certain number of soft processes, such as Initial State Radiation (ISR), Final State Radiation (FSR), and Underlying Event (UE). The ISR involves particles, that are radiated by partons, which will interact in the hard process prior to their scattering. Those partons, which are not involved in the hard scattering process, the so-called *spec-*

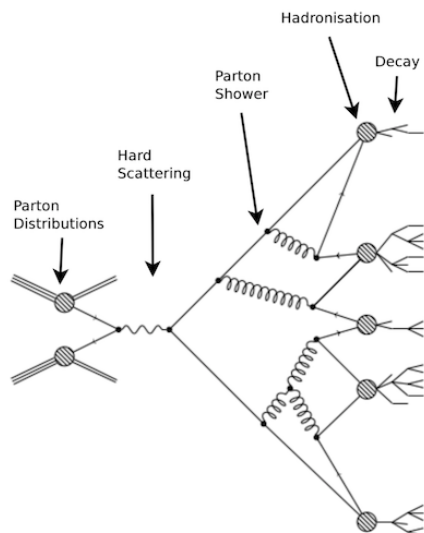


Figure 4.2: Example of a  $pp$  DIS event.

“jet”, etc.

<sup>2</sup> “Feynman [61] interpreted the Bjorken scaling as the point-like nature of the nucleon’s constituents when they were incoherently scattered by the incident electron. Feynman named the point-like constituents partons. This is the parton model.”(taken from [62])

tators, form the **UE**. The **FSR** refers to particles that are radiated from the final state products of the hard scattering. Furthermore, *parton showering* is a process in which particles in the event that have colour can radiate gluons and/or produce  $q\bar{q}$  pairs. Products of these showers will undergo the process of *hadronisation* during which colourless hadron states are produced if  $Q^2$  is of the order of 1 GeV. Such a process occurs due to confinement.

In order to allow analysers to select samples with relevant processes, **MC** samples are divided in categories depending upon the hard-process specified before generation. It is also possible to filter events to only produce a given final state, e. g. asking for zero leptons, in order not to waste computational resources on events which would not pass any selection criteria, regardless, improving the available statistics. The effect of the selection will be taken into account by applying filter efficiency when the analysis is carried out. The HEPMC format is used to store the output of simulated data outputs [64].

## Parton Distribution Function

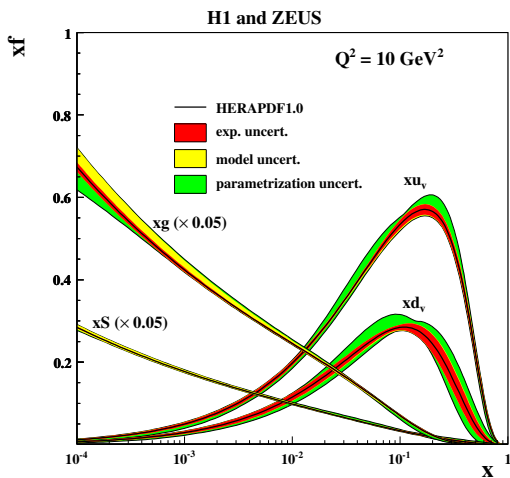


Figure 4.3: PDF from HERAPDF1.0, for up and down valence quarks  $xu_v$  and  $xd_v$ , gluons  $xg$ , and sea quarks  $xS = 2x(\bar{U} + \bar{D})$ , using a momentum transfer of  $Q^2 = 10 \text{ GeV}^2$  (from [65]).

for up and down valence quarks, gluons, and sea-quarks.

PDFs [66] mathematically describe the probability density of constituent partons of the interacting protons to have a fraction,  $x$ , of the nucleon momentum. They depend upon the parton type such as, valence quark, gluon, or sea quark, and the momentum transfer  $Q^2$ . Although perturbative calculations of the PDFs are not feasible, the DGLAP [67, 68] evolution equations, using a range of hard scattering data from both fixed target and collider experiments, can be used to estimate the dependence as a function of  $Q^2$  for a given parton. In other words, PDFs describe the evolution of the structure functions of quarks and gluons as a function of the running<sup>3</sup> strong coupling constant  $\alpha_s$ . Figure 4.3 shows the PDFs, calculated with input from HERA and CTEQ at  $Q^2 = 10 \text{ GeV}^2$

## Matrix Element

The Matrix Element (**ME**) is a simulation stage used to compute the hard processes, where a large momentum transfer ( $Q^2 > \mathcal{O}(1 \text{ GeV})$ ) is involved, which can be calculated using quantum field theory techniques. In order to calculate a probabilistic distribution of the outgoing par-

<sup>3</sup> Referred to a dependence on  $Q^2$

tons, **MEs** to Leading Order (**LO**) or Next-to-Leading Order (**NLO**) in an expansion in  $\alpha_s$ , are used to make **PDFs** simulate partons coming into the hard scatter process. Hard emissions, namely the production of high momentum quarks and gluons in the event can be added into the **ME**; e. g. processes such as a gluon splitting into two gluons,  $g \rightarrow gg$ , or a gluon decaying to a quark-antiquark pair  $g \rightarrow q\bar{q}$ , and a quark radiating a gluon ( $q \rightarrow gq$ ).

## Parton Showers

Due to its non-perturbative nature, the emission of extra soft objects cannot be modelled with the **ME**. Parton Shower (**PS**) generators are instead used to include processes such as the emission of a gluon by a quark ( $q \rightarrow qg$ ), or the emission of  $q\bar{q}$  pairs  $g \rightarrow qq$  or a gluon pair by a gluon  $g \rightarrow gg$ . HERWIG [69], PYTHIA [70], and SHERPA [71] collaborations have developed the most used **PS** models across the ATLAS community and beyond. Markov chains [72] are the heart of the algorithms used to simulate **PS**. These use probabilities that a gluon is radiated or a  $q\bar{q}$  pair is produced.

At intermediate  $Q^2$ , gluon/quark radiation may be treated as a hard emission or part of the **PS**, meaning that, in a given event double-counting might occur. To overcome such issue, the Catani-Krauss-Kuhn-Webber (**CKKW**) [73] and the Michelangelo L. Mangano (**MLM**) [74] schemes are employed to determine whether the emissions are part of the **ME** or **PS**. As the energy of the partons decrease below 1 GeV they will undergo hadronisation.

## Hadronisation

As previously mentioned in Section 1.1, once the quarks and gluons in the final state reach a  $Q^2$  of the order of  $\Lambda_{\text{QCD}} \sim 200$  MeV, the recombination into colourless objects must occur. The modelling of the production of such bound state, the hadronisation, involves non-perturbative **QCD** and many more parameters than the parton showering. Phenomenological models, tuned using data, are then needed. The cluster model [75], used by HERWIG, and the Lund string model [76], used by PYTHIA, are the most employed.

## Underlying Event

Partons not involved in the hard process of the event, referred to as the **UE** [77], can lead to a certain number of soft interactions at a lower energy scale, therefore producing additional hadronic activity in the event. Once again, phenomenological models are used to account for such effect which is modelled within SHERPA and PYTHIA where a whole lot of additional free tuned-to-data parameters are included. More details can be found in [77].

## Detector simulation

Although at this stage the output of the **MC** generators contains all the kinematic features of the event, it is not yet possible to compare simulated events to the **ATLAS** collected data, as the interactions of the particles passing through the detectors are not yet included. The GEANT4 software [78], included within the **ATLAS** offline software<sup>4</sup>, is used to simulate the energy deposited within the detector: in a first stage, the interactions of the particles with the various sub-systems is simulated; following this, a second stage converts energy deposits into detector-output-like signals (voltage, times, etc.). This is the so-called *digitisation*. The output is now produced with a format that is identical to the one produced by the **ATLAS TDAQ** system, therefore **MC** and collected **ATLAS** data can now be consistently processed by the same trigger and reconstruction software. In addition, the **ATLAS** Collaboration also uses fast simulation software such as ATLFAST-II (AF2) [57], where, in order to reduce the usage of the available computational resources, a parametrised description of the showers in the calorimeters is implemented.

## 4.2 Object Reconstruction

Once **MC** samples are digitised, the signals have to be turned into tracks and calorimeter deposits which, in turn, have to be processed to be reconstructed into physics object: electrons, photons, muons, jets, taus, and missing energy,  $E_T^{\text{miss}}$ . Initially, a set of loose definitions is employed in order for various analyses to use such objects. Later, a set of tighter cuts can be applied depending on what a particular analysis needs to focus on. This approach increases the purity of the selected objects at the expense of selection efficiency. The criteria used to define the physics objects, relevant to the analysis presented in this thesis, will be presented in the following paragraphs.

### Tracks and vertices

When a charged particle passes through the detector, all the **ID** sub-systems (pixel, **SCT** and **TRT** components), register “hits” and then, tracing the particle’s trajectory, the hits are reconstructed into a “track”. The most used algorithm is the so-called *inside-out* method: it works outwards from the centre of the **ID** to produce a track once it has initially grouped together hits in the pixel and **SCT** sub-systems. If this track is then compatible with hits in the **TRT** detector, then these hits are also included and the track is accepted. On the contrary, the *back-tracking* algorithm tries to reconstruct a track starting from the **TRT** to the **SCT** and Pixel detectors. Tracks can also be reconstructed using only the hits in the **TRT**. A number of selection cuts are applied to the tracks in order to achieve the required quality. Signals produced in other parts of the detector are then used to match **ID** tracks up with charged-particle candidates, e. g. **ECAL** cluster for an electron track. The  $\eta$  and  $\phi$  values are then assigned to tracks using their

---

<sup>4</sup> All the software made available for analysers to be used after the data have been collected

direction with respect to the origin<sup>5</sup> in the co-ordinate system described in Section 2.2. The relation that links the  $p_T$  of a track to its bending radius and the magnetic field is  $p_T = 0.3 \times B \times R$ , where the  $p_T$  is given in GeV, the magnetic field  $B$  in Tesla, and the radius  $R$  in meters. Moreover a set of variable is defined:

- $d_0$  : the distance of closest approach between the track and the origin
- $z_0$  : the  $z$ -plane component of  $d_0$ ;
- $z_0 \sin \theta$  : the projection of  $d_0$  onto the  $z$ -axis

Vertex reconstruction is needed for various purposes e. g. to differentiate objects produced in the hard scattering from other pile-up<sup>6</sup> interactions. As the bunch length is finite,  $pp$  interactions are spread out along the  $z$  coordinate. In order to reconstruct the PV<sup>7</sup>, tracks are back-tracked to the beam line. Table 4.1 shows a set of cuts applied to the reconstructed ID tracks to be used for vertex reconstruction.

Table 4.1: Cuts applied to the tracks

Variable	Cut
$p_T$	$> 400$ MeV
$ \eta $	$< 2.5$
# IBL hits + B Layer hits	$\geq 1$
# shared modules <sup>8</sup>	$\leq 1$
# Pixel holes <sup>9</sup>	$= 0$
# SCT holes	$\leq 1$
# Si <sup>10</sup> hits	$\geq 9$ if $ \eta  \leq 1.65$ $\geq 11$ if $ \eta  > 1.65$

A global maximum in the  $z$  coordinate of reconstructed tracks is searched for first, to find a vertex seed. The vertex position is then fitted using an algorithm called the *Adaptive Vertex Fitting* algorithm [79, 80]. The vertex position is determined by fitting to ID tracks with the least squares fitting method. Outlier tracks<sup>11</sup> are assigned lower weights in the fit than tracks close to the vertex centre. The adaptive fitting algorithm is able to decrease the sensitivity to these tracks by applying a smaller weight. As we do not know a priori the true position of the vertex centre, and which tracks are outliers, the algorithm iteratively tries to fit the vertex: all tracks weights are initialised with high values and after each fit iteration the weight of the outlier tracks is decreased. The algorithm then determines both the vertex centre and which tracks are outliers with increasing accuracy after each iteration. Finally, the algorithm will stop once

<sup>5</sup> This is assumed to be the position of the primary interaction

<sup>6</sup> For every bunch crossing, the average number of interactions  $\langle \mu \rangle$ , usually referred to as *pile-up*, can be computed

<sup>7</sup> The vertex associated to the hard scattering interaction

<sup>8</sup> 1 shared Pixel hit or 2 shared SCT hits

<sup>9</sup> Holes exist when a hit is expected in a layer of sensors given the fitted trajectory of the track but none is found

<sup>10</sup> Silicon refers to IBL, Pixel and SCT

<sup>11</sup> Tracks that are far from the vertex centre

the fitted vertex centre does not change any more. Once a vertex is found, tracks which are incompatible with the found vertex will form a new vertex seed. The vertex reconstruction process will terminate once all the tracks have been clustered into vertices or no additional vertices can be found. Among all the vertices found by the algorithm, the **PV** will be the one with the highest sum of the squared momenta of the associated tracks ( $\sum p_T^2$ ). The remaining primary vertices found by the algorithm, if any, are referred to as pile-up vertices. Further detail about the algorithm can be found in references [79, 80].

Secondary vertices (**SVs**) can also be reconstructed by looking at the displacement, with respect to the primary vertex position, due to the distance travelled by a decaying particle whose lifetime is sufficiently long for the decay length e.g. b-quarks, which travel a few millimetres.

## Electrons and Photons

Clusters of energy deposits in the electromagnetic calorimeter are used to reconstruct both electron and photon. The **ECAL** is divided into a grid of towers, each of which measuring  $\Delta\eta \times \Delta\phi = 0.025 \times 0.025$ . The total tower energy is calculated summing the energy from all longitudinal layers inside each tower. A sliding-window algorithm groups energy towers into electromagnetic (**EM**) clusters [81, 82]. The window width is  $3 \times 7$  towers in the barrel and  $5 \times 5$  towers in the endcap. The reconstructed cluster therefore has a size of  $\Delta\eta \times \Delta\phi = 0.075 \times 0.175$  in the barrel and  $0.125 \times 0.125$  in the endcap. In order to achieve better cancellation of systematics when using electrons to measure the photon response, the same window size is employed for electrons and photons [81]. Monte-Carlo-based algorithms and data-driven corrections, derived from  $Z \rightarrow ee$  events, are employed to carry out energy calibration [81]. Figure 4.4 shows an illustration of the electron reconstruction algorithm.

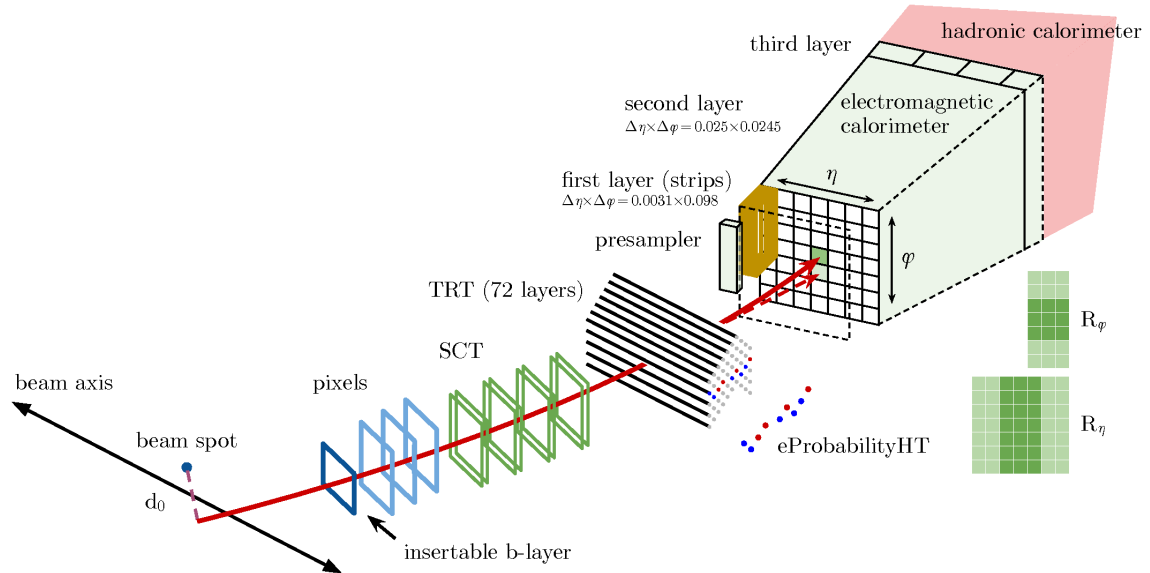


Figure 4.4: Schematic view of the electron reconstruction and identification (taken from [83]).

Identified clusters are then matched to reconstructed **ID** tracks (required to have a minimum number of pixel and silicon hits) using the track and cluster position. A cluster will be

either considered as an electron or a photon candidate, if it satisfies one of the following criteria:

**electron:** one single reconstructed [ID](#) track with an associated vertex;

**unconverted photon:** no [ID](#) tracks;

**converted photon:** two opposite-signed collinear tracks (consistent with electrons) are associated with a secondary vertex;

**converted photon:** single track is present but there are missing hits in the [IBL](#)

Once electrons and photons have been reconstructed an additional set of criteria is employed to rule out any potential misidentification. In particular, the identification is based on a Likelihood ([LH](#)) algorithm that depends on variables such as shower shape, radiation deposited in the [TRT](#), and associated-track properties. Identification Working Points ([WPs](#)), such as Loose, Medium and Tight, are employed to identify electrons using different selections, which will reflect in different efficiencies and purities<sup>12</sup>, as the tighter the identification is, the purer the selected object will be. Figure 4.5 shows the reconstruction and identification efficiencies using 2016 data for electrons, and 2015+2016 for unconverted photons. Here, the data-[MC](#) discrepancy in the electron identification performance is due to a mismodelling of the [TRT](#) conditions in addition to the known mismodelling of calorimeter shower shapes in the GEANT4 detector simulation [84]. Nonetheless, scale factors<sup>13</sup> were derived and applied to the Monte Carlo, to match the performance observed in the data.

The shower shape and the amount of hadronic activity behind the [EM](#) cluster are at the heart of photon identification. The [EM](#) showers originating from photons and those originating from neutral mesons e. g.  $\pi_0$  can be distinguished by looking at the energy deposited in the cells within the first and second layer of the [ECAL](#) [86]. Two categories of photons are reconstructed employing two identification [WPs](#): Loose and Tight. The former are typically used for triggering, the latter for physics analysis, such as the one presented in Chapter 5, where, the top-quark pair production in association with a photon,  $t\bar{t}+\gamma$  was studied.

## Muons

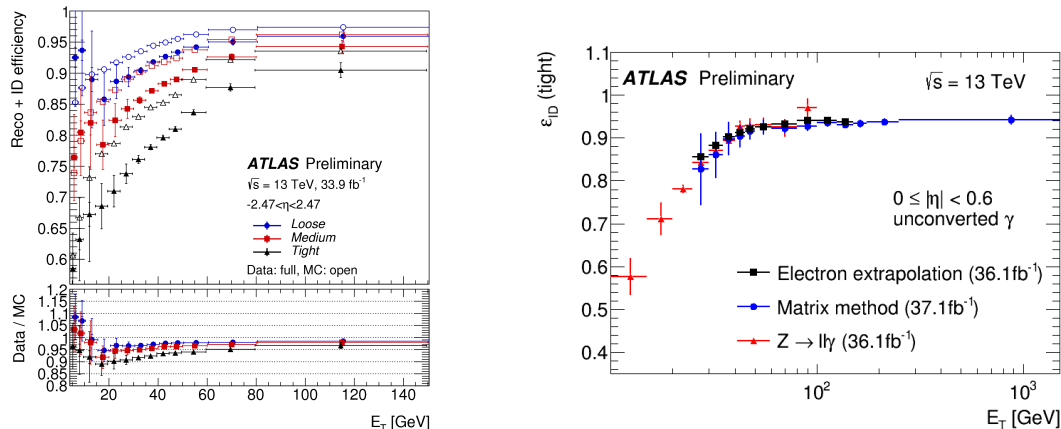
Two independent track fits in the [ID](#) and [MS](#) are the basis of the muons selection procedure. Depending on the signature in each sub-system the fits are combined using different algorithms. Various categories of muons can be reconstructed with the [ATLAS](#) detector [87] and they can be listed as it follows:

**Combined:** candidates whose tracks are found in both [ID](#) and [MS](#) on which a global refit is run to obtain a combined muon track that describes the trajectory of the particle through the whole detector, in order to take into account the energy loss in the calorimeter;

---

<sup>12</sup>The number of actual electrons (photons) among the selected candidates.

<sup>13</sup>Calibration factors derived from data.



(a) Electron reconstruction and identification efficiencies in  $Z \rightarrow ee$  events as a function of  $E_T$ , integrated over the full pseudo-rapidity range. The data efficiencies are obtained by applying data/MC efficiency ratios that were measured in  $J/\psi \rightarrow e^+e^-$  and  $Z \rightarrow ee$  events to MC simulation. The total statistical and systematic uncertainty is shown.

(b) Photon identification efficiencies using the full 2015 + 2016 dataset. Comparison of the data-driven measurements (radiative  $Z$  decay, electron extrapolation and matrix method [85]) of the identification efficiency for unconverted photons as a function of  $E_T$  in the region  $10 \text{ GeV} < E_T < 1500 \text{ GeV}$  for the pseudo-rapidity interval  $|\eta| < 0.6$ . The error bars represent the sum in quadrature of the statistical and systematic uncertainties estimated in each method.

Figure 4.5: Electron and photon reconstruction and identification efficiencies (taken from [84]).

**Extrapolated:** candidates in the forward region ( $2.5 < |\eta| < 2.7$ ) that produced a track in the **MS** but fell outside the **ID** acceptance, therefore their trajectory is reconstructed using the **MS** track, loosening its compatibility requirement with the interaction point;

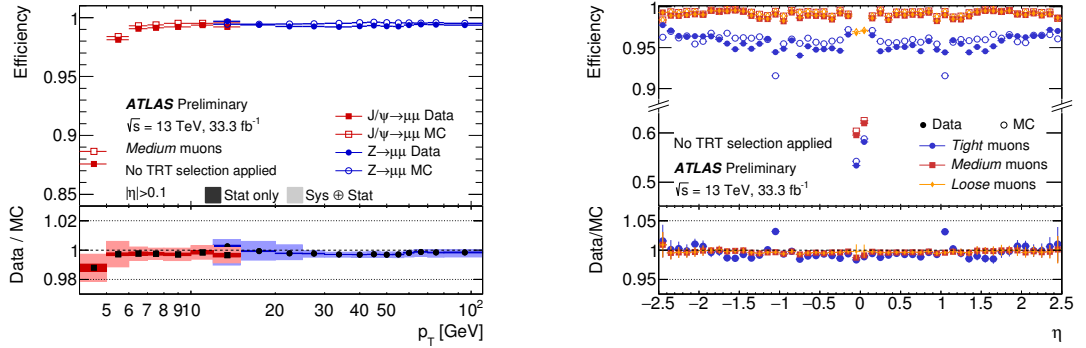
**Segment tagged:** candidates whose tracks in the **ID** are found to have a corresponding hit in the inner layer of the **MS**. Generally for muons with low  $p_T$  or due to cracks in the **MS**;

**Calorimeter tagged:** candidates, whose **ID** tracks can be matched with an energy deposit in the calorimeter, compatible with the signature of a Minimum Ionising Particle (**MIP**), with no associated **MS** tracks; mainly muons in the central pseudo-rapidity region ( $|\eta| < 0.1$ ) due to a crack in the barrel of the **MS**;

In order to separate prompt muons from backgrounds such as pions and kaons decays, further identification requirements are employed, e. g. track quality requirements in the **ID** and the **MS**, normalised  $\chi^2$  of the combined track fit, etc.).

Figure 4.6 shows reconstruction and identification efficiencies as a function of  $p_T$  and  $\eta$ . Likewise electrons and photons, in order to meet all the different requirements of the various ATLAS analyses, a set of **WPs** is defined. The performance is calibrated using the so-called tag-and-probe method<sup>14</sup> in  $Z \rightarrow \mu\mu$  or  $J/\psi \rightarrow \mu\mu$  events. Further details can be found at [87].

<sup>14</sup> Method used to select, from known resonances such as  $Z \rightarrow ee$  unbiased samples of electrons (probes) by using strict selection requirements on the second object produced from the particle's decay (tags) [89].



(a) Muon reconstruction efficiencies for the Medium identification algorithm measured in  $J/\psi \rightarrow \mu\mu$  and  $Z \rightarrow \mu\mu$  events as a function of the muon  $p_T$ . The prediction by the detector simulation is depicted as empty circles (squares), while the full circles (squares) indicate the observation in collision data for  $J/\psi \rightarrow \mu\mu$  ( $Z \rightarrow \mu\mu$ ) events. Only statistical errors are shown in the top panel. The bottom panel reports the efficiency scale factors. The darker error bands indicate the statistical uncertainty, while the lighter bands indicate the quadratic sum of statistical and systematic uncertainties.

(b) Muon reconstruction efficiencies for the Loose/Medium/Tight identification algorithms measured in  $Z \rightarrow \mu\mu$  events as a function of the muon  $\eta$  for muons with  $p_T > 10 \text{ GeV}$ . The prediction by the detector simulation is depicted as open circles, while filled dots indicate the observation in collision data with statistical errors. The bottom panel shows the ratio between expected and observed efficiencies, the efficiency scale factor. The errors in the bottom panel show the quadratic sum of statistical and systematic uncertainty.

Figure 4.6: Muon reconstruction and identification efficiencies (taken from [88]).

## Jets

As already mentioned in Sections 1.1 and 4.1, due to QCD confinement when a  $pp$  collision occurs, a spray of hadronic matter, or *jet*, is produced. A jet in the ATLAS detector looks like an object that released its energy in both ECAL and HCAL via EM and hadronic showers and, as it is generally comprised of a certain number of charged particles, it also has ID tracks associated with the showers. The identification and the reconstruction of jets is important for the analysis discussed in Chapter 5, which targets the  $pp \rightarrow t\bar{t} \rightarrow bqq\tilde{\chi}_1^0 + \bar{b}\bar{q}\tilde{\chi}_1^0$  channel where all the visible decay products are quarks, therefore jets. A brief description of jet reconstruction and calibration is presented in the following paragraphs.

The three-dimensional structure of topological clusters in the calorimeters is used to measure the energy deposited by the showers through the clusters[90, 91]. These are built up via an iterative algorithm which first forms the core of the cluster by identifying seed cells, with a high energy threshold, and adding adjacent cells with a lower threshold, and then, in order to account any potential shower leak an extra layer of cells is added, such that a collection of topological clusters per event is obtained. Jet-finding algorithms, which treat jets as massless objects, are then fed with such clusters information such as energy and position. The former is calculated as the sum of all the energy deposits in the cells previously identified, whose position within the detector is used to deduct angular information. A widely used algorithm within the ATLAS Collaboration is the anti- $k_t$  one which forms a collection of jets as output by iteratively recombining the input clusters. The algorithm essentially groups two object into a single

one according to a distance  $d_{ij}$ , defined as:

$$d_{ij} = \min\left(k_{t_i}^{2p}, k_{t_j}^{2p}\right) \frac{\Delta_{ij}^2}{R^2} \quad (4.1)$$

where  $i$  and  $j$  are topological cluster indices,  $k_t$  is the transverse momentum of each topological cluster,  $\Delta_{ij}^2 = \Delta\phi_{ij}^2 + \Delta\eta_{ij}^2$  is the distance between the two topological clusters, and  $R$  is an input parameter into the algorithm which, in the analysis presented in this work, is set to  $R = 0.4$ . The topological clusters  $i$  and  $j$  which minimise  $d_{ij}$  are then combined to form larger individual clusters. The next iteration takes into account the larger individual clusters as well as the remaining initial topological clusters and combines them according to the same procedure, which is repeated until all remaining topological-cluster pairs satisfy  $\Delta_{ij} > R$ . Additional information can be found at [92].

Due to the compensation condition<sup>15</sup> the hadronic component of the shower produced by jets is underestimated and for such reason a calibration procedure is employed. In particular, the so-called Electromagnetic + Jet Energy Scale scheme is employed [93] where a set of corrections is applied to match the energy of the initial partons. These are:

**vertex correction:** once the anti- $k_t$  algorithm has reconstructed the jets, its four-vectors, initially pointing at the centre of the detector, are adjusted to point to the primary vertex;

**pile-up correction:** pile-up effect on the jets energy is reduced by using an area-based subtraction procedure [94];

**jet energy and  $\eta$  correction:** additional calibration based on energy and pseudo-rapidity corrections where the kinematical properties of the reconstructed jet ( $p_T$  and  $\eta$ ) are compared to the ones derived from MC simulations;

**global sequential correction:** individual jet property-based correction for properties such as the fraction of energy deposited in different calorimeter layers or the number and type of associated tracks [95];

**in-situ corrections:** then measured  $p_T$  of the jet is corrected using multi-jet and  $\gamma/Z+jets$  events, where the momentum of a *probe* jet is balanced against a well-measured reference object [96].

Finally, the Jet vertex Tagger (JVT) variable [97], related to the fraction of charged tracks within the jets that point to the primary vertex, is employed. This observable tests the compatibility between the reconstructed jet and the hard-scatter charged particles within the jet [98].

### b-tagged jets

---

<sup>15</sup>Calorimeters response can be described in terms of the EM/Hadronic ratio, as it is a measure of the calorimeter response to EM VS hadronic radiation. An ideal calorimeter would have EM/Hadronic~1.

The identification and the reconstruction of jets originated from  $b$ -quarks is also important, as they also are part of the final state of the analysis presented in this work. The standard jet-reconstruction procedure discussed above applies to  $b$ -jets too, with the addition of dedicated algorithms ( $b$ -tagging [100]) employed to spot a  $b$ -hadron within their cone. A diagram, showing the difference between light jets and  $b$ -jets is shown in Figure 4.7. Due to their lifetime ( $\sim 10^{-12}$  s),  $b$ -hadrons can travel a measurable distance in the detector before decaying ( $\sim 1$  mm for a 20-GeV  $b$ -jet), therefore producing a **SV** which, together with a requirement on the impact parameter  $d_0$ , already provides a useful discrimination tool for jet flavour. Unfortunately,  $c$ -jets also leave a similar signature within the ATLAS detector. Although on average they travel a shorter distance due to their shorter lifetime [101], their presence introduces a source of background for  $b$ -tagging.

Algorithms for  $b$ -tagging, such as, *I2PD* and *I3PD* [102]<sup>16</sup>, *Secondary Vertex Finding* [103], and *Decay Chain Multi-Vertex Algorithm (JetFitter)* [104], are widely employed within the ATLAS Collaboration. Their outputs are combined to feed a single multivariate tagger, Multivariate algorithm (**MV2**), which is used by many analyses as it is, as of today, the algorithm with the highest discriminating power for jet flavour tagging. In particular, **MV2** is a Boosted Decisions Tree (**BDT**) algorithm [105] implemented within the ROOT TMVA [106, 107] and is provided in three different versions: MV2c00, MV2c10, and MV2c20. MV2c00 denotes the MV2 algorithm where no  $c$ -jet contribution was present in the training. MV2c10 (MV2c20) denote the MV2 outputs where a 7% (15%)  $c$ -jet fractions was present in the background sample [100]. Such tagger was used for both the analyses presented in this thesis.

Figure 4.8 shows the performances of different configuration of such tagger. In particular, the  $b$ -tagging efficiency is compared to the  $c$ -jets and light-jet rejection which can be defined as the inverse of the mis-tag rates. Furthermore, the more  $c$ -jet there are in the background training sample the better the rejection will be, as opposite to the case where no  $c$ -jets are included.

### Missing Transverse Energy, $E_T^{\text{miss}}$

As previously mentioned, particles like neutrinos or potential DM candidates escape the ATLAS detector. When these particles are produced a momentum imbalance in the transverse plane

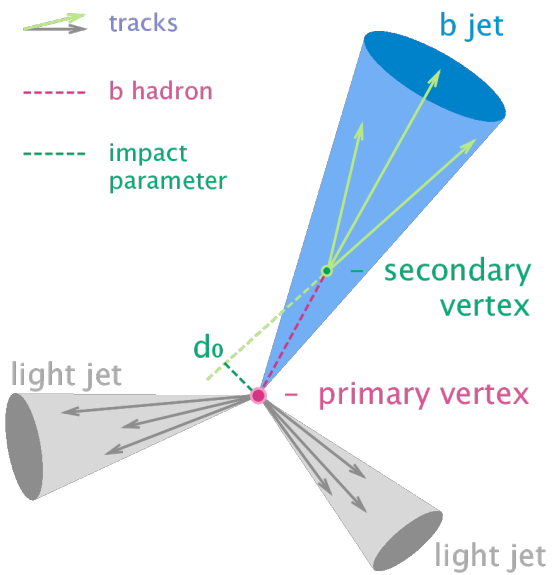


Figure 4.7: Diagram showing the common principle of identification of jets initiated by  $b$ -quark decays [99].

<sup>16</sup>The significance of the transverse impact parameter (IP) of the tracks,  $d_0/\sigma_{d_0}$  is used by both algorithms

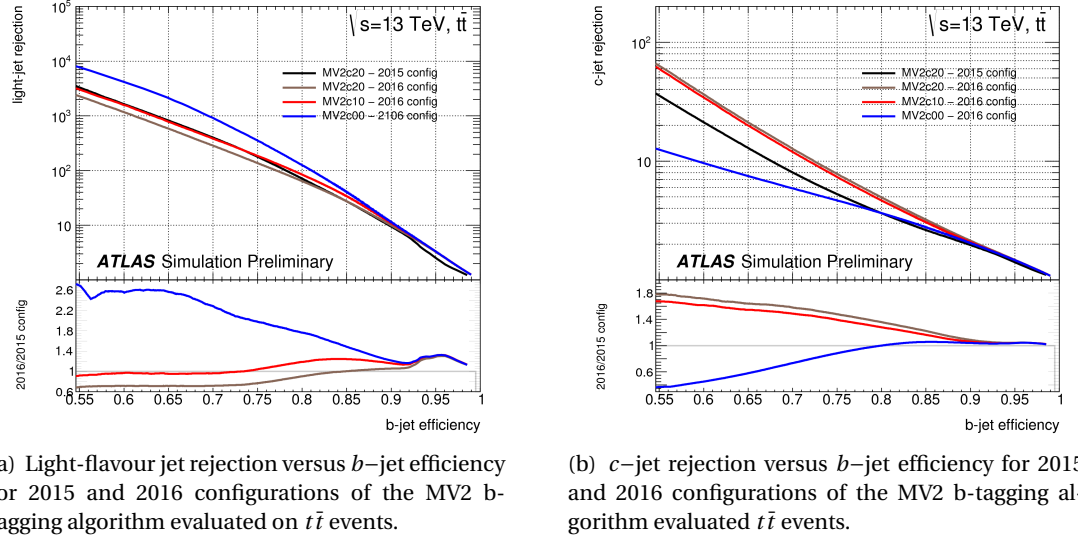


Figure 4.8: Performance of the MV2 tagger in  $t\bar{t}$  events. Various fractions of  $c$ -jets in the background training sample were considered (taken from [108]).

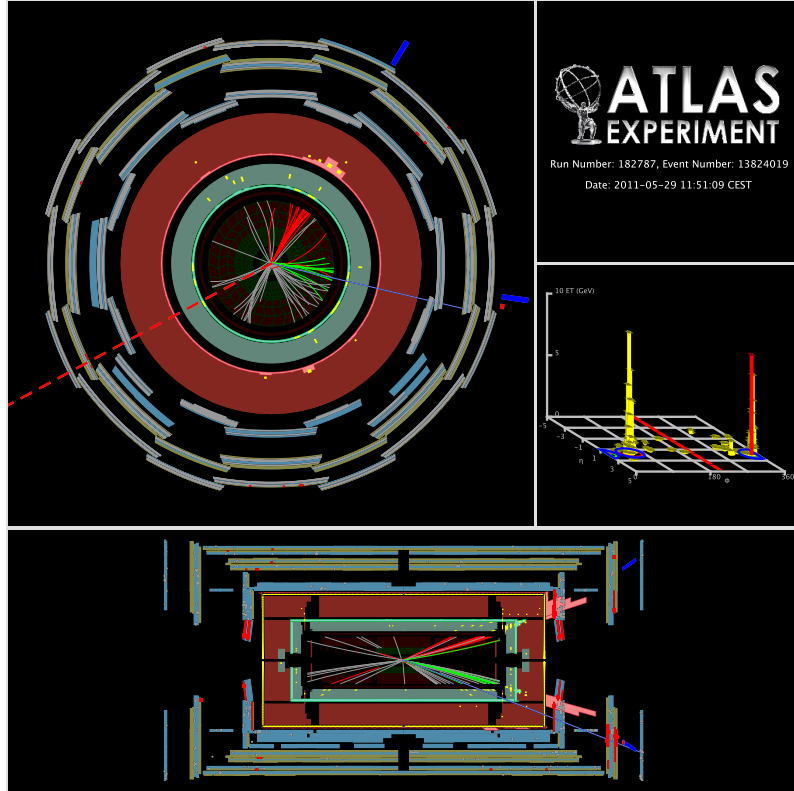


Figure 4.9: ATLAS Event display for an event that has jets (blue solid lines) and  $E_T^{\text{miss}}$  (red dashed line) (taken from [109]).

will characterise the event, as shown in Figure 4.9. Such quantity can be estimated using the four-momenta of all the visible detected objects in the event, and it is called missing transverse momentum,  $\mathbf{p}_T^{\text{miss}}$  [110]. The  $\mathbf{p}_T^{\text{miss}}$  provides an estimate of the total momentum of the particles

that escaped the [ATLAS](#) detector and it is defined as it follows:

$$\mathbf{p}_T^{\text{miss}} = - \sum_i \mathbf{p}_T^{i,\text{obj}} \quad (4.2)$$

Here,  $\mathbf{p}_T^{i,\text{obj}_i}$  represents the transverse momentum of the  $i$ -th visible object in the event. The Missing Transverse Energy  $E_T^{\text{miss}}$ , is therefore defined as the magnitude of  $\mathbf{p}_T^{\text{miss}}$ .

The  $E_T^{\text{miss}}$  is reconstructed by selecting calibrated hard objects to measure the missing transverse momentum in the event. In particular the  $(x - y)$  components of the  $E_T^{\text{miss}}$  are calculated as it follows:

$$E_{x(y)}^{\text{miss}} = E_{x(y)}^{\text{miss},e} + E_{x(y)}^{\text{miss},\mu} + E_{x(y)}^{\text{miss},\tau} + E_{x(y)}^{\text{miss,jets}} + E_{x(y)}^{\text{miss},\gamma} + E_{x(y)}^{\text{miss,soft}} \quad (4.3)$$

where each object term is given by the negative vectorial sum of the momenta of the respective calibrated objects. In the analyses presented in this work, terms containing  $\tau$  leptons were not considered as  $\tau$  reconstruction was never explicitly performed. The *soft term* is reconstructed from detector signal objects not associated with any object passing the selection cuts, e. g. [ID](#) tracks (track-based soft term) or calorimeter signals (calorimeter-based soft term). From the components in Equation 4.3 the magnitude of  $E_T^{\text{miss}}$  and the azimuthal angle  $\phi^{\text{miss}}$  are calculated as it follows:

$$E_T^{\text{miss}} = \sqrt{\left(E_x^{\text{miss}}\right)^2 + \left(E_y^{\text{miss}}\right)^2} \quad ; \quad \phi^{\text{miss}} = \arctan\left(\frac{E_y^{\text{miss}}}{E_x^{\text{miss}}}\right) \quad (4.4)$$

The  $E_T^{\text{miss}}$  performance is studied in two complementary topologies, with and without genuine  $E_T^{\text{miss}}$ , such as  $W \rightarrow ev$  and  $Z \rightarrow \mu\mu$ , in both data and [MC](#) in order to test the reconstruction algorithms and correct for any potential biases.

# SEARCH FOR TOP SQUARKS IN ALL-HADRONIC FINAL STATES

5

*In God we trust. All others must  
bring data.*

---

William E. Deming

In this chapter the core of this thesis will be presented, namely the search for the direct pair-production of the supersymmetric partner of the top quark in all-hadronic final states using a dataset of  $36.1\text{ fb}^{-1}$   $pp$  collisions, at a centre-of-mass energy  $\sqrt{s} = 13\text{ TeV}$ , delivered by the [LHC](#) and collected by the [ATLAS](#) detector.

The results produced were published in a paper in the [Journal of High Energy Physics](#) in September 2017 [111]. A previous version of the analysis was also made public, using  $13.3\text{ fb}^{-1}$  collected at  $\sqrt{s} = 13\text{ TeV}$ , with an earlier subset of the whole 2015+2016 dataset, documented in an [ATLAS](#) conference note [112]. Although both versions contain author's contributions, only the results of the most recent analysis will be hereby discussed, as it represents the most updated, improved and extended version. Specifically, the optimisation of the search strategy, as well as the data-driven estimation of the number of events in the search regions for one of the most important backgrounds, and the evaluation of the related theory uncertainties, characterised the author's contributions. In addition, exception made for the optimisation strategy, the same contributions were also used in a different [SUSY](#) analysis published in October 2017 in [113]. Further details can be found in Appendix A.

The chapter will be structured as it follows: an excursus on the simplified [SUSY](#) models considered will be presented in Section 5.1; the objects used in both data and [MC](#) will be discussed in Section 5.2; the selection of the events, together with the key variables used and the optimisation of the regions in which the [SUSY](#) signals were searched for will be presented in Section 5.3; the nominal procedure used for the background estimation will be discussed in Section 5.6, with particular focus on the data-driven background estimation in Section 5.7; the results, together with their interpretation, will finally be presented in Section 5.8.

## 5.1 SUSY Signals

As already introduced in Section 1.2.2, the signals considered in this work are generated using simplified models, meaning that only the  $\tilde{t}$ , the  $\tilde{\chi}_1^0$ , the  $\tilde{\chi}_2^0$ , and the  $\tilde{\chi}_1^\pm$ , were the **SUSY** particles considered. In particular, in such considered models, either  $\tilde{\chi}_2^0$  or  $\tilde{\chi}_1^\pm$  is assumed to be the **NLSP** and, the chargino-neutralino mass splitting  $\Delta m(\tilde{\chi}_1^\pm, \tilde{\chi}_1^0)$  is assumed to be 1 GeV, in accordance with the naturalness argument. This implies that the  $\tilde{\chi}_1^\pm$  will promptly decay to  $W^* \tilde{\chi}_1^0$ , with the  $W$  emitted as a virtual particle. The decay products of the so-created virtual  $W$  will therefore be low  $p_T$  objects which will not be reconstructed by the **ATLAS** detector.

### 5.1.1 Benchmark processes

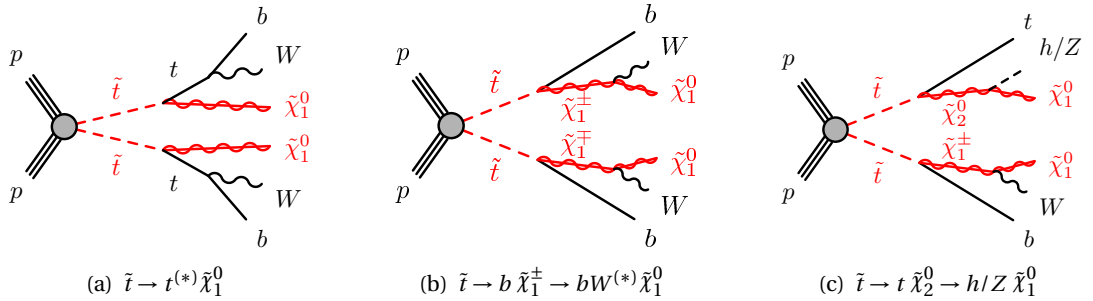


Figure 5.1: Diagrams of the decay topologies of the signal models considered in this work.

Figure 5.1(a)–(c) shows the diagrams corresponding to the decay scenarios considered in this work. In particular, (a) where both top squarks decay<sup>1</sup> via  $\tilde{t} \rightarrow t^{(*)} \tilde{\chi}_1^0$ ; (b) where at least one of the stops decays via  $\tilde{t} \rightarrow b \tilde{\chi}_1^\pm \rightarrow b W^{(*)} \tilde{\chi}_1^0$ ; (c) where  $m_{\tilde{\chi}_2^0}$  is small enough to allow one stop to decay via  $\tilde{t} \rightarrow t \tilde{\chi}_2^0 \rightarrow h/Z \tilde{\chi}_1^0$  where  $h$  is the **SM** Higgs boson;

The results were interpreted in the simplified models where only one- and two-step decays scenarios are allowed and, as already mentioned, the latter will be referred to as a natural **SUSY**-inspired mixed grid, i.e.  $\Delta m(\tilde{\chi}_1^\pm, \tilde{\chi}_1^0) = 1$  GeV [114, 115, 116]. Furthermore, in both scenarios the **LSP** is considered to be a pure bino state. The results will also be interpreted in two slices of the **pMSSM** models: wino-**NLSP** and well-tempered neutralino **pMSSM** [117, 118]. A fourth scenario, in addition to direct pair production, was considered: top squarks can also be indirectly produced via gluino decays, as illustrated in Figure 5.2. In such model, the mass difference between the top squark and the

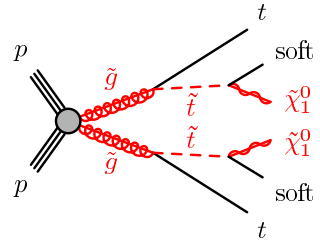


Figure 5.2: Diagram of the gluino-mediated top squark production. The term “soft” refers to decay products whose transverse momenta are below the detector thresholds.

<sup>1</sup> The symbol (\*) indicates off-shell production

neutralino is considered to be relatively small,  $\Delta m(\tilde{t}_1, \tilde{\chi}_1^0) = 5$  GeV, allowing the jets originating from  $\tilde{t}_1$  decay to have a  $p_T$  below the reconstruction threshold of the ATLAS detector resulting in an experimental signature nearly equivalent to the one in Figure 5.1(a).

### 5.1.2 MC samples

A grid of points across the  $(m_{\tilde{t}_1} - m_{\tilde{\chi}_1^0})$  plane with a 50-GeV spacing is generated to simulate the above-mentioned simplified models. The signal models were generated using MG5\_aMC@NLO 2.2-2.4 [119] interfaced to PYTHIA8 [120] for the PS and hadronisation. EvtGen 1.2.0 [121] was employed for the decays of the  $b$ - and  $c$ -hadrons. The tree-level ME calculation includes the emission of up to two additional partons for all signal samples. The NNPDF2.3LO PDF [122] set was used to generate the signal samples with the A14 [123] tune for the UE and shower parameters. Additionally, the CKKW-L prescription [124] was used for the ME-PS matching.

The various signal cross sections were all calculated to next-to-leading order in the strong coupling constant, with the addition of soft-gluon emission re-summation at next-to-leading-logarithm accuracy (NLO+NLL) [125, 126, 127]. The sparticle mass spectra for pMSSM models were calculated using Softsusy 3.7.3 [128, 129] while the decays of each sparticle were performed by HDECAY 3.4 [130] and SDECAY 1.5/1.5a [131]. Finally, various PDF sets, factorisation, and re-normalisation scales were used to generate an envelope of cross-section predictions, within which a nominal value and uncertainty were chosen. Further details can be found in [28].

## 5.2 Objects definition

The physics objects, as output of the reconstruction algorithms discussed in Section 4.2, are required to pass a first loose selection to be categorised as *baseline* objects. An additional procedure is employed, to remove potentially overlapping objects, e.g. a lepton is identified as a jet, or a lepton that falls within the same jet cone. The so-called Overlap Removal (OR) procedure, whose inputs are two baseline objects, is employed to resolve such ambiguity by discarding one of the two objects by looking at their  $\Delta R$  as shown in Table 5.1.

Table 5.1: List of the possible ambiguities with relative criteria and decisions.

Ambiguity	Criterion	Object kept	Object removed
electron/jet	$\Delta R(e, \text{jet}) < 0.2$	electron	jet
	$0.2 \leq \Delta R(e, \text{jet}) < 0.4$	jet	electron
electron/ $b$ -jet	$\Delta R(e, b\text{-jet}) < 0.2$	$b$ -jet	electron
muon/jet	$\Delta R(\mu, \text{jet}) < 0.4$ and $N_{\text{tracks}} < 3, p_T^{\text{track}} > 500$ MeV	muon	jet
photon/electron	$\Delta R(e, \gamma) < 0.4$	electron	photon
photon/muon	$\Delta R(\mu, \gamma) < 0.4$	muon	photon
photon/jet	$\Delta R(\text{jet}, \gamma) < 0.4$	jet	photon

The data-driven estimation of  $t\bar{t}+Z$  events using  $t\bar{t}+\gamma$  is the only part of the analysis that used reconstructed photons. In particular, the **OR** is modified accordingly to avoid that an object will appear in multiple collections (double-counting). The various baseline and signal objects can now be defined as it follows:

**Electrons** baseline electrons are required to have  $|\eta| < 2.47$ ,  $p_T > 7$  GeV and have to pass a variant of the VeryLoose likelihood-based selection (further details in [132, 133]). Electron candidates which pass the **OR**, have a  $p_T > 20$  GeV ( $p_T > 28$  GeV) in regions with a  $E_T^{\text{miss}}$  (lepton) trigger, satisfy  $d_0/\sigma_{d_0} < 5$ ,  $z_0 \sin \theta < 0.5$ , and pass a Tight likelihood-based selection isolation, are tagged as signal;

**Muons** baseline muons have to pass a Loose selection [134], satisfy  $|\eta| < 2.7$  and  $p_T > 6$  GeV. Further requirements are imposed on muon candidates to tag them as signal. In particular, they have to pass the **OR**, a Medium quality selection [134], and satisfy  $|d_0| < 3\sigma_{d_0}$  and  $|z_0 \times \sin \theta| < 0.5$ . Additionally, the  $p_T$  requirement is tightened up to 20 GeV (28 GeV) in regions with a  $E_T^{\text{miss}}$  (lepton) trigger;

**Photons** baseline photons have to pass a Tight [85] selection, and have  $p_T > 25$  GeV and  $|\eta| < 2.37$ . Additionally, baseline photon candidates are required to have  $p_T > 130$  GeV and satisfy a tighter isolation selection, in order to be tagged as signal;

**Jets** as already mentioned in Chapter 4.2, jets are reconstructed using the anti- $k_t$  algorithm with  $R = 0.4$ . Baseline jets are required to have  $p_T > 20$  GeV and  $|\eta| < 4.8$ . Signal jets have to pass the **OR**, satisfy the **JVT** requirement, and have  $|\eta| < 2.8$  and  $p_T > 20$  GeV.

**b-tagged jets** baseline jets in the event are identified as originating from the decay of a  $b$ -quark is based on the MV2c10 jet tagger which uses the a 77% fixed-cut WP. The  $p_T$  threshold applied to signal jets is also applied to  $b$ -jet and the requirement on the pseudorapidity is relaxed down to  $|\eta| < 2.5$ .

**Missing transverse energy** The  $E_T^{\text{miss}}$  is reconstructed as described in Section 4.2. Baseline muons, electrons, and jets after overlap removal are used in the  $E_T^{\text{miss}}$  recalculation.

Additionally, in the analysis carried out during Run-1 [135] another  $E_T^{\text{miss}}$ -related quantity was introduced. The track-based  $E_T^{\text{miss}}$ , derived from the sum of the  $p_T$  of the tracks associated with the objects in the event was found to have discriminating power to reject fake  $E_T^{\text{miss}}$ . The  $\mathbf{p}_T^{\text{miss,track}}$ , whose magnitude is  $E_T^{\text{miss,track}}$ , from the tracking system is computed using the vector sum of the reconstructed inner detector tracks,  $\mathbf{p}_T^{\text{miss,track}} = \sum_i^{\text{tracks}} \mathbf{p}_T^i$ , with  $p_T > 500$  MeV and  $|\eta| < 2.5$ , that are associated with the **PV** in the event.

Ultimately, leptons are also required to satisfy  $p_T$ -dependent track- and calorimeter-based isolation criteria. The calorimeter-based isolation is determined by taking the ratio of the sum of energy deposits in a cone of  $R = 0.2$  around the electron or muon candidate and the energy deposits associated with the electron and muon. The track-based isolation is estimated in a similar way but using a variable cone size with a maximum value of  $R = 0.2$  for electrons and

$R = 0.3$  for muons. An isolation requirement is made that is 95% efficient for electron or muon candidates with  $p_T = 25$  GeV and 99% for candidates with  $p_T = 60$  GeV.

## 5.3 Event Selection

A cut-and-count strategy is at the heart of the analysis here presented. Dedicated sets of discriminating variables are employed to isolate, where possible, the targeted signals from the main SM backgrounds. Equally, background-enriched regions are defined to *control* the modelling of such backgrounds. The number of events passing such selections is used as the main observable, to predict both signal and background processes either by means of MC samples, or using data-driven techniques. In general, a combination of the two is employed.

The ATLAS detector did not operate with the same conditions during 2015 and 2016, meaning that different triggers and objects (calibration parameters) were used. In order for MC parameters to be modified consistently with what is done in data, MC events are assigned a random number, which identifies an ATLAS run. This allows MC events to be associated with specific data-taking periods such that their parameters are associated with what is done in data and can be modified accordingly.

### 5.3.1 Triggers used

As previously discussed in Chapter 2 and 3, physics events are recorded once they passed a certain trigger. In particular, a  $E_T^{\text{miss}}$  trigger is used to select events that fall in signal-enriched regions, Signal Region (SR), where 0 leptons ( $\ell$ ) are required; a single-lepton (photon) trigger is used for background-enriched regions, where 1-lepton (photon) is required. A breakdown of all the lowest unprescaled online triggers used will be presented below;

**Missing transverse energy** once the  $E_T^{\text{miss}}$  is reconstructed from an input jet collection, a 70-GeV threshold is required in the 2015 dataset whereas, due to the increase in instantaneous luminosity (impact on the trigger rate), in 2016 the threshold was gradually raised to 90, 100, and 110 GeV. It can be seen (Figure 3.8) that for analysis purposes a cut of at least 200 GeV is required to stay in a region where the trigger is fully efficient (*plateau*);

**Single electron** events with an electron are triggered on using a logic OR of three chains. In particular, the first consists of a 24-GeV (26-GeV) threshold, together with an L1 isolation, in 2015 (2016) data; the second chain uses a 60-GeV threshold without additional isolation requirement; the third uses a 120-GeV threshold to be efficient at high  $E_T$ ; a  $p_T^e > 27$  GeV cut is applied to stay in the plateau region;

**Single muon** a logic OR of two chains is instead used to trigger events with muons; a first chain with a 20-GeV threshold is used in data 2015 and 26-GeV threshold, together with an isolation requirement, in 2016; a second chain with a 50-GeV threshold is employed for both 2015 and 2016 data; a  $p_T^\mu > 27$  GeV is applied to stay in the plateau region;

**Single photon** unlike the lepton case, only one chain is used to select events with photons; a 120 GeV (140 GeV) threshold is employed in 2015 (2016). Additionally, in order to ensure full trigger efficiency a  $p_T^\gamma > 150$  GeV cut is applied.

### 5.3.2 Event cleaning

In order to remove events where a detector fault occurred, a set of offline cuts is applied. The first requirement for an event to be a good physics event, is the existence of a primary vertex with a minimum of two tracks, with  $p_T > 400$  MeV, associated with it. Once this is passed, the status of both ECAL and HCAL for that event is checked: if any of the calorimeters returned an error state, the event is discarded. In addition, to reduce and suppress the fake-jet contamination a *bad jet* requirement is defined by introducing quality requirements on a variety of jet parameters, e.g. the fraction of energy deposited in the different layers of the calorimeters, and the fraction of jet  $p_T$  measured by the tracks in the Inner Detector. Events containing bad jets that passed the OR are discarded. Similarly, events containing baseline muon candidates, whose relative uncertainty on  $e/p$  is larger than 20%, and which were found before the OR, are discarded. This also applies to events containing those potentially cosmic muons which were not removed by the OR.

## 5.4 Standard Model Backgrounds

As already anticipated in Section 1.1.2, there exists a wide variety of SM processes whose cross sections are significantly larger than SUSY signal ones. In order for the analysis to robustly target the desired signal the accurate modelling of such backgrounds is a fundamental part. The signal region definitions, discussed in Section 5.5, therefore need an accurate knowledge of the kinematical properties of both targeted signals and backgrounds whose modelling is strictly related to the sensitivity reached by the analysis. Such backgrounds, with their relative MC samples employed, which contribute to the search of direct stop-pair production in final states with jets and  $E_T^{\text{miss}}$ , will be discussed below using information taken from the Particle Data Group [8].

**Top pairs production:**  $t\bar{t}$  production is a major background for many third-generation SUSY analyses at the LHC. The dominant top-quark decay is  $t \rightarrow bW$  with a Branching Ratio (BR) of  $\sim 99.8\%$ , which in turn yields two oppositely charged  $b$ -jets and  $W$  bosons which will then yield 0-lepton, 1-lepton, and 2-lepton final states with 45.7%, 43.8%, and 10.5% BRs respectively, giving the name to the fully hadronic, semi-leptonic, and di-leptonic  $t\bar{t}$  decays, respectively;

**Single top production:** the production of one single top is also possible at the LHC. The different decays are usually referred to as  $s$ -channel,  $t$ -channel, and  $W$   $t$  channel, the last one being the most relevant for this analysis since it yields a  $W$ ;

**Z boson production in association with jets:** the production of a  $Z$  boson in association with jets is one of the main backgrounds in a 0-lepton plus  $E_T^{\text{miss}}$  final states, as well as a 2-lepton channel. The  $Z \rightarrow vv$  decay, with a  $\text{BR} \sim 20\%$ , and the  $Z \rightarrow \ell\ell$  decay<sup>2</sup>, with total  $\text{BR} \sim 10\%$ . Although the hadronic decay of the  $Z$  boson,  $Z \rightarrow qq$ , has the largest  $\text{BR}$  ( $\sim 70\%$ ), it is not relevant for third-generation SUSY searches, as the multi-jet background is still the dominant one. The  $Z + \text{jets}$  MC samples are generated categorising<sup>3</sup> the events depending on the flavours of the hadrons produced in association with the  $Z$  boson:

- $b$ -filtered: containing at least one  $b$ -hadron;
- $c$ -filtered: containing at least one  $c$ -hadron (no  $b$ -hadrons);
- light-filtered: no  $b$ - or  $c$ -hadrons included

In this analysis the major contribution to such background comes from the  $b$ -filtered sub-sample as the selected events contain  $b$ -jets.

**W boson production in association with jets:** the production of  $W$  bosons in association with jets is a relevant background in 1-lepton final states, due to the  $W \rightarrow \ell v$  decay which has a  $\text{BR}$  of  $\sim 32\%$ . The dominant hadronic decay of the  $W$ ,  $W \rightarrow qq'$ , produces a multi-jet final state which, again, is irrelevant for this analysis. As the  $Z + \text{jets}$  MC samples, even the  $W + \text{jet}$  events are equally categorised depending on the flavour of the hadrons produced in association with the  $W$  boson;

**Di-bosons production:** albeit the production of pairs of bosons,  $WW$ ,  $WZ$ , and  $ZZ$ , can also be a source of background in channels with leptons or jets, depending on the decay mode of each boson;

**Top pairs production in association with a vector boson:** the cross section of the production of top pairs in association with a vector boson or a Higgs boson is smaller than the processes considered thus far. Nevertheless, such background can be a prominent background for third-generation SUSY analyses. In particular, the top-pair production in association with a  $Z$  boson, with the  $Z$  boson decaying to neutrinos,  $t\bar{t} + Z \rightarrow vv$ , does represent an irreducible background for this analysis: it yields a final state with jets and  $E_T^{\text{miss}}$  which looks identical to the signal searched for. For such reason a data-driven technique is employed, where essentially the top-pair production in association with a photon  $t\bar{t}+\gamma$  is used instead. Further details on the method for its estimation will be given in Section 5.7;

**Multi-jet:** the multi-jet production is the process with the highest cross section among the ones mentioned so far, and even though such events do not contain neither leptons nor  $E_T^{\text{miss}}$  they could resemble the signal due to either isolated but mis-reconstructed leptons or large measured  $E_T^{\text{miss}}$  due to detector resolution. Despite the low probability of such

---

<sup>2</sup>  $\ell = e, \mu, \tau$

<sup>3</sup> Using the information at truth level

occurrence, the high rate of such background might generate a non-negligible contribution in a certain channel;

For most of the listed backgrounds, a set of additional sub-samples is generated in order to estimate the theoretical uncertainties associated with the generation of the process. The variations of, re-normalisation, factorisation, CKKW matching scales, different PDF sets or hadronisation models, are included.

## 5.5 Signal Region optimisation

The experimental signature for all signal topologies described in Section 5.1 is essentially characterised by the presence of multiple jets, two of which are required to have passed the  $b$ -tagging selection, a significant missing transverse energy, and no leptons (electrons or muons).

An initial overview of the five different sets of SRs, Signal Region A (SRA) to Signal Region E (SRE) employed to target each topology and kinematic regime will be given below:

**SRA** is sensitive to the production of high-mass  $\tilde{t}$  pairs with a large  $\tilde{t}-\tilde{\chi}_1^0$  mass splitting  $\Delta m(\tilde{t}_1, \tilde{\chi}_1^0)$ .

It is optimised for  $(m_{\tilde{t}_1}, m_{\tilde{\chi}_1^0}) = (1000, 1)$  GeV signal point;

**SRB** targets decays involving top squarks with high stop mass but with smaller  $\Delta m(\tilde{t}_1, \tilde{\chi}_1^0)$ . It

is optimised for  $(m_{\tilde{t}_1}, m_{\tilde{\chi}_1^0}) = (700, 400)$  GeV, and  $(m_{\tilde{t}_1}, m_{\tilde{\chi}_1^0}) = (600, 300)$  GeV signal points;

**SRC** is designed for the so-called highly compressed region where,  $\Delta m(\tilde{t}_1, \tilde{\chi}_1^0) \sim m_t$  and it em-

ploys an **ISR** to improve sensitivity to such decays. It targets various signal points e.g.

$(m_{\tilde{t}_1}, m_{\tilde{\chi}_1^0}) = (500, 327)$ , and  $(m_{\tilde{t}_1}, m_{\tilde{\chi}_1^0}) = (300, 127)$  GeV;

**SRD** targets the  $\tilde{t}_1 \rightarrow b\tilde{\chi}_1^\pm$  decay, with  $m_{\tilde{\chi}_1^\pm} = 2m_{\tilde{\chi}_1^0}$ , where no top-quark candidates are recon-

structed. It is optimised for  $(m_{\tilde{t}_1}, m_{\tilde{\chi}_1^0}) = (400, 50)$  GeV and  $(m_{\tilde{t}_1}, m_{\tilde{\chi}_1^0}) = (700, 100)$  GeV;

**SRE** is sensitive to highly boosted scenarios that can occur in gluino-mediated stop produc-

tion and it is optimised for  $(m_{\tilde{g}}, m_{\tilde{t}_1}, m_{\tilde{\chi}_1^0}) = (1700, 400, 395)$  GeV signal point;

### 5.5.1 Preliminary selection and discriminating key variables

A *pre-selection*, essentially a basic selection of candidate events common to all the SRs, is performed by applying trigger and event-cleaning cuts together with the requirement of a relevant set of physics objects according to the targeted experimental signature. A summary of the pre-selection cuts is shown in Table 5.2, where three groups of cuts are listed: a  $E_T^{\text{miss}}$  cut of 250 GeV is applied, to stay in a region where the trigger is fully efficient, as already mentioned in Section 5.3; a lepton veto is required, together with a cut on the number of jets (at least four, ordered in  $p_T > 80, 80, 40, 40$  GeV), at least one of which must be  $b$ -tagged, as signal events tend to have more energetic jets than the background; finally, an angular separation between

the azimuthal angle of the two highest- $p_T$  jets and the  $\mathbf{p}_T^{\text{miss}}$  is required to reject events with mis-measured  $E_T^{\text{miss}}$  originating from **SM**-background decays. In addition, in order to further reject these events, a requirement on  $\mathbf{p}_T^{\text{miss,track}}$  to be aligned in  $\phi$  with respect to the  $\mathbf{p}_T^{\text{miss}}$  calculated from the calorimeter system, is employed.

Table 5.2: Selection criteria common to all signal regions in addition to the event cleaning.

Object	Selection
Trigger $E_T^{\text{miss}}$	$E_T^{\text{miss}} > 250 \text{ GeV}$
$N_{\text{lep}}$	$= 0$
anti- $k_t$ $R = 0.4$ jets	$\geq 4$ , $p_T > 80, 80, 40, 40 \text{ GeV}$
$b$ -tagged jets	$\geq 1$
$ \Delta\phi(\text{jet}^{0,1}, \mathbf{p}_T^{\text{miss}}) $	$> 0.4$
$E_T^{\text{miss,track}}$	$> 30 \text{ GeV}$
$ \Delta\phi(\mathbf{p}_T^{\text{miss}}, \mathbf{p}_T^{\text{miss,track}}) $	$< \pi/3$

Figure 5.3 displays a pie chart of the **SM** background composition, after having applied all the cuts listed in Table 5.2. The main background is  $t\bar{t}$  production, as a result of the requirement on the number of jets and at least 1  $b$ -jet. The  $t\bar{t}$  **MC** sample used here is an inclusive sample<sup>4</sup>.

The physics objects, reconstructed as discussed in Section 4.2, are used to build the various variables used to discriminate the **SUSY** signal from the **SM** background. The event selection is based on such variables which will be described below:

$\mathbf{m}_T^i$ : The transverse mass ( $m_T$ ) between the  $i^{\text{th}}$  jet and the  $E_T^{\text{miss}}$  in the event.

$\mathbf{m}_T^{b,\text{min}}$ : Transverse mass between closest  $b$ -jet to  $E_T^{\text{miss}}$  and  $E_T^{\text{miss}}$ . This variable provides very good discrimination between signal and semileptonic  $t\bar{t}$  background.

$\mathbf{m}_T^{b,\text{max}}$ : Transverse mass between farthest  $b$ -jet to  $E_T^{\text{miss}}$  and  $E_T^{\text{miss}}$ . This variable provides

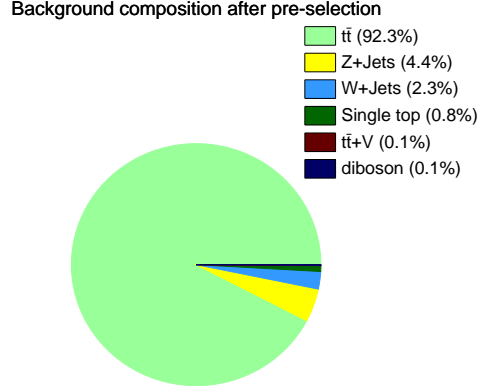


Figure 5.3: Pie chart of the background composition after the pre-selection selections described in Table 5.2

<sup>4</sup> The sample takes into account all the possible  $t\bar{t}$  decays: fully hadronic, semi-leptonic and di-leptonic

very good discrimination between signal and semileptonic  $t\bar{t}$  background.

**$\Delta R(\mathbf{b}, \mathbf{b})$ :** The angular separation between the two jets with the highest MV2c10 weight. This variable is useful in discriminating against the  $Z(v\bar{v}) + b\bar{b} + \text{jets}$  background.

**Top quark mass reconstruction** In addition to the above-mentioned variables, another set of variables is needed in SRs targeting the pair production of  $\tilde{t}_1 \rightarrow t + \tilde{\chi}_1^0$ : the reconstruction of two hadronically decaying top quarks in the event using the jet *re-clustering* algorithm, performed using the anti- $k_t$  algorithm (with a larger distance parameter  $R = 1.2$ ), fed with the calibrated anti- $k_t$   $R = 0.4$  jet collection (further details can be found in [92]). The highest- (second-highest)  $p_T$  re-clustered jet is chosen to be the first (second) top candidate. The best signal sensitivity is reached by using  $R = 1.2$  and  $R = 0.8$ , for top and  $W$  candidates, respectively [111, 112]. The variables used are the masses of the  $R = 1.2$  and  $R = 0.8$  leading and sub-leading jets, indicated by  $m_{\text{jet}, R=1.2}^0$ ,  $m_{\text{jet}, R=1.2}^1$ ,  $m_{\text{jet}, R=0.8}^0$ ,  $m_{\text{jet}, R=0.8}^1$ , respectively. Such variables help reduce the SM backgrounds.

### 5.5.2 Optimisation strategy

## 5.6 Nominal Background Estimation

### 5.6.1 Control Regions

### 5.6.2 Validation Regions

## 5.7 Data-Driven Background Estimation

## 5.8 Results and Interpretation

# CONCLUSION

*Every new beginning comes from  
some other beginning's end.*

---

Seneca

Last thing to write

# $t\bar{t}+Z$ ESTIMATION IN DM PLUS HEAVY FLAVOUR

A

The data-driven background estimation technique and the theory uncertainties calculation prescription already discussed in Chapter 5 were also employed in the search for dark matter produced in association with third-generation quarks, which was published in October 2017 in the Eur. Phys. J. [113]. This analysis also used  $36.1\text{fb}^{-1}$  of  $pp$  collisions delivered by the LHC and recorded with the ATLAS detector, and although it targeted various final states with different number of leptons, depending on the  $t\bar{t}$  decay modes, the author's contribution was only used for the experimental signature shown in Figure A.1, as this is identical to the final states discussed in Chapter 5, namely the one shown in Figure 5.1: 4 or more jets plus missing transverse momentum.

The objects used, and the variables employed in the design of a region of control for the  $t\bar{t}+\gamma$  process, are the same as those used in the analysis already discussed in Chapter 5. Only one set of 2 SR was used. Table bla shows the selection of the two SRs.

Table bla shows the control region selection employed ( $\text{CR}\gamma$ ) to isolate the  $t\bar{t}+\gamma$  process. This essentially is identical to Table blabla already shown in Chapter 5. A purity of bla% was reached and a scale factor of 1.whatever was obtained.

Figure bla2 shows the distribution of the  $E_{\text{T}}^{\text{miss}}$  in  $\text{CR}\gamma$  where a very good data/MC agreement was found.

The procedure adopted to estimate the contribution of the theory uncertainties to the total uncertainty is also the same and the results are shown in Table bla, where the highest uncertainty of whatever% was obtained for SR bla.

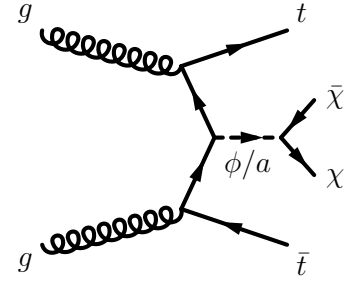


Figure A.1: Representative diagrams at the lowest order for spin-0 mediator associated production with top quarks  $t\bar{t} + \phi/a$  (taken from [113])

## LIST OF ACRONYMS

**ALICE** A Large Ion Collider Experiment

**AOD** Analysis Objects Data

**ATLAS** A Toroidal LHC ApparatuS

**BDT** Boosted Decisions Tree

**BR** Branching Ratio

**BSM** Beyond Standard Model

**CERN** European Organization for Nuclear Research

**CKKW** Catani-Krauss-Kuhn-Webber

**CMS** Compact Muon Solenoid

**CPU** Central Processing Unit

**CSC** Cathode Strip Chamber

**CTP** Central Trigger Processor

**DIS** Deep Inelastic Scattering

**DM** Dark Matter

**ECAL** Electromagnetic Calorimeter

**EM** electromagnetic

**ESD** Event Summary Data

**FCNC** Flavour Changing Neutral Currents

**FSR** Final State Radiation

**FTF** Fast Track Finder

**FTK** Fast TracKer

**GUT** Grand Unification Theory

**HCAL** Hadronic Calorimeter

**HLT** High Level Trigger

**IBL** Insertable B-Layer

**ID** Inner Detector

**ISR** Initial State Radiation

**JVT** Jet vertex Tagger

**L1** Level-1

**L1Calo** L1 Calorimeter

**L1Muon** L1 Muon

**L1Topo** Level-1 Topological

**LAr** Liquid Argon

**LEIR** Low Energy Ion Ring

**LEP** Large Electron-Positron Collider

**LH** Likelihood

**LHC** Large Hadron Collider

**LHCb** Large Hadron Collider beauty

**LHCf** Large Hadron Collider forward

**LINAC2** Linear Accelerator 2

**LINAC3** Linear Accelerator 3

**LO** Leading Order

**LS1** Long Shut down 1

**LSP** Lightest Supersymmetric Particle

**MC** Monte Carlo

**ME** Matrix Element

**MDT** Monitored Drift Tube

**MIP** Minimum Ionising Particle

**MLM** Michelangelo L. Mangano

**MoEDAL** Monopole & Exotics Detector At the [LHC](#)

**MS** Muon Spectrometer

**MSSM** Minimal Supersymmetric Standard Model

**MV2** Multivariate algorithm

**NLO** Next-to-Leading Order

**NLSP** Next Lightest Supersymmetric Particle

**OR** Overlap Removal

**PDF** Parton Distribution Function

**pMSSM** Phenomenological [MSSM](#)

**PS** Parton Shower

**PSB** Proton Synchrotron Booster

**PV** Primary Vertex

**QCD** Quantum Chromodynamics

**QED** Quantum Electrodynamics

**QFT** Quantum Field Theory

**RDO** Raw Data Object

**RoI** Region of Interest

**ROS** Read-Out System

**RPC** *R*-Parity Conserving

**RPC** Resistive-Plate Chamber

**SCT** SemiConductor Tracker

**SM** Standard Model

**SPS** Super Proton Synchrotron

**SR** Signal Region

**SUSY** Supersymmetry

**SV** Secondary Vertex

**TDAQ** Trigger and Data Acquisition

**TGC** Thin-Gap Chamber

**TOTEM** TOTal cross section, Elastic scattering and diffraction dissociation Measurement at the [LHC](#)

**TRT** Transition Radiation Tracker

**UE** Underlying Event

**VEV** Vacuum Expectation Value

**WIMP** Weakly Interacting Massive Particle

**WP** Working Point

## BIBLIOGRAPHY

- [1] M. Herrero, *The Standard Model*, <https://arxiv.org/abs/hep-ph/9812242>. 3
- [2] The ATLAS Collaboration, *Observation of a New Particle in the Search for the Standard Model Higgs Boson with the ATLAS Detector at the LHC*, *Phys.Lett.* **B716** (2012), [arXiv:1207.7214 \[hep-ex\]](https://arxiv.org/abs/1207.7214). 3
- [3] CMS Collaboration, *Observation of a new boson at a mass of 125 GeV with the CMS experiment at the LHC*, *Phys.Lett.* **B716** (2012), [arXiv:1207.7235 \[hep-ex\]](https://arxiv.org/abs/1207.7235). 3
- [4] M. E. Peskin, D. V. Schroeder, *An Introduction to Quantum Field Theory*. Westview Press, 1995. 3
- [5] W. N. Cottingham and D. A. Greenwood, *An introduction to the standard model*. Cambridge, 1998. 3
- [6] L. Lederman and C. Hill, *Symmetry and the Beautiful Universe*. Prometheus Books, 2004. <https://books.google.co.uk/books?id=X2QPAQAAQAAJ>. 3
- [7] A. Pich, *The Standard Model of Electroweak Interactions*, [arXiv:1201.0537 \[hep-ph\]](https://arxiv.org/abs/1201.0537). 3, 6
- [8] Particle Data Group Collaboration, C. Patrignani et al., *Review of Particle Physics*, *Chin. Phys.* **C40** no. 10, (2016) 100001. 4, 61
- [9] S. Weinberg, *The quantum theory of fields. Vol. 2: Modern applications*. Cambridge University Press, 2013. 5
- [10] S. L. Glashow, *Partial Symmetries of Weak Interactions*, *Nucl. Phys.* **22** (1961) 579–588. 5
- [11] A. Salam and J. Ward, *Electromagnetic and weak interactions*, *Physics Letters* **13** no. 2, (1964) 168 – 171.  
<http://www.sciencedirect.com/science/article/pii/0031916364907115>. 5
- [12] S. Weinberg, *A Model of Leptons*, *Phys. Rev. Lett.* **19** (1967) 1264–1266.  
<https://link.aps.org/doi/10.1103/PhysRevLett.19.1264>. 5

- [13] P. W. Higgs, *Broken Symmetries and the Masses of Gauge Bosons*, *Phys. Rev. Lett.* **13** (1964) 508–509. 6
- [14] J. Goldstone, A. Salam and S. Weinberg, *Broken Symmetries*, *Phys. Rev.* **127** (1962) 965–970. 7
- [15] ATLAS Collaboration, “Summary plots from the ATLAS Standard Model physics group.” [https://atlas.web.cern.ch/Atlas/GROUPS/PHYSICS/CombinedSummaryPlots/SM/ATLAS\\_a\\_SMSummary\\_TotalXsect/ATLAS\\_a\\_SMSummary\\_TotalXsect.png](https://atlas.web.cern.ch/Atlas/GROUPS/PHYSICS/CombinedSummaryPlots/SM/ATLAS_a_SMSummary_TotalXsect/ATLAS_a_SMSummary_TotalXsect.png). 9
- [16] S. Weinberg, *Implications of Dynamical Symmetry Breaking*, *Phys. Rev.* **D19** (1976) 1277–1280. 8
- [17] Super-Kamiokande Collaboration, Y. Fukuda et al., *Evidence for oscillation of atmospheric neutrinos*, *Phys. Rev. Lett.* **81** (1998) 1562–1567, [arXiv:hep-ex/9807003 \[hep-ex\]](https://arxiv.org/abs/hep-ex/9807003). 9
- [18] SNO Collaboration, *Measurement of the Rate of  $\nu_e + d \rightarrow p + p + e^-$  Interactions Produced by  ${}^8B$  Solar Neutrinos at the Sudbury Neutrino Observatory*, *Phys. Rev. Lett.* **87** (2001). 9
- [19] The official website of the Nobel Prize.  
[https://www.nobelprize.org/nobel\\_prizes/physics/laureates/2015/](https://www.nobelprize.org/nobel_prizes/physics/laureates/2015/). 9
- [20] E. Kh. Akhmedov, et. al, *Seesaw mechanism and structure of neutrino mass matrix*, *Phys. Lett.* **B478** (1999). 9
- [21] V. C. Rubin and W. K. Ford, Jr., *Rotation of the Andromeda Nebula from a Spectroscopic Survey of Emission Regions*, *Astrophysical Journal* **159** (1970) 379. 10
- [22] M. H. Jones, R. J. A. Lambourne, and S. Serjeant, *An Introduction to Galaxies and Cosmology* (2nd ed). Cambridge University Press/Open University, Cambridge, January, 2015. <http://oro.open.ac.uk/44361/>. 10
- [23] S. P. Martin, *A Supersymmetry primer*, [arXiv:hep-ph/9709356 \[hep-ph\]](https://arxiv.org/abs/hep-ph/9709356). [Adv. Ser. Direct. High Energy Phys.18,1(1998)]. 10
- [24] R. Barbieri and G. F. Giudice, *Upper Bounds on Supersymmetric Particle Masses*, *Nucl. Phys.* **B306** (1988) 63–76. 10
- [25] F. Jegerlehner, *The hierarchy problem of the electroweak Standard Model revisited*, [arXiv:1305.6652 \[hep-ph\]](https://arxiv.org/abs/1305.6652). 12
- [26] H. E. Haber and G. L. Kane, *The Search for Supersymmetry: Probing Physics Beyond the Standard Model*, *Phys. Rept.* **117** (1985) 75–263. 13
- [27] K. Hidaka and A. Bartl, *Impact of bosonic decays on the search for the lighter stop and sbottom squarks*, *Phys. Lett.* **B501** (2001) 78–85, [arXiv:hep-ph/0012021 \[hep-ph\]](https://arxiv.org/abs/hep-ph/0012021). 13

- [28] C. Borschensky, M. Kramer, A. Kulesza, M. Mangano, S. Padhi, T. Plehn, and X. Portell, *Squark and gluino production cross sections in pp collisions at  $\sqrt{s} = 13, 14, 33$  and 100 TeV*, *Eur. Phys. J. C* **74** (2014) 3174, [arXiv:1407.5066 \[hep-ph\]](https://arxiv.org/abs/1407.5066). 16, 58
- [29] O. S. Brüuning, P. Collier, P. Lebrun, S. Myers, R. Ostojic, J. Poole and P. Proudlock, *LHC Design Report*, <https://cds.cern.ch/record/782076>. 19, 20
- [30] J.M. Jowett, M. Schaumann, R. Alemany, R. Bruce, M. Giovannozzi, P. Hermes, W. Hofle, M. Lamont, T. Mertens, S. Redaelli, J. Uythoven, J. Wenninger, *The 2015 Heavy-Ion Run of the LHC*, <http://accelconf.web.cern.ch/accelconf/ipac2016/papers/tupmw027.pdf>. 20
- [31] C. Lefèvre, *The CERN accelerator complex*, [http://cds.cern.ch/record/1260465](https://cds.cern.ch/record/1260465). 21, 22
- [32] The ATLAS Collaboration, *The ATLAS experiment at the CERN Large Hadron Collider*, *Journal of Instrumentation* **3** no. 08, (2008) S08003. <http://stacks.iop.org/1748-0221/3/i=08/a=S08003>. 21, 23, 29, 33, 34
- [33] CMS Collaboration, *The CMS experiment at the CERN LHC*, *Journal of Instrumentation* **3** no. 08, (2008) S08004. <http://stacks.iop.org/1748-0221/3/i=08/a=S08004>. 21
- [34] LHCb Collaboration, *The LHCb Detector at the LHC*, *JINST* (2008). 21, 42
- [35] ALICE Collaboration, *The ALICE experiment at the CERN LHC*, *Journal of Instrumentation* **3** no. 08, (2008) S08002. <http://stacks.iop.org/1748-0221/3/i=08/a=S08002>. 21
- [36] TOTEM Collaboration, *The TOTEM Experiment at the CERN Large Hadron Collider*, *Journal of Instrumentation* **3** no. 08, (2008) S08007. <http://stacks.iop.org/1748-0221/3/i=08/a=S08007>. 21
- [37] LHCf Collaboration, *LHCf experiment: Technical Design Report*. Technical Design Report LHCf. CERN, Geneva, 2006. [http://cds.cern.ch/record/926196](https://cds.cern.ch/record/926196). 21
- [38] J. Pinfold, *The MoEDAL experiment at the LHC*, *EPJ Web Conf.* **145** (2017) 12002. 21
- [39] A. Yamamoto, Y. Makida, R. Ruber, Y. Doi, T. Haruyama, F. Haug, H. ten Kate, M. Kawai, T. Kondo, Y. Kondo, J. Metselaar, S. Mizumaki, G. Olesen, O. Pavlov, S. Ravat, E. Sbrissa, K. Tanaka, T. Taylor, and H. Yamaoka, *The ATLAS central solenoid*, *Nuclear Instruments and Methods in Physics Research Section A: Accelerators, Spectrometers, Detectors and Associated Equipment* **584** no. 1, (2008) 53 – 74. <http://www.sciencedirect.com/science/article/pii/S0168900207020414>. 23
- [40] The ATLAS Collaboration, *The ATLAS Inner Detector commissioning and calibration*, *Eur. Phys. JC* **70**, [arXiv:1004.5293](https://arxiv.org/abs/1004.5293). 24

- 
- [41] The ATLAS Collaboration, *ATLAS Insertable B-Layer Technical Design Report*, <https://cds.cern.ch/record/1291633>. 25, 36
- [42] G. A. et al., *ATLAS pixel detector electronics and sensors*, Journal of Instrumentation **3** no. 07, (2008) P07007. <http://stacks.iop.org/1748-0221/3/i=07/a=P07007>. 25
- [43] A. Bingül, *The ATLAS TRT and its Performance at LHC*, Journal of Physics: Conference Series **347** no. 1, (2012) 012025. <http://iopscience.iop.org/article/10.1088/1742-6596/347/1/012025/meta>. 26
- [44] The ATLAS Collaboration, *Studies of the performance of the ATLAS detector using cosmic-ray muons*, The European Physical Journal C **71** no. 3, (2011) 1593. <https://doi.org/10.1140/epjc/s10052-011-1593-6>. 26
- [45] The ATLAS Collaboration, *ATLAS liquid-argon calorimeter: Technical Design Report*, <https://cds.cern.ch/record/331061>. 28
- [46] The ATLAS Collaboration, *ATLAS muon spectrometer: Technical design report*, <https://cds.cern.ch/record/331068>. 28
- [47] The ATLAS Collaboration, *Fast TrackEr (FTK) Technical Design Report*, <https://cds.cern.ch/record/1552953>. 30
- [48] The ATLAS Collaboration, *Performance of the ATLAS Trigger System in 2015*, Eur. Phys. J. **C77** (2017), [arXiv:1611.09661 \[hep-ex\]](arXiv:1611.09661). 31, 32, 33, 35, 36, 37, 38, 39
- [49] E. Simoni, *The Topological Processor for the future ATLAS Level-1 Trigger: from design to commissioning*, <arXiv:1406.4316>. 33
- [50] The ATLAS Collaboration, *Performance of the ATLAS Trigger System in 2010*, Eur. Phys. J. **C72** (2012), [arXiv:1110.1530 \[hep-ex\]](arXiv:1110.1530). 33, 34, 35
- [51] The ATLAS Collaboration, *The ATLAS Level-1 Calorimeter Trigger*, Journal of Instrumentation **3** no. 03, (2008) P03001. <http://stacks.iop.org/1748-0221/3/i=03/a=P03001>. 33
- [52] The ATLAS Collaboration, *Expected Performance of the ATLAS Experiment - Detector, Trigger and Physics*, [arXiv:0901.0512 \[hep-ex\]](arXiv:0901.0512). 34
- [53] F. Miano for the ATLAS Collaboration, *The design and performance of the ATLAS Inner Detector trigger for Run 2 LHC collisions at  $\sqrt{s} = 13$  TeV*, PoS **ICHEP2016** (2016) 856. 36
- [54] The ATLAS Collaboration, *Performance of primary vertex reconstruction in proton-proton collisions at  $\sqrt{s} = 7$  TeV in the ATLAS experiment*, tech. rep., CERN. 38
- [55] N. Ruthmann, Y. Nakahama, and C. Leonidopoulos, *Trigger Menu in 2016*, Tech. Rep. ATL-COM-DAQ-2016-137, CERN, Geneva, Sep, 2016. <https://cds.cern.ch/record/2216366>. 40

- 
- [56] The ATLAS Collaboration, “Missing energy trigger public results.” <https://twiki.cern.ch/twiki/bin/view/AtlasPublic/MissingEtTriggerPublicResults>. 41
- [57] W. Lukas, *Fast Simulation for ATLAS: Atlfast-II and ISF*, J. Phys.: Conf. Ser. **396** no. 022031, (2012). 42, 46
- [58] The ATLAS Collaboration, *ATLAS Computing : technical design report*, <https://cds.cern.ch/record/837738>. 42
- [59] G. Barrand, et. al, *GAUDI - A software architecture and framework for building HEP data processing applications.*, [http://dx.doi.org/10.1016/S0010-4655\(01\)00254-5](http://dx.doi.org/10.1016/S0010-4655(01)00254-5). 42
- [60] A. Buckley et al., *General-purpose event generators for LHC physics*, Phys. Rept. **504** (2011) 145–233, [arXiv:1101.2599 \[hep-ph\]](https://arxiv.org/abs/1101.2599). 43
- [61] R. P. Feynman, *Very High-Energy Collisions of Hadrons*, Phys. Rev. Lett. **23** (1969) 1415–1417. <https://link.aps.org/doi/10.1103/PhysRevLett.23.1415>. 43
- [62] T.-M. Yan and S. D. Drell, *The Parton Model and its Applications*, Int. J. Mod. Phys. **A29** (2014) 0071, [arXiv:1409.0051 \[hep-ph\]](https://arxiv.org/abs/1409.0051). 43
- [63] J. D. Bjorken, *Asymptotic Sum Rules at Infinite Momentum*, Phys. Rev. **179** (1969) 1547–1553. <https://link.aps.org/doi/10.1103/PhysRev.179.1547>. 43
- [64] M. Dobbs and J. B. Hansen, *The HepMC C++ Monte Carlo event record for High Energy Physics*, Computer Physics Communications **134** no. 1, (2001) 41 – 46. <http://www.sciencedirect.com/science/article/pii/S0010465500001892>. 44
- [65] ZEUS, H1 Collaboration, F D. Aaron et al., *Combined Measurement and QCD Analysis of the Inclusive ep Scattering Cross Sections at HERA*, JHEP **01** (2010) 109, [arXiv:0911.0884 \[hep-ex\]](https://arxiv.org/abs/0911.0884). 44
- [66] J. M. Campbell, J. Houston and W. Stirling, *Hard Interactions of Quarks and Gluons: A Primer of LHC Physics*, Rept. Prog. Phys. **70** no. 1, (2007). 44
- [67] V. N. Gribov and L. N. Lipatov, *Deep inelastic e p scattering in perturbation theory*, Sov. J. Nucl. Phys. **15** (1972) 438–450. [Yad. Fiz.15,781(1972)]. 44
- [68] G. Altarelli and G. Parisi, *Asymptotic Freedom in Parton Language*, Nucl. Phys. **B126** (1977) 298–318. 44
- [69] G. Corcella, et al., *HERWIG 6: an event generator of hadron emission reactions with interfering gluons (including supersymmetric processes)*, J. High Energy Phys. **JHEP(2001)** (2001). <http://iopscience.iop.org/article/10.1088/1126-6708/2001/01/010/meta>. 45

- 
- [70] Torbjörn Sjöstrand and Stephen Mrenna and Peter Skands, *PYTHIA 6.4 physics and manual*, Journal of High Energy Physics **2006** no. 05, (2006) 026.  
<http://stacks.iop.org/1126-6708/2006/i=05/a=026>. 45
- [71] T. Gleisberg et al., *Event generation with SHERPA 1.1*, JHEP **02** (2009) 007. 45
- [72] Bernd A. Berg, *Introduction to Markov Chain Monte Carlo Simulations and their Statistical Analysis*, arXiv:cond-mat/0410490 [cond-mat]. 45
- [73] S. Catani, F. Krauss, R. Kuhn and B. Webber, *QCD Matrix Elements + Parton Showers*, JHEP 0111 (2001), arXiv:hep-ph/0109231 [hep-ph]. 45
- [74] M. L. Mangano, M. Moretti and R. Pittau, *Multijet Matrix Elements and Shower Evolution in Hadronic Collisions:  $Wb\bar{b} + n$  Jets as a Case Study*, Nucl.Phys **B632** (2001), arXiv:0108069 [hep-ph]. 45
- [75] A. Kupco , *Cluster Hadronization in HERWIG 5.9*, arXiv:hep-ph/9906412 [hep-ph]. 45
- [76] B. Andersson, S. Mohanty and F. Soderberg, *Recent Developments in the Lund Model*, arXiv:hep-ph/0212122 [hep-ph]. 45
- [77] R. D. Field, *The Underlying Event in Hard Scattering Processes*, arXiv:hep-ph/0201192 [hep-ph]. 45
- [78] GEANT4 Collaboration, *Geant4 a simulation toolkit*, Nucl. Instrum. Meth. A **506** (2003). 46
- [79] *Vertex Reconstruction Performance of the ATLAS Detector at " $\sqrt{s} = 13$  TeV"*, Tech. Rep. ATL-PHYS-PUB-2015-026, CERN, Geneva, Jul, 2015.  
<https://cds.cern.ch/record/2037717>. 47, 48
- [80] R. Frühwirth, W. Waltenberger, and P. Vanlaer, *Adaptive vertex fitting*, J. Phys. **G34** (2007) N343. 47, 48
- [81] The ATLAS Collaboration, *Electron and photon energy calibration with the ATLAS detector using data collected in 2015 at  $\sqrt{s} = 13$  TeV*, tech. rep., CERN. 48
- [82] G. Aad et al., *Electron and photon energy calibration with the ATLAS detector using LHC Run 1 data.*, 48
- [83] The ATLAS collaboration, *Electron efficiency measurements with the ATLAS detector using the 2015 LHC proton-proton collision data.*, 48
- [84] The ATLAS Collaboration, “Electron and photon performance public results.”  
<https://twiki.cern.ch/twiki/bin/view/AtlasPublic/ ElectronGammaPublicCollisionResults>. 49, 50

- 
- [85] ATLAS Collaboration, The ATLAS Collaboration, *Measurement of the photon identification efficiencies with the ATLAS detector using LHC Run-1 data*, *Eur. Phys. J.* **C76** no. 12, (2016) 666, [arXiv:1606.01813 \[hep-ex\]](https://arxiv.org/abs/1606.01813). 50, 59
- [86] The ATLAS Collaboration Collaboration, *Photon identification in 2015 ATLAS data*, Tech. Rep. ATL-PHYS-PUB-2016-014, CERN, Geneva, Aug, 2016.  
<https://cds.cern.ch/record/2203125>. 49
- [87] The ATLAS Collaboration, *Muon reconstruction performance of the ATLAS detector in proton–proton collision data at  $\sqrt{s} = 13$  TeV*, 49, 50
- [88] The ATLAS Collaboration, “Atlas muon combined performance with the full 2016 dataset.” <https://atlas.web.cern.ch/Atlas/GROUPS/PHYSICS/PLOTS/MUON-2017-001/index.html>. 51
- [89] The ATLAS Collaboration, *Electron reconstruction and identification efficiency measurements with the ATLAS detector using the 2011 LHC proton-proton collision data*, *Eur. Phys. J.* **74** no. 7, (2014), [arXiv:1404.2240 \[hep-ex\]](https://arxiv.org/abs/1404.2240). 50
- [90] W. Lampl, et al., *Calorimeter Clustering Algorithms: Description and Performance*,  
<https://cds.cern.ch/record/1099735>. 51
- [91] THe ATLAS Collaboration, *Topological cell clustering in the ATLAS calorimeters and its performance in LHC Run 1*, 51
- [92] G. S. M. Cacciari, G. P. Salam, *The Anti- $k(t)$  jet clustering algorithm*, *JHEP* **0804** (2008), [arXiv:0802.1189 \[hep-ph\]](https://arxiv.org/abs/0802.1189). 52, 65
- [93] The ATLAS Collaboration, *Jet Calibration and Systematic Uncertainties for Jets Reconstructed in the ATLAS Detector at  $\sqrt{s} = 13$  TeV*, Tech. Rep. ATL-PHYS-PUB-2015-015, CERN, Geneva, Jul, 2015.  
<https://cds.cern.ch/record/2037613>. 52
- [94] The ATLAS collaboration, *Pile-up subtraction and suppression for jets in ATLAS*,. 52
- [95] The ATLAS collaboration, *Jet global sequential corrections with the ATLAS detector in proton-proton collisions at  $\sqrt{s} = 8$  TeV*,. 52
- [96] The ATLAS collaboration, *Data-driven determination of the energy scale and resolution of jets reconstructed in the ATLAS calorimeters using dijet and multijet events at  $\sqrt{s} = 8$  TeV*, Tech. Rep. ATLAS-CONF-2015-017, CERN, Geneva, Apr, 2015.  
<https://cds.cern.ch/record/2008678>. 52
- [97] The ATLAS Collaboration, *Tagging and suppression of pileup jets with the ATLAS detector*, Tech. Rep. ATLAS-CONF-2014-018, CERN, Geneva, May, 2014.  
<https://cds.cern.ch/record/1700870>. 52

- [98] The ATLAS Collaboration, *Identification and rejection of pile-up jets at high pseudorapidity with the ATLAS detector.*, 52
- [99] N. Bartosik, *Diagram showing the common principle of identification of jets initiated by b-hadron decays*, 2016. [http://bartosik.pp.ua/hep\\_sketches/btagging](http://bartosik.pp.ua/hep_sketches/btagging). 53
- [100] The ATLAS Collaboration, *Performance of b-Jet Identification in the ATLAS Experiment.*, 53
- [101] The ATLAS Collaboration, *Performance and Calibration of the JetFitterCharm Algorithm for c-Jet Identification*, Tech. Rep. ATL-PHYS-PUB-2015-001, CERN, Geneva, Jan, 2015. <http://cds.cern.ch/record/1980463>. 53
- [102] M. Lehmacher, *b-Tagging Algorithms and their Performance at ATLAS*, Tech. Rep. ATL-PHYS-PROC-2008-052. ATL-COM-PHYS-2008-152, CERN, Geneva, Jul, 2008. <http://cds.cern.ch/record/1128662>. 53
- [103] The ATLAS Collaboration, *Secondary vertex finding for jet flavour identification, with the ATLAS detector*, tech. rep., CERN. 53
- [104] G. Piacquadio and C. Weiser, *A new inclusive secondary vertex algorithm for b-jet tagging in ATLAS*, Journal of Physics: Conference Series **119** no. 3, (2008) 032032. <http://stacks.iop.org/1742-6596/119/i=3/a=032032>. 53
- [105] L. Breiman et al., *Classification and Regression Trees*. Chapman & Hall, New York, 1984. <http://www.crcpress.com/catalog/C4841.htm>. 53
- [106] R. Brun and F. Rademakers, *ROOT: An object oriented data analysis framework*, Nucl. Instrum. Meth. **A389** (1997) 81–86. 53
- [107] A. Hoecker, P. Speckmayer, J. Stelzer, J. Therhaag, E. von Toerne, H. Voss, M. Backes, T. Carli, O. Cohen, A. Christov, D. Dannheim, K. Danielowski, S. Henrot-Versille, M. Jachowski, K. Kraszewski, A. Krasznahorkay, Jr., M. Kruk, Y. Mahalalel, R. Ospanov, X. Prudent, A. Robert, D. Schouten, F. Tegenfeldt, A. Voigt, K. Voss, M. Wolter, and A. Zemla, *TMVA - Toolkit for Multivariate Data Analysis*, ArXiv Physics e-prints (2007), [physics/0703039](https://arxiv.org/abs/physics/0703039). 53
- [108] ATLAS Collaboration, *Optimisation of the ATLAS b-tagging performance for the 2016 LHC Run*, Tech. Rep. ATL-PHYS-PUB-2016-012, CERN, Geneva, Jun, 2016. <http://cds.cern.ch/record/2160731>. 54
- [109] The ATLAS Collaboration, “ATLAS Event Displays from papers.” <https://twiki.cern.ch/twiki/bin/view/AtlasPublic/EventDisplayPapers>. 54
- [110] The ATLAS Collaboration, *Performance of missing transverse momentum reconstruction for the ATLAS detector in the first proton-proton collisions at at  $\sqrt{s}=13$  TeV*, Tech. Rep. ATL-PHYS-PUB-2015-027, CERN, Geneva, Jul, 2015. <http://cds.cern.ch/record/2037904>. 54

- 
- [111] The ATLAS Collaboration, *Search for a scalar partner of the top quark in the jets plus missing transverse momentum final state at  $\sqrt{s}=13$  TeV with the ATLAS detector*, [JHEP 06 \(2013\) 065](#)
- [112] The ATLAS Collaboration, *Search for the Supersymmetric Partner of the Top Quark in the Jets+ $E_T^{\text{miss}}$  Final State at  $\sqrt{s} = 13$  TeV*, [JHEP 06 \(2013\) 065](#)
- [113] The ATLAS Collaboration, *Search for dark matter produced in association with bottom or top quarks in  $\sqrt{s} = 13$  TeV pp collisions with the ATLAS detector*, [JHEP 06 \(2013\) 067](#)
- [114] J. Alwall, M.-P. Le, M. Lisanti, and J. G. Wacker, *Searching for directly decaying gluinos at the Tevatron*, [Phys. Lett. B 666 \(2008\) 34–37](#), [arXiv:0803.0019 \[hep-ph\]](#).
- [115] J. Alwall, P. Schuster, and N. Toro, *Simplified models for a first characterization of new physics at the LHC*, [Phys. Rev. D 79 \(2009\) 075020](#), [arXiv:0810.3921 \[hep-ph\]](#).
- [116] LHC New Physics Working Group Collaboration, D. Alves, *Simplified models for LHC new physics searches*, [J. Phys. G 39 \(2012\) 105005](#), [arXiv:1105.2838 \[hep-ph\]](#).
- [117] A. Djouadi et al., *The Minimal supersymmetric standard model: Group summary report*, [arXiv:9901246 \[hep-ph\]](#).
- [118] C. F. Berger, J. S. Gainer, J. L. Hewett, and T. G. Rizzo, *Supersymmetry without prejudice*, [JHEP 02 \(2009\) 023](#), [arXiv:0812.0980 \[hep-ph\]](#).
- [119] J. Alwall, R. Frederix, S. Frixione, V. Hirschi, F. Maltoni, O. Mattelaer, H. S. Shao, T. Stelzer, P. Torrielli, and M. Zaro, *The automated computation of tree-level and next-to-leading order differential cross sections, and their matching to parton shower simulations*, [JHEP 07 \(2014\) 079](#), [arXiv:1405.0301 \[hep-ph\]](#).
- [120] T. Sjöstrand, S. Mrenna, and P. Z. Skands, *A brief introduction to PYTHIA 8.1*, [Comput. Phys. Commun. 178 \(2008\) 852–867](#), [arXiv:0710.3820 \[hep-ph\]](#).
- [121] D. J. Lange, *The EvtGen particle decay simulation package*, [Nucl. Instrum. Meth. 462 no. 1–2, \(2001\) 152 – 155](#).
- [122] R. D. Ball et al., *Parton distributions with LHC data*, [Nucl. Phys. B 867 \(2013\) 244–289](#), [arXiv:1207.1303 \[hep-ph\]](#).
- [123] H.-L. Lai, M. Guzzi, J. Huston, Z. Li, P. M. Nadolsky, J. Pumplin, and C. P. Yuan, *New parton distributions for collider physics*, [Phys. Rev. D 82 \(2010\) 074024](#), [arXiv:1007.2241 \[hep-ph\]](#).
- [124] L. Lönnblad and S. Prestel, *Merging multi-leg NLO matrix elements with parton showers*, [JHEP 03 \(2013\) 166](#), [arXiv:1211.7278 \[hep-ph\]](#).
- [125] W. Beenakker, M. Kramer, T. Plehn, M. Spira, and P. M. Zerwas, *Stop production at hadron colliders*, [Nucl. Phys. B515 \(1998\) 3–14](#), [hep-ph/9710451](#).

- 
- [126] W. Beenakker, S. Brensing, M. Kramer, A. Kulesza, E. Laenen, and I. Niessen, *Supersymmetric top and bottom squark production at hadron colliders*, JHEP **1008** (2010) 098, [arXiv:1006.4771 \[hep-ph\]](https://arxiv.org/abs/1006.4771). 58
- [127] W. Beenakker, S. Brensing, M. Kramer, A. Kulesza, E. Laenen, et al., *Squark and gluino hadroproduction*, Int.J.Mod.Phys. **A26** (2011) 2637–2664, [arXiv:1105.1110 \[hep-ph\]](https://arxiv.org/abs/1105.1110). 58
- [128] B. Allanach, *SOFTSUSY: a program for calculating supersymmetric spectra*, Comput. Phys. Commun. **143** (2002) 305–331, [arXiv:hep-ph/0104145](https://arxiv.org/abs/hep-ph/0104145). 58
- [129] B. Allanach, P. Athron, L. C. Tunstall, A. Voigt, and A. Williams, *Next-to-minimal SOFTSUSY*, Comput. Phys. Commun. **185** (2014) 2322–2339, [arXiv:1311.7659 \[hep-ph\]](https://arxiv.org/abs/1311.7659). 58
- [130] A. Djouadi, J. Kalinowski and M. Spira, *HDECAY: A Program for Higgs boson decays in the standard model and its supersymmetric extension*, Comput. Phys. Commun. **108** (1998) 56, [arXiv:9704448 \[hep-ph\]](https://arxiv.org/abs/9704448). 58
- [131] A. Djouadi, M. Muhlleitner and M. Spira, *Decays of supersymmetric particles: The Program SUSY-HIT (SUspect-SdecaY-Hdecay-InTerface)*, Acta. Phys. Polon. B **38** (2007) 635–644, [arXiv:0609292 \[hep-ph\]](https://arxiv.org/abs/0609292). 58
- [132] The ATLAS Collaboration, *Electron efficiency measurements with the ATLAS detector using 2012 LHC proton–proton collision data*, 59
- [133] The ATLAS Collaboration, *Electron identification measurements in ATLAS using  $\sqrt{s} = 13$  TeV data with 50 ns bunch spacing*. <https://cds.cern.ch/record/2048202>. 59
- [134] The ATLAS Collaboration, *Muon reconstruction performance of the ATLAS detector in proton–proton collision data at  $\sqrt{s} = 13$  TeV*, 59
- [135] The ATLAS Collaboration, *Search for direct pair production of the top squark in all-hadronic final states in proton-proton collisions at  $\sqrt{s} = 8$  TeV with the ATLAS detector*, JHEP **09** (2014) 015, [arXiv:1406.1122 \[hep-ex\]](https://arxiv.org/abs/1406.1122). 59

This thesis was typeset using the L<sup>A</sup>T<sub>E</sub>X typesetting system created by Leslie Lamport.  
The body text size is set to 11 pt with *Utopia Regular* with *Fourier* font, part of T<sub>E</sub>X Live.  
The bibliography was typeset using the [ATLAS](#)-paper style.